

NASA-CR-194192

REMTECH

RTR 214-01

1991 VERSION OF THE PLUME
IMPINGEMENT COMPUTER PROGRAM
VOLUME I — DESCRIPTION

October 1991

Prepared by:

Robert L. Bender
Richard E. Somers
Maurice J. Prendergast
Joseph P. Clayton
of REMTECH inc.

Sheldon D. Smith
of SECA, Inc.

Contract:

NAS8-38423

For:

National Aeronautics and Space Administration
George C. Marshall Space Flight Center
Marshall Space Flight Center, AL 35812

NATIONAL AERONAUTICS AND SPACE ADMINISTRATION
SBIR PHASE II FINAL REPORT

PROJECT SUMMARY

CONTRACT NO. NAS8-38423

PROJECT TITLE Vacuum Plume Impingement Evaluator

PURPOSE The objective of this contract was to continue development of a vacuum plume impingement evaluator to provide an analyst with a capability for rapid assessment of thruster plume impingement scenarios. The research was divided into three areas: Plume Impingement Computer Program (PLIMP) modification/validation; graphics development; and documentation in the form of a Plume Handbook and PLIMP Input Guide.

RESEARCH COMPLETED PLIMP code modifications and enhancements have been made to provide more detailed output information, improved shading, and the ability to order and analyze two-phase impingement solutions in a single execution. The code was also modified to accept plume flowfields generated using the Source Flow Plume Model Generator (SFPGEN). A pre/post processing graphics system utilizing the NCAR graphics package was developed. The pre-processing graphics system provides the capability to view the individual subshapes or the composite body (with or without shading) prior to PLIMP execution to ensure correct model geometry. The post processor enables the user to view 3D geometric object(s) with color contours representing surface conditions such as temperature, pressure, heating rate, etc. A Plume Handbook detailing the processes necessary to perform rapid assessment of plume impingement scenarios was the principal output of this research. The Handbook consists of two volumes. One volume describes the overall process of generating plume impingement environments with PLIMP from various plume flowfield sources. The second volume is an updated PLIMP specific input/output guide.

RESULTS Selected analytical/experimental data comparisons were performed to demonstrate the validity of the analytical (modified PLIMP code) approach to plume impingement analysis. Sample cases were executed to demonstrate the pre/post processing graphics system and aid the user in familiarization and preparation of input data for the modified PLIMP code. A database of precomputed plume flowfields which can be used by PLIMP to predict high altitude plume induced environments was developed. Space Shuttle RCS and Orbital Maneuvering System (OMS) RCS are examples of some of the plume flowfields included in this database.

POTENTIAL APPLICATIONS The evaluator will be applicable to all current and future NASA missions where thrusters are utilized in close proximity to spacecraft and propulsion hardware. Thermal protection systems and contamination minimization schemes can be derived from assessments based upon the evaluator.

NAME AND ADDRESS OF CONTRACTOR

REMTECH INC.
3304 Westmill Drive
Huntsville, Alabama 35805

PRINCIPAL INVESTIGATOR

Robert L. Bender

FOREWORD

This document presents the latest version of the Plume Impingement Computer Program (PLIMP) and discusses previous capabilities and additional and revised capabilities. It is a compilation of a number of reports and studies from 1985 to 1991 documenting various changes. It also reports very recent changes which have not been documented anywhere else. This report consists of two volumes; one describes the theoretical bases for the program and the other is the PLIMP user's input guide.

We have reported the details necessary for new and previous users to implement the program. We have not discussed in fine detail the information available in the previous documentation, but have referred the user to that documentation if he desires more explanation.

The NASA/MSFC Contracting Officer's Technical Representative for this contract was Mr. Peter Sulyma, of the Induced Environments Branch, Aerophysics Division of the Structures and Dynamics Laboratory, ED33.

Contents

FOREWORD i

List of Figures iv

List of Tables vi

1 INTRODUCTION 1

 1.1 Background and Problem Description 1

 1.2 Scope 1

 1.3 New PLIMP Code 2

2 PLUME CALCULATION 3

 2.1 Method of Characteristics (MOC) 3

 2.2 RAMP2 6

 2.3 SPF/2 12

3 PLIMP PROGRAM 21

 3.1 General Description 21

 3.2 Previous Capabilities 21

 3.2.1 Surface Geometry 21

 3.2.1.1 Subshapes 21

 3.2.1.2 Rotation of Axes 27

 3.2.2 Impingement Properties 28

 3.2.3 Impingement Pressure 28

 3.2.4 Forces and Moments 31

 3.2.5 Heating Rates 35

 3.2.6 Shading 39

 3.3 Changes and Added Capabilities 43

 3.3.1 Internal Improvements 43

 3.3.2 Particle Impingement 43

 3.3.3 SFPGEN 44

 3.3.4 Contamination Determination 45

 3.3.5 Graphics 45

 3.3.5.1 Introduction 45

 3.3.5.2 Subshape Drawing 47

 3.3.5.3 Code Execution and Use 62

3.4 Ordered Flowfields 63

 3.4.1 Bi-Propellant Engines 63

 3.4.2 H2/O2 Engines 64

 3.4.3 Hydrazine Engines 64

 3.4.4 Cold Gas Thrusters 64

 3.4.5 Solid Propellant Engines 65

3.5 Sample Problems 92

 3.5.1 Sample Case 1 92

 3.5.2 Sample Case 2 92

4 References 100

Appendix A Experimental Verification A1

 A.1 AEDC Tests A1

 A.1.1 Introduction A1

 A.1.2 Analytical Simulation A2

 A.1.2.1 Plume Analysis A2

 A.1.2.2 Impingement Analysis A5

 A.1.3 Results A14

 A.2 Ariane Tests A14

 A.2.1 Introduction A14

 A.2.2 Analytical Simulation A18

 A.2.2.1 Plume Analysis A18

 A.2.2.2 Impingement Analysis A18

 A.2.3 Results A18

 A.3 Conclusions A18

 A.4 References A21

Appendix B Description of Taped Program Code Input and Output Flowfield Files . B1

List of Figures

1	Flow Chart for Creating PLIMP Input File from MOC Program	5
2	Reflecting a Right-Running Shock Hitting the Axis of Symmetry	7
3	Reflecting a Right-Running Shock Hitting a Mach Disc	7
4	Sample MOC Problem with One Compression Corner	8
5	Sample MOC Problem with Two Shocks	8
6	Sample MOC Problems for External Flows	8
7	Sequencing and Communication of the RAMP2 Programs	11
8	Plume Flowfield Showing Structures Accounted for in SPF/2	13
9	Component Structure of SPF/2	16
10	SPF/2 Overlaying Sequence of Operations	19
11	PLIMP Coordinate Systems	22
12	Subshape Coordinate Systems and Parameters	23
13	Rotation Angles Between Coordinate Systems	28
14	Empirical Fit of Newtonian Coefficient	30
15	Force and Moment System	31
16	Conical Subshape C.P. Location	33
17	Rectangular, Right Triangular and Trapezoid Plate Subshape C.P. Location . . .	34
18	Circular Plate Subshape C.P. Location	34
19	Body of Revolution Subshape C.P. Location	35
20	Vectors for Determining Self-Shading by Subshape Element	40
21	Vectors for Determining Shading of One Subshape by Another	41
22	Flow Chart for Graphics Program	48
23	Plane Generation for the Conic or Body of Revolution Subshapes	50
24	Plane Generation for Rectangular Plate Subshape	51
25	Plane Generation for Circular Plate Subshape	52
26	Plane Generation for Triangular Plate Subshape	53
27	Input for Preprocessing Subshapes	54
28	Shading Determination Using Summation of Angles at Vertices	56
29	"Bleed-Through" Caused by Centroid Shading but Element Not Completely Shaded	57
30	Preprocessing Results with No Shading	58
31	Preprocessing Results with Predicted Shading	59
32	Postprocessing Results — Top View	60
33	Postprocessing Results — Bottom View	61
34	Density Contours: Space Shuttle Vernier RCS Engine	67
35	Density Contours: Space Shuttle Primary RCS Engine ($A/A^* = 22$) Constant O/F .	68
36	Density Contours: Space Shuttle Primary RCS Engine ($A/A^* = 22$) Variable O/F .	69
37	Density Contours: AJ10-181 ($A/A^* = 93$; 5 lbf Thrust)	70
38	Density Contours: BP14 ($A/A^* = 45$; 21 lbf Thrust)	71
39	Density Contours: Marquart R2 (11 lbf Thrust)	72
40	Density Contours: R6C ($A/A^* = 150$; 5 lbf Thrust)	73
41	Density Contours: Space Station ACS Engine	74

42 Density Contours: Nuclear Engine (Solid Cone; $A/A^* = 200$; 70,000 lbf Thrust) . 75

43 Density Contours: 0.5 Newton Hydrazine Engine ($A/A^* = 41$) 76

44 Density Contours: 1 lbf Thrust Hydrazine Engine ($A/A^* = 50$) 77

45 Density Contours: REA-MONO-A (30 lbf Thrust; $A/A^* = 79$) 78

46 Density Contours: MRE15 (OMV RCS) ($A/A^* = 50$) 79

47 Density Contours: AFE RCS 30 lbf 80

48 Density Contours: 7.49 lbf Hydrazine Engine ($A/A^* = 50$) 81

49 Density Contours: REA 15 ($A/A^* = 50$) 82

50 Density Contours: AFE Gaseous Helium Thruster 83

51 Density Contours: OMV Nitrogen Thruster 84

52 Density Contours: AEDC CO2 Sonic Orifice 85

53 Density Contours: Space Station EVA Free Air Sonic Vent (4 In. Diameter) . . . 86

54 Density Contours: Space Station EVA Stringer Air Vent (1 In. Diameter) 87

55 Density Contours: Space Station EVA Stringer Air Vent (4 In. Diameter) 88

56 Density Contours: Space Station Hyperbaric Air Vent 89

57 Density Contours: JPL GN2 Nozzle 90

58 Density Contours: STAR63 (AFE Ignition Motor) 91

59 Sample Case 1 — Impingement Pressure (View 1) 96

60 Sample Case 1 — Impingement Pressure (View 2) 97

61 Sample Case 2 — Impingement Pressure (View 1) 98

62 Sample Case 2 — Impingement Pressure (View 2) 99

A1 Test Installation A1

A2 PLIMP Input Geometry for AEDC Test Comparison A5

A3 Analytical/Experimental Heating Rate Comparison for AEDC Case #1 along the Engine Centerline ($A/A^* = 10$, $h = 3R_e$, $\delta = 0$ Deg) A9

A4 Analytical/Experimental Surface Pressure Comparison for AEDC Case #1 along the Engine Centerline ($A/A^* = 10$, $h = 3R_e$, $\delta = 0$ Deg) A10

A5 Analytical/Experimental Heating Rate Comparison for AEDC Case #2 along the Engine Centerline ($A/A^* = 40$, $h = 3R_e$, $\delta = 0$ Deg) A11

A6 Analytical/Experimental Heating Rate Comparison for AEDC Case #3 along the Engine Centerline ($A/A^* = 40$, $h = 3R_e$, $\delta = 10$ Deg) A12

A7 Analytical/Experimental Heating Rate Comparison with Distance from the Engine Centerline for AEDC Case #3 ($A/A^* = 40$, $h = 3R_e$, $\delta = 10$ Deg) A13

A8 Ariane Configuration with Plume Due to Retro-rocket Firing A15

A9 Position of Antennas #1 and #2 on the Cylindrical Model A17

A10 Position of Antennas #3 and #4 on the Cylindrical Model A17

A11 Analytical/Experimental Heating Rate Comparison on Antenna #1 with Axial Distance ($\alpha = 11$ Deg) A23

A12 Analytical/Experimental Heating Rate Comparison on Antenna #2 with Axial Distance ($\alpha = 11$ Deg) A24

A13 Analytical/Experimental Heating Rate Comparison on Antenna #4 with Axial Distance ($\alpha = 11$ Deg) A25

List of Tables

1	Chemical Systems in SPF/2	17
2	Important Subshape Parameters Calculated by PLIMP	26
3	Species Contained in PLIMP Data File	46
4	Flowfields Generated for "Canned" Plume Data Base	65
5	PLIMP Input File for Sample Case 1	93
6	PLIMP Input File for Sample Case 2	94
A1	Engine Operating Characteristics and Nozzle Geometry	A3
A2	Bipropellant, Equilibrium/Frozen, Constant O/F with Variable Total Enthalpy Tables	A4
A3	AEDC Test RAMP2 Input File ($A/A^* = 10$)	A6
A4	AEDC Test RAMP2 Input File ($A/A^* = 40$)	A7
A5	AEDC Test PLIMP Input Files for Cases #1, #2, #3	A8
A6	Ariane Engine Operating Characteristics (Data Obtained from Ref. [A4])	A16
A7	RAMP2 Input File for Ariane Tests	A19
A8	PLIMP Input File for Ariane Tests (Antennas #3 and #4 with $\alpha = 11$ Deg) . .	A20
A9	Maximum Heating Rates for Ariane Tests on Antennas #1, #2, #3, and #4 at Various Engine Cants (α)	A21

Section 1 INTRODUCTION

1.1 Background and Problem Description

When a rocket engine is fired at high altitudes, exhaust gases expand into a large solid angle, and impingement on nearby surfaces cannot be avoided. There are numerous situations in which impingement is encountered, some examples are: the operation of stabilization and maneuver thrusters, multiple satellite launching, launching a reusable spacecraft, and launcher stage separation. Undesirable consequences resulting from exhaust plume impingement include additional forces and torques exerted on the spacecraft, surface heating, contamination (with possible damage to solar cells, optics and antennas) and electrical charging. The exhaust plume impingement pressure and heat transfer phenomena also complicate the environment to which the spacecraft and its functional surfaces are exposed. It is difficult to experimentally investigate potential exhaust plume impingement possibilities early in spacecraft development, when configuration and operational timelines are not finalized. Therefore, reliable simulation methods for investigating the interactions of rocket plumes with spacecraft are needed, thus allowing spacecraft or satellite designers the opportunity to simulate and assess impingement effects on hardware prior to flight.

The Plume Impingement Computer Program (PLIMP) is such a simulation method. Originally developed by Lockheed-Huntsville to assess impingement environments, this program calculates impact pressure distributions, integrated pressure forces, resulting moments and heating rates, and contamination to bodies immersed in rocket exhaust plume flowfields. The code has undergone continuous development and modifications over the past twenty years and has wide acceptance in the plume technology community.

REMTECH, under NASA contract, has developed a quick impingement assessment tool, which is built around the modified PLIMP program. As part of this effort and to assist potential users in application of the methodology, a handbook for PLIMP was specified as an essential output of the REMTECH contract. This volume and Volume II, User's Manual, satisfy that requirement and contain the necessary information in handbook format to quickly use the PLIMP program for any plume impingement scenario.

1.2 Scope

This volume explains the plume calculation methods available, describes the program with emphasis on recent changes and added capabilities, and details the ordered flowfields currently in storage. It also documents PLIMP's analytical heating rate computations which are validated by experimental data.

The handbook is not intended to address the general problems of vacuum plume impingement simulation, which are beyond the scope of the REMTECH contract, nor is it comprehensive in its treatment of specific impingement phenomena. Rather, it tells

the reader the background and bases for the plume generation and PLIMP programs, how to use them to simulate an impingement scenario, how the results are presented, and the general level of accuracy provided by this method. The limitations and program restraints are explained in detail such that the user can decide if this methodology is appropriate for the problem of interest.

1.3 New PLIMP Code

During the performance of this contract, the PLIMP program was updated and streamlined to affect a faster solution, more compatible input, and more useful output. The remodeled code is now an ANSI Standard program with metric input/output options, single run capability for two-phase impingement solutions, and detailed output information. A preprocessing graphics display of the user-provided input geometry was also developed so that surfaces can be adjusted by the user for the proper orientation prior to running PLIMP. Likely shaded areas are also identified by this display. A postprocessing display is available for showing the color-coded output parameters (pressure, temperature, heat rate, etc.) on the surfaces. The PLIMP program was also expanded to include predicted contamination of impinged surfaces by particles and condensing gases. Details of the recent modifications and discussions of the new PLIMP versus the original program are provided in Section 3.0.

Section 2

PLUME CALCULATION

A number of programs are available for plume generation; however, the ones typically used for the PLIMP program calculations are MOC, RAMP2, and SPF/2. Each of these has useful qualities and their specific attributes are discussed in the subsequent subsections.

2.1 Method of Characteristics (MOC)

Lockheed's MOC program [1] has been in existence over 20 years and is the original code used to generate flowfields for PLIMP. It is used for predicting the gas dynamic parameters of single phase, real gas, inviscid supersonic flows of adiabatic reacting gases in thermal equilibrium. The most frequent use of this program has been in calculating rocket nozzle and exhaust plume flows. It is not limited to this and has also been used to calculate external supersonic flow over solid bodies.

The MOC program has a number of basic capabilities, some of which are:

1. The gas may be ideal or real. If real, frozen or equilibrium assumptions can be made. Oxidizer/fuel gradients may be considered.
2. Two-dimensional or axisymmetric problem geometry can be used.
3. Both upper and lower boundaries can be solid or free. (A solid boundary can be approximated by either a conic or polynomial equation.)
4. A nozzle wall may be curve fit with discrete points.
5. One compression corner on the upper wall and the subsequent shock can be calculated. (Any number may be considered if the problem is re-started each time.)
6. The number of Prandtl-Meyer rays to be computed around expansion corner discontinuities may be input.
7. Any number of expansion corners can be considered on either the upper or lower wall.
8. Various methods for obtaining an initial start line are available.
 - The program will calculate a one-dimensional start line anywhere in the nozzle.
 - The program will calculate a start line at points within the nozzle necessary to conserve mass.
 - Characteristic data can be input at points across the flowfield within the nozzle or in the plume.
 - Any right running characteristic line can be used for a start line.
 - Any left running characteristic line can be used (may be in combination with a normal start line).
 - Any left running line may be input with a right running shock crossing it.

- 9. The approach flow may be hypersonic or quiescent.
- 10. Exit to ambient pressure ratios from over-expanded to highly under-expanded flows are possible.
- 11. Viscous boundary layer approximations at the nozzle lip are available.
- 12. Displacement of the axis of symmetry from the center of flow (i.e., the plug nozzle flowfield) is possible.
- 13. Reacting gas solutions which are in chemical equilibrium have been facilitated by providing a binary tape from TRAN72 [2] of its equilibrium or frozen real gas calculations at any desired O/F ratio(s) or total enthalpy(s). The MOC program has the capability of selecting the proper case from a large set of real gas properties cases stored on a master tape. Cases stored are uniquely identified by some characteristics of the particular gas under consideration. For example, a LOX/LH₂ system may be identified by the following:

<u>Gas Type</u>	<u>Mixture Ratio</u>	<u>Chamber Pressure</u>
O ₂ /H ₂	O/F = 1.5 - 8.0	PC = 546.0

New cases of the general interest may be added to the master tape; however, ad hoc cases should be prepared on a separate tape.

- 14. Once the flowfield solution has been obtained, the output file may be used by the MOC Radial Lookup Program which determines the radial variations of flowfield properties across the nozzle and plume flowfields at constant axial stations.

The flow of information needed to obtain a PLIMP flowfield input from the MOC Program is shown in Fig. 1. Three separate programs are involved: (1) the NASA/LeRC TRAN72; (2) a program for generating an MOC compatible file (TAPGEN); and (3) the MOC Program.

The TRAN72 program has data on all typical aerospace oxidizers and fuels and computes the chemical species in a flow given the oxidizer, fuel, O/F ratio, and pressure. The resultant species' temperature, enthalpy, entropy, molecular weight, and isentropic exponent are calculated for ideal, frozen, and equilibrium conditions. These results are output in a binary form which is transformed by TAPGEN into a format compatible to the MOC Program input. Each of the three programs must be called by separate control statements.

The MOC Program has two major components as seen in Fig. 1: (1) the MOC nozzle solution, and (2) the MOC plume solution. The nozzle solution is used when solid boundaries are specified. Characteristic lines are computed from a supersonic start line (usually the nozzle throat for a rocket nozzle) to the solid boundary. The solution scheme changes when a line goes outside a solid boundary. The flowfield is recalculated using a compression or a Prandtl-Meyer expansion algorithm as determined by the exit and ambient pressures. The compression calculation will also generate a shock.

Only one compression corner is allowed, because the program is normally restricted to a single shock within the flowfield. Also, only right-running shocks can be handled, thus no provision exists for compression corners on the lower wall. When a shock intersects

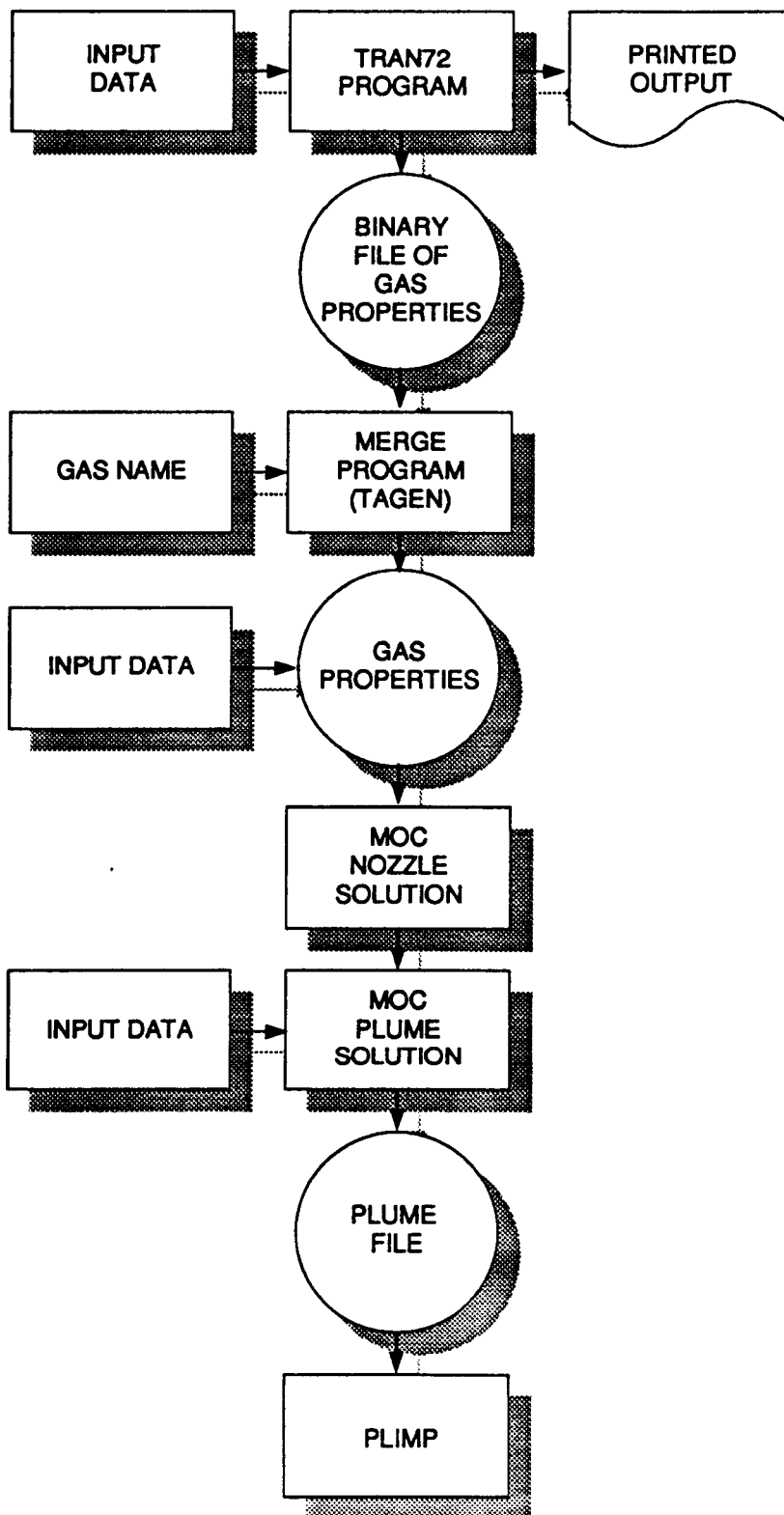


Figure 1: Flow Chart for Creating PLIMP Input File from MOC Program

the plume axis, it may be automatically reflected because the program will handle two shocks if the first terminates by intersecting a lower free boundary. Shocks may also be reflected by inverting the last characteristic line [using negative Y values (2D) or R values (axisymmetric)] and rerunning the program with this line as the start (Fig. 2).

When a restart is required for a shock which has terminated at a "Mach Disc," a boundary equation simulating a cylindrical "pipe" must be used to approximate the subsonic region (Fig. 3). This is a loose approximation and is not as good as the plume flow programs discussed below.

The shock will continue to be calculated until the change in stagnation pressure becomes less than a given input percentage. After the criterion is satisfied, the shock will no longer be iterated. If a value for the percentage change is not provided in the input, the default value is 0.1 psid.

Solid boundaries can be described by a set of discrete points. The set of points is spline fit with individual polynomials for each pair of points, according to the polynomial boundary option selected by the user.

The program computes nozzle thrust by integrating the pressure distribution along the nozzle wall, including the thrust increment between the last characteristic line inside the nozzle and the Prandtl-Meter expansion at the nozzle lip. The vacuum specific impulse and nozzle thrust coefficient at each nozzle wall point is also calculated.

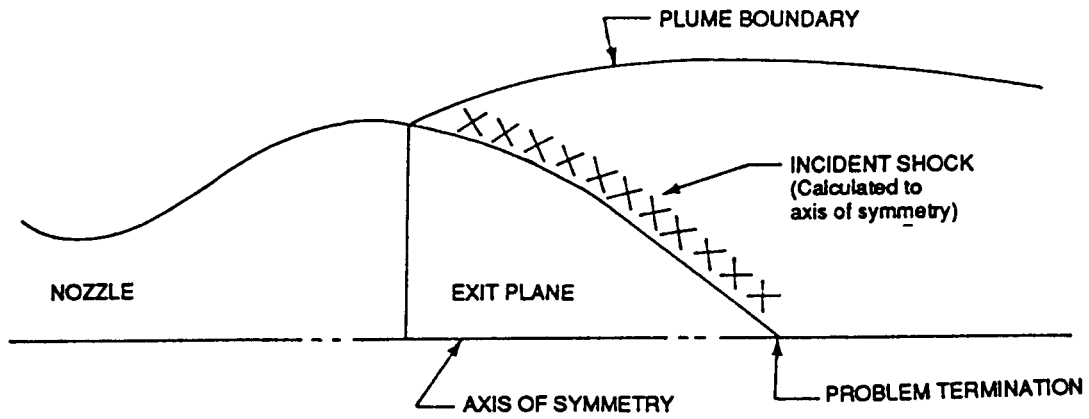
The most common applications of this program are in the areas of standard rocket nozzles and axisymmetric plumes. Many other complex flowfields can be treated, however, using the various options. To illustrate this, Fig. 4 shows a supersonic, two-dimensional flowfield with angular boundaries restricting the flow. The MOC-generated flow structures are shown and, while only one compression corner can be modeled, this example could have had more than two expansion corners illustrating a more complex case. Although this example is two-dimensional, it could easily have been axisymmetric.

Another sample problem is shown in Fig 5. This shows that two shocks can be calculated in one flowfield if the shock ends in a lower free boundary.

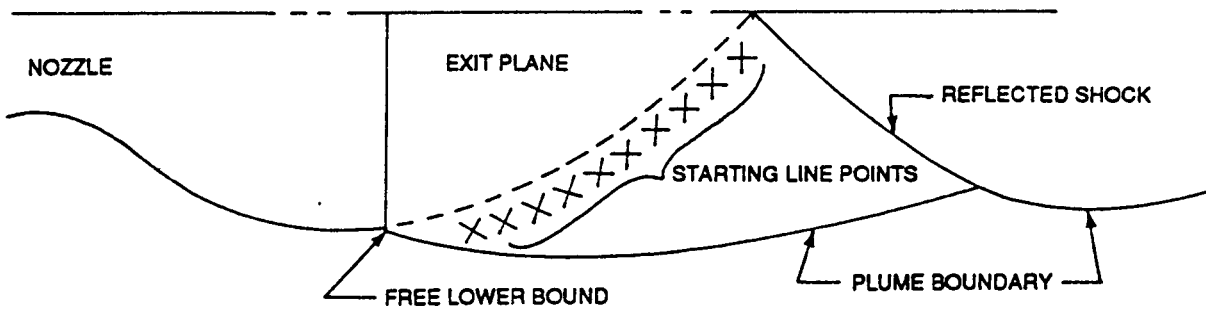
External flow (shown in Fig. 6) is simulated by specifying the necessary stagnation conditions and inserting a two-dimensional or axisymmetric object in the flowfield. The restriction that the flow remain supersonic (inherent in the method-of-characteristics solution) must be observed throughout all flowfields.

2.2 RAMP2

The ReActing Multiphase Plume Flowfield Program — Version 2, RAMP2 [3], was designed to calculate high altitude rocket exhaust plumes. It uses a method-of-characteristics solution to calculate a flowfield but has many additional capabilities that do not exist in the MOC Program. It can account for the effects of boundary layers, chemistry, two-phase flow, free molecular flow and a number of other phenomena which affect the characteristics of nozzle and exhaust plume flowfields. The ability of the RAMP2 program to treat single and two



a) Initial Run



b) Restarted Run

Figure 2: Reflecting a Right-Running Shock Hitting the Axis of Symmetry [1]

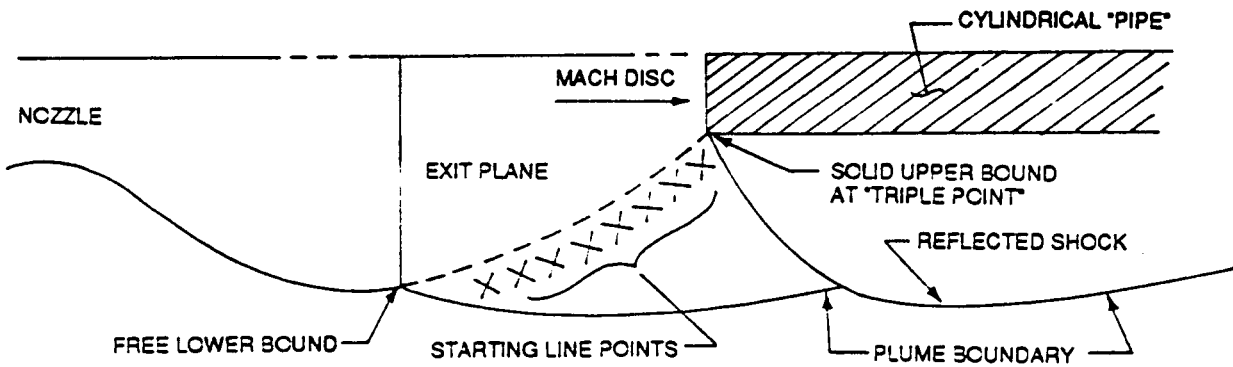


Figure 3: Reflecting a Right-Running Shock Hitting a Mach Disc [1]

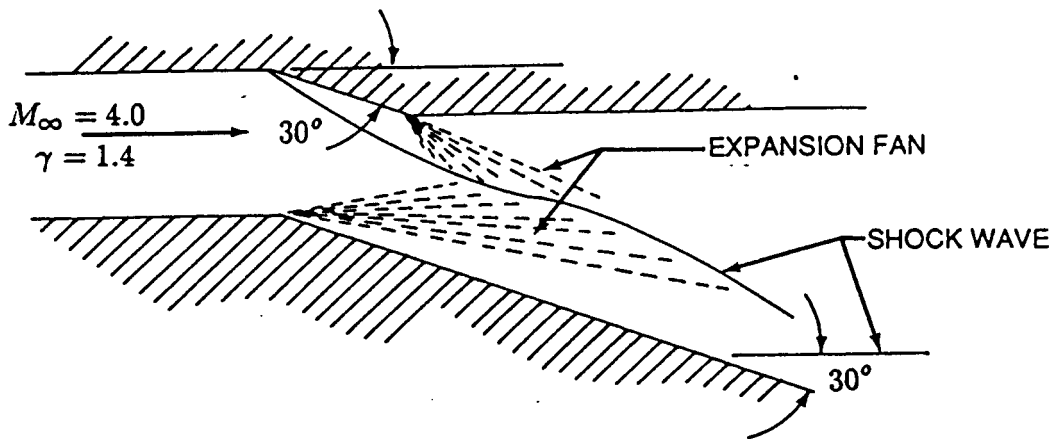


Figure 4: Sample MOC Problem with One Compression Corner [1]

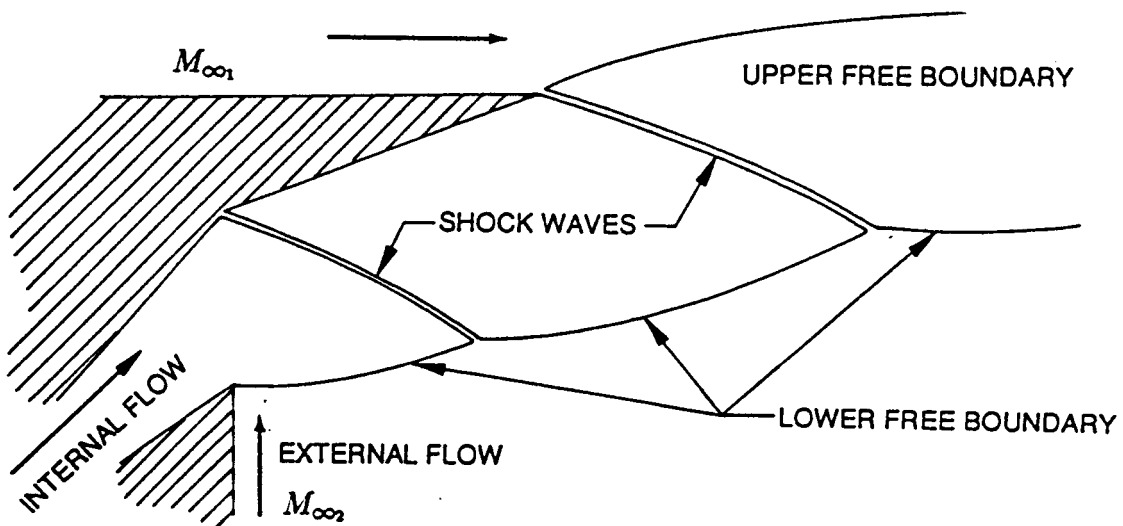


Figure 5: Sample MOC Problem with Two Shocks [1]

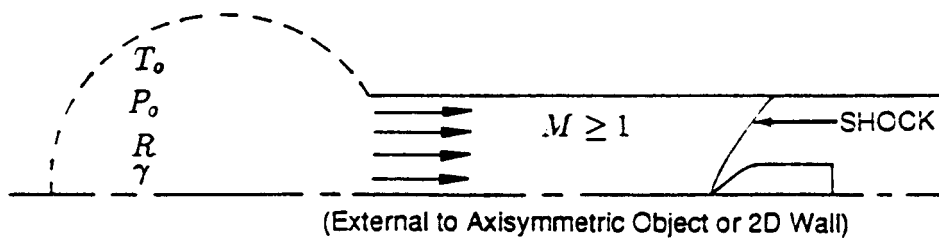


Figure 6: Sample MOC Problems for External Flows [1]

phase flows has led to the application of the program to solve a wide range of problems associated with real gas, supersonic, compressible flow. Some of the more important basic capabilities and limitations of the existing program are:

1. The gas may be ideal or real. If the gas is real, frozen, equilibrium, or non-equilibrium, chemistry assumptions can be made. The effects of oxidizer/fuel gradients may be considered.
2. Two-dimensional or axisymmetric flow problem geometries can be selected.
3. Both upper and lower boundaries can be solid or free. (A solid boundary can be approximated by either a conic or polynomial equation.) (Two-phase problems require the nozzle centerline as a lower boundary.)
4. A nozzle wall may be curve fit with discrete points.
5. Any number of expansion corners can be considered on either the upper or lower walls.
6. Various methods for obtaining an initial start line are available.
 - a. The program will calculate a one-dimensional startline anywhere in the nozzle.
 - b. Data on a normal surface can be input at points across the flowfield within the nozzle or in the plume.
 - c. An exit plane startline can be stored.
 - d. The program can be restarted from a stored startline.
 - A single phase startline can be calculated using a transonic solution which can handle ideal gas or equilibrium chemistry for both constant and variable oxidizer/fuel ratios.
 - A two-phase startline can be set up using a transonic solution.
7. Hypersonic or quiescent approach flow options may be used.
8. Exit to ambient pressure ratios from overexpanded to highly underexpanded are possible.
9. Displacement of the axis of symmetry from the center of flow (i.e., the plug nozzle flowfield) is possible for gas only cases.
10. There is presently a maximum of 100 points on a normal and 100 input points.
11. The reacting gas solutions are generated by TRAN72.
12. The program has a radial lookup routine like that of the MOC.
13. By appropriate description of the flow boundaries, it is possible to change from a solid to free boundary on either the upper or lower walls. Conversely, it is not possible to change from a free to a solid boundary on either wall.
14. A real gas nozzle boundary layer solution can be performed with no interface between the user and the RAMP2 results. Frozen equilibrium chemistry with turbulent or laminar solution is possible.
15. The effect of a nozzle wall boundary layer on particles which enter the boundary layer is treated.
16. An exit plane startline can be generated for the SPF/2 and SFPGEN programs (discussed in Sections 2.3 and 3.3) which include two-phase flow and boundary layer effects.

17. Multiple passes through the inviscid nozzle solution with the nozzle contour modified by the BLIMPJ solution displacement thickness is not possible.
18. High altitude rarefied plumes may be treated with either continuum or sudden freeze, free molecular flow assumptions.
19. Nozzle shocks can be treated using a shock capturing methodology or can be treated isentropically using the streamline normal solution.
20. When the continuum treatment of rarefied plumes is used, the plume may be solved only to the point where the gas velocity reaches 99.9 percent of its limiting velocity. Near the gas limiting velocity numerical problems can lead to a termination of the solution.

RAMP2 consists of three basic computational components: (1) TRAN72 which generates equilibrium thermodynamic and transport data, (2) RAMP2F which calculates the inviscid flowfield, and (3) BLIMPJ which computes a boundary layer in the nozzle. These components are actually separate programs and must be executed separately to avoid storage problems. However, temporary files are used to transfer the output of one to the input of the next so they act like one program. Figure 7 shows the major components and modules in RAMP2.

In general, in order to solve a high altitude plume the following steps are required. First, the TRAN72 program input data is prepared and executed to generate a data file describing the thermodynamic characteristics of the post-combustion gases. Next the RAMP2F flowfield data are prepared and the nozzle flowfield is solved using the TRAN72 program data file as input. Then in order to adequately describe the nozzle boundary layer, the BLIMPJ code is executed using an input data file and flowfield file generated by the RAMP2F nozzle solution. Finally, the exhaust plume is generated by using the nozzle solution and boundary layer solution to generate an exit plane start line that is used to initiate the plume solution. Thus, the generation of a high altitude plume can require up to four different executions of programs (TRAN72, RAMP2F, BLIMPJ, and RAMP2F) for the specification of the most detailed and accurate results. Physical input data are required only for the TRAN72 and first RAMP2F execution. All data required for the BLIMPJ code and second RAMP2F execution are generated internal to the program and/or communicated by data files and temporary files. Depending on the application, the problem or the level of sophistication required in the plume results it may not be necessary to run the TRAN72 or BLIMPJ codes. It is possible that a single RAMP2F calculation may be adequate.

As mentioned previously, the TRAN72 program generates thermodynamic data for the equilibrium/frozen post-combustion gases which are used in the flowfield calculations performed by RAMP2F. However, equilibrium/frozen thermodynamic data can be input if the data were generated using some other method in which case it is not necessary to execute the TRAN72 program. It is also possible that the propellant for the motor might be an ideal gas (e.g., nitrogen jet) in which case the gas thermodynamic data can be input directly into the RAMP2F code. Finally, the user may decide that a finite rate or frozen chemistry solution is required in which case the reaction package and individual species thermodynamics are input directly into the RAMP2F code.

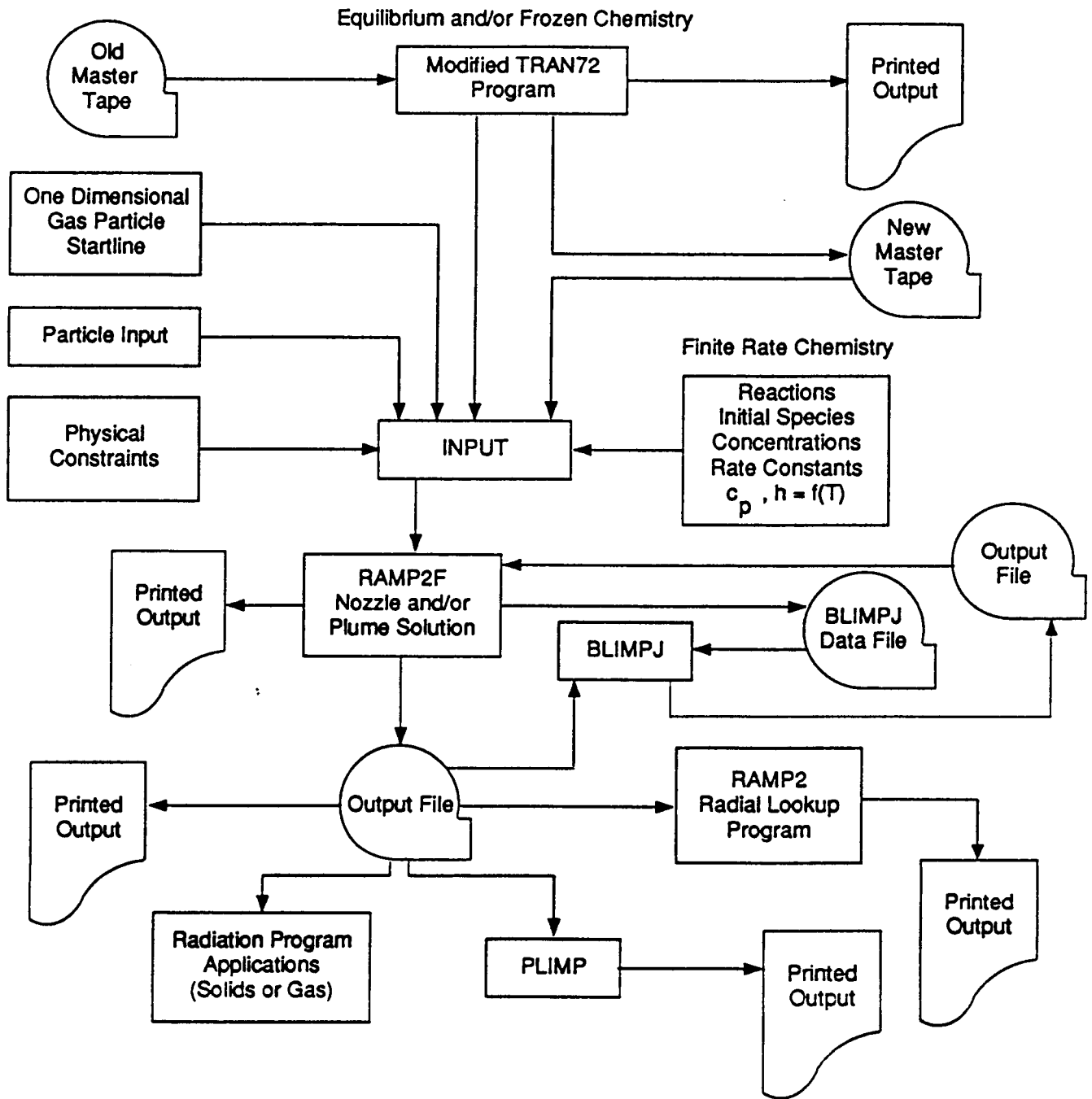


Figure 7: Sequencing and Communication of the RAMP2 Programs [3]

If the user has an application in which nozzle boundary layer effects are not important then it is not necessary to execute the BLIMPJ code. A single RAMP2F flowfield calculation starting at the throat or at the exit plane can then be made to generate the exhaust flowfield.

Thus, numerous combinations of program executions are possible, depending on what the user requires as results. Additionally, the TRAN72 program may be executed alone if the results are required for some use other than for RAMP2F. It is possible to execute the BLIMPJ as a stand-alone program, but some minor program modifications are required to change the input file numbers and omit reference to flowfield data files that come from the RAMP2F nozzle solution.

Typical uses of RAMP2 have been in the analysis of:

1. Analyzed Space Shuttle RCS motor combustion chamber, nozzle and exhaust plume. Utilized equilibrium/frozen chemistry, variable O/F transonic solution and boundary layer effects [4].
2. Space Shuttle Solid Rocket Motor
 - a. Equilibrium/frozen nozzle/plumes at various altitudes and operation conditions for base heating application [5].
 - b. Sea level plume for Space Shuttle mobile launcher design environment [6].
 - c. High altitude plume calculation including finite rate chemistry for application to range safety plume radar cross-section determination [7].
3. Space Shuttle separation motor nozzle/plume solutions for determination of stage separation impingement environments on Orbiter/ET combination [8].
4. Small solid rocket motor nozzle and plumes to determine how best to apply the program for making nozzle and plume calculations. Compared RAMP2 results with experimental nozzle and plume data [9].
5. High altitude interim upper stage motor plumes. Particulate flowfields were to be used for determination of possible orbiter heat shield damage during various satellite deployment scenarios [10].
6. Detailed combustion chamber and nozzle flowfields for comparisons with exit plane radiation measurements to determine the best analytic models for performing combustion chamber/nozzle calculations [11].
7. IR irradiance on a vehicle-borne sensor arising from a plume emitted by a thruster on the vehicle in an exoatmospheric environment. [12].

2.3 SPF/2

JANNAF's Standardized Plume Flowfield program, second version, SPF/2 [13], is used for predicting the gas dynamic structure of two phase, low attitude (<70 km) rocket exhaust plumes. Its main use is calculating plume signatures and plume impingement conditions and is designed for single nozzle exhausts at zero angle of attack. Figure 8 shows the regions of the plume modeled by SPF/2. The program models the shock structure and the thin shear layer in the near field of the plume by overlaying a viscous

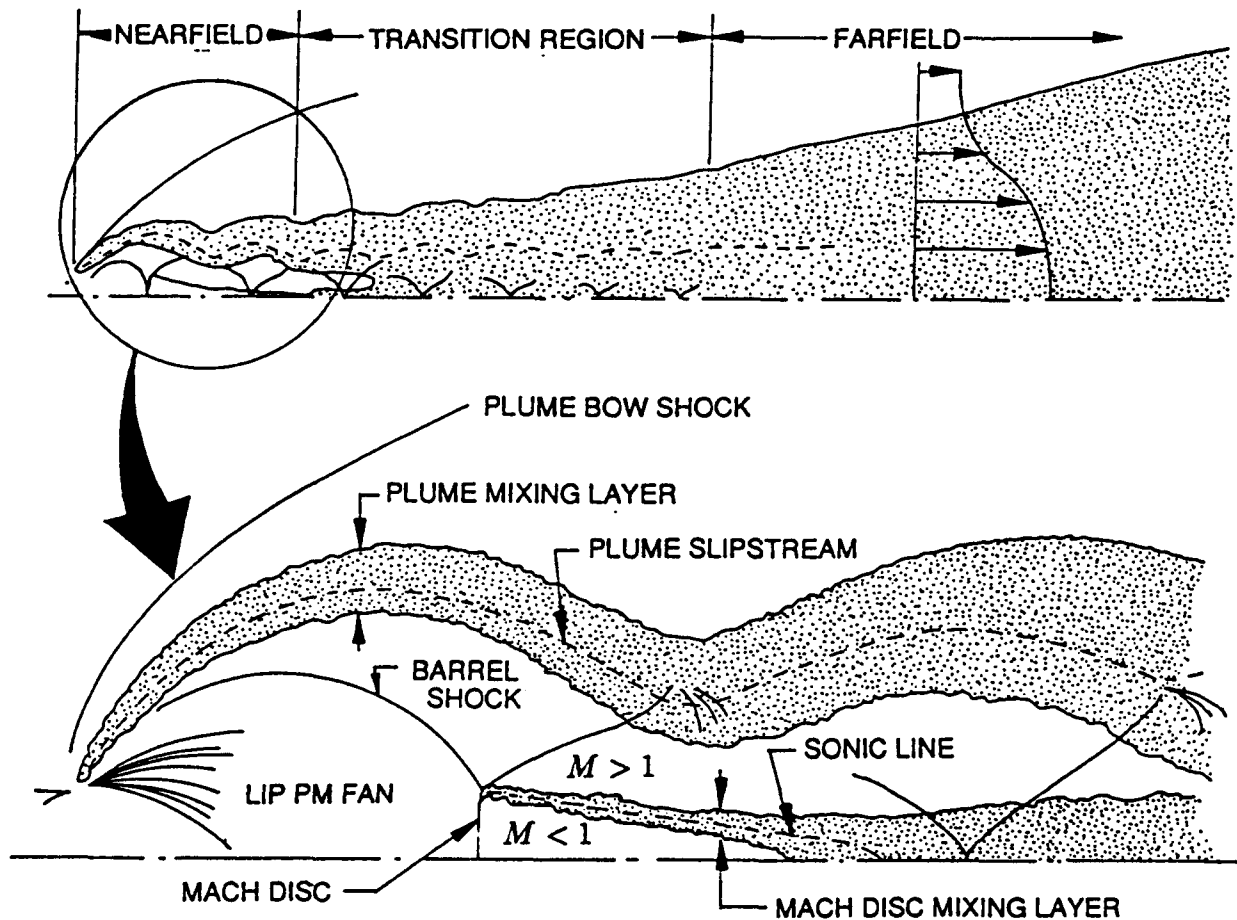


Figure 8: Plume Flowfield Showing Structures Accounted for in SPF/2 [13]

plume calculation on the inviscid one. The pressure in this region is determined by the shock-capturing method. Downstream of the near field the pressure is decayed until ambient and is subsequently modeled as constant in the far field for the mixing and afterburning calculations. The program does not account for the weaker wave structure in the viscous transitional region where the wave and mixing processes are strongly coupled.

Several aspects of SPF/2 make it superior at low altitudes to other programs. It accounts for full gas/particle nonequilibrium effects in the inviscid plume and in the near field, transitional, and far field mixing regions. Also the subsonic/supersonic turbulent mixing flow downstream of a Mach disc has been modeled using a parabolized Navier-Stokes (PNS) technique. Another improvement is that inviscid gas-only plumes with expansion angles greater than 90 degrees can be considered.

The user inputs the chemical system to be used, run options, nozzle exit plane properties (both gaseous and particulate) and external flow conditions. He must choose from any of six pre-defined chemical systems with user specified modifications or a

completely user-defined chemical system. In addition, the user can choose from three modes of operation. These are:

1. A shock-capturing inviscid mode,
2. A turbulent mixing constant pressure mode, or
3. An overlaid mode.

For these three run options, the user can

1. Select a turbulence model,
2. Calculate the gas/particle interactions using a full nonequilibrium, equilibrium or 'mixed' approach,
3. Select from two particle drag/heat transfer laws,
4. Choose froze, equilibrium or nonequilibrium chemistry, and
5. Select from three external flow rules (depending on the flight condition) which relate the external pressure to the inviscid plume boundary inclination angle.

The initial conditions specified at the nozzle exit plane must contain profiles of velocity, temperature, pressure and composition for the gas-phase. Profiles of velocity, temperature (or enthalpy) and particle cloud density are also required for each particle size group considered. Particles can either be liquid or solid with phase change thermodynamics taken into account using particulate enthalpy curve fits. Currently, only Al_2O_3 enthalpy curves are coded into SPF/2. The external flow conditions at the nozzle exit plane are assumed to be those of the undisturbed free stream, although they can be user-specified. The upstream disturbance of the external flow by the vehicle and the plume (i.e., plume-induced separation) is not automatically taken into account. This limitation is being addressed in a current JANNAF-sponsored effort which uses the SPF/2 component to analyze plume/vehicle interactions for vehicles with significant base regions.

The following assumptions were made in deriving the two-phase flow equations from the Cartesian/cylindrical Navier-Stokes equations:

Gas-Phase

1. The viscous terms in the streamwise direction are negligible in comparison to the normal/radial terms (i.e., the standard parabolization of the Navier-Stokes equations).
2. The turbulent density correlations as well as the third and higher-order turbulence correlations are negligible in comparison to the second-order correlations (i.e., the 'standard' incompressible assumptions).
3. The transport of heat and mass is the same such that the Lewis number is unity and only the laminar/turbulent Prandtl numbers appear in the energy and species transport equations.

Particles

1. The continuum of particle sizes can be represented by several groups of discrete particle sizes.
2. The particles can be represented by a 'continuum cloud' for each size group.

3. The volume occupied by the particles is negligible.
4. The particles do not interact with one another.
5. The only forces acting on the particles are viscous drag forces.
6. The particles are spherical in shape and chemically inert (no heterogeneous reactions) such that the total particle mass is constant.
7. The energy exchange between the gas and the particles is due to convection only.
8. There are no temperature gradients within the particles.
9. Particle terms such as Saffman lift, Magnus force, etc., are negligibly small.
10. Turbulent particle diffusivities can be related to that of the gas in terms of time scale ratios.

The SPF/2 program is organized into three linked components: (1) Processor Component, (2) Shocking-Capturing Component, and (3) Turbulent Mixing Component. Each is actually a separate and distinct computer code and consists of individual modules and subroutines, although some have essentially the same logic (Fig. 9).

The Processor Component reads the user input and creates input files for the Shock-Capturing and Turbulent Mixing Components. This component's Data Bank model contains thermodynamic data (molecular weights, heats of formation, and polynomial curve fits for the specific heat, enthalpy, and Gibbs free energy) from the JANNAF Thermochemical Tables and the TRAN72 program (Table 1). The Data Bank also contains the chemical reactions and rate coefficients for the six chemical systems. The thermodynamic and chemical kinetic data are processed to form curve fits and data arrays for the Shock-Capturing and the Turbulent Mixing Component input files. This component also creates laminar viscosity and thermal conductivity data curve fits so that the drag and heat transfer coefficients needed for calculating gas/particle interactions can be determined by the other components.

The Shock-Capturing Component uses shock-capturing to account for the detailed shock structure, and it computes gas/particle interactions using the local fluid viscosity and thermal conductivity curve fits from the Processor Component. The gas/particle nonequilibrium equation and viscous transport equations account for the nonequilibrium interaction between the gas and particle phases, the turbulent mixing of both phases, and finite-rate chemistry. Generally, however, the Shock-Capturing Component solves only the inviscid form of these equations (i.e., no gas or particle cloud viscosity, and no chemical reactions) for most of the plume near field using the chemical composition frozen at the nozzle exit plane. The only exception occurs when the barrel shock of an underexpanded plume is strong enough to produce a Mach disc. In this case the Shock-Capturing Component is applied for a distance of approximately two inviscid cells, which is coded as three times the distance to the Mach disc or shock reflection. The turbulent mixing form of the gas and particle equations is then solved within the Mach disc shear layer. The species continuity equation is also solved, but only to establish the mixing region; therefore, an inert dummy species is used for simplicity. Two data files, one for the gas and one for the particle properties, are then written to transfer to the Turbulent Mixing Component the data for shear layer calculations if this option has been user selected.

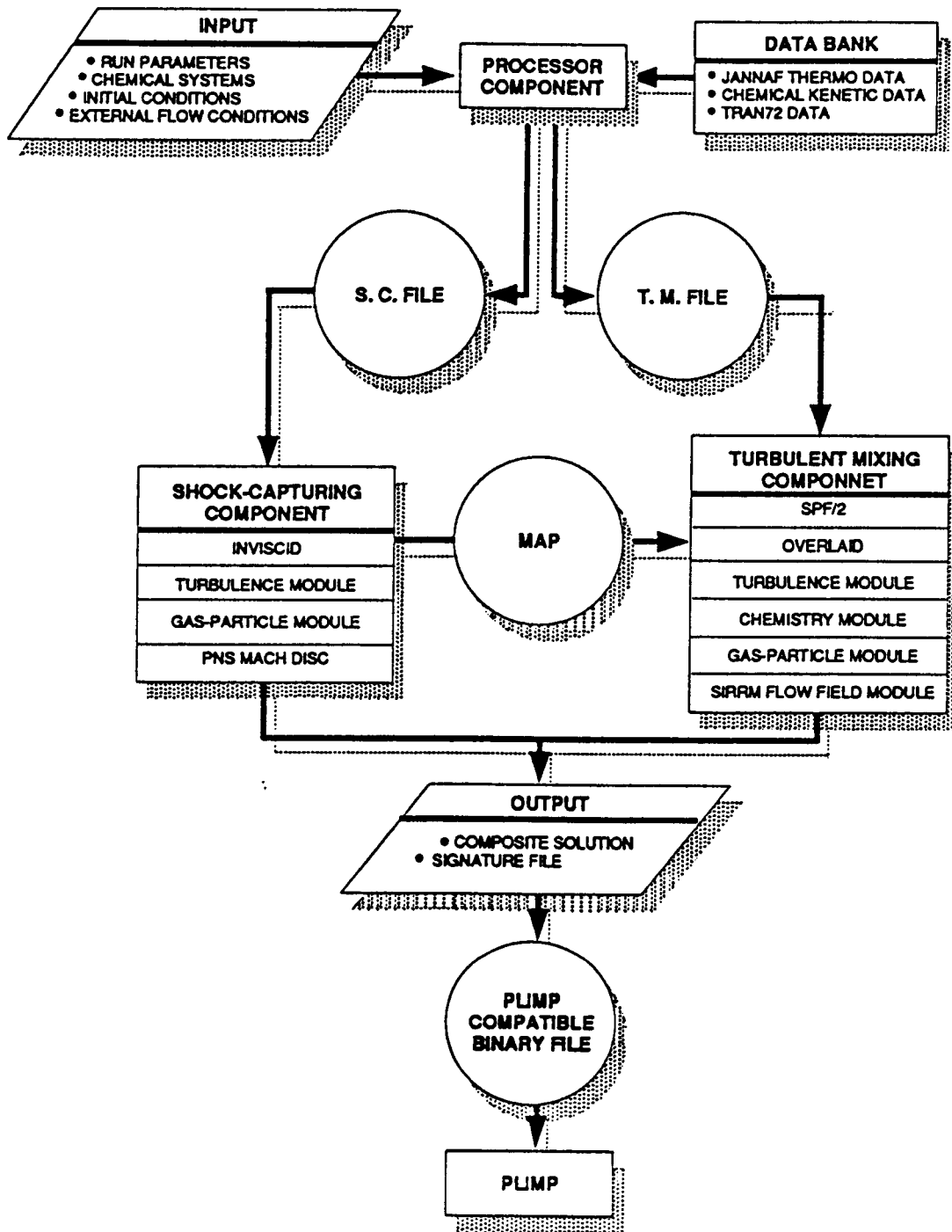


Figure 9: Component Structure of SPF/2 [13]

Table 1: Chemical Systems in SPF/2

Propellant Type	1 Liquid Hydrogen Oxygen	2 Liquid Amines Conventional Oxidizers (e.g., N ₂ O ₄) Solid Double Base (No AP)	3 Solid Composite (AP and Al)	4 Liquid Amines Inter-halogen oxidizers	5 Liquid B-containing fuels Conventional Oxidizers	6 Liquid B-containing fuels Inter-halogen oxidizers
Elements (All systems contain N ₂ as an inert species)	H/O	C/H/O	C/H/O/Cl	C/H/O/Cl/F	H/O/B	H/O/B/Cl/F
Number of Species (NS)	7	9	13	15	11	24
Number of Reactions (NR)	8	10	16	22	16	36
Species (Data Bank Number)	H(48) H ₂ (49) H ₂ O(50) H ₂ (66) O(85) OH(87) O ₂ (89)	CO(29) CO ₂ (30) H(48) H ₂ (49) H ₂ O(50) H ₂ (66) O(85) OH(87) O ₂ (89)	Al ₂ O ₃ CO(29) CO ₂ (30) Cl(35) Cl ₂ (39) H(48) H ₂ (49) H ₂ O(50) HCl(54) H ₂ (66) O(85) OH(87) O ₂ (89)	CO(29) CO ₂ (30) Cl(35) Cl ₂ (39) F(42) F ₂ (46) H(48) H ₂ (49) H ₂ O(50) HBO ₂ (52) H ₂ (66) O(85) OH(87) O ₂ (89)	BO(11) BO ₂ (15) B ₂ O ₃ (19) H(48) H ₂ (49) H ₂ O(50) HBO ₂ (52) H ₂ (66) O(85) OH(87) O ₂ (89)	BF(7) BF ₂ (8) BF ₃ (9) BO(11) BOCl(12) BOF(13) BO ₂ (15) B ₂ O ₃ (19) CO(29) CO ₂ (30) Cl(35) Cl ₂ (35) F(42) F ₂ (46) H(48)

A routine to extend the Shock-Capturing Component to treat gas-only exhausts (with jet pressure ratios, P_j/P_∞ , on the order of 2000 and larger) has been incorporated into SPF/2. This modification (for gas-only and gas/particle equilibrium flows) also allows SPF/2 calculations for intermediate and high altitude plumes, where the initial flow inclination angle can exceed 90. The modification, however, has not been thoroughly tested.

The Turbulent Mixing Component calculates the viscous, turbulent mixing of the plume shear layer with finite-rate chemistry. Frozen and equilibrium chemistry options also exist, although the equilibrium chemistry solution has not been thoroughly tested since this is normally performed by the Shock-Capturing Component. Gas/particle interactions are calculated using the local fluid viscosity and thermal conductivity curve fits from the Processor Component.

The Turbulent Mixing Component can be run in either the constant pressure mode (which is a gas-only mode) or the overlaid mode. In general the overlaid approach couples viscous and inviscid processes in the plume near field and involves 'overlying' a parabolic plume shear layer calculation on a vector map of the near field inviscid solution. Entrainment into the shear layer from both the jet and external stream boundaries occurs through equations that describe the growth of the computational boundary. The pressure, streamwise pressure gradient and the variable edge boundary conditions (temperature and velocity) are imposed from the inviscid map arrays.

The following is the overlaying sequence of operations (schematically shown in Fig. 10).

1. The Shock-Capturing Component is used to predict the coupled inviscid/Mach disc mixing solution in the plume nearfield (i.e., ~ 2 inviscid cells). The two output files mentioned above are generated for 25 interpolated radial grid points at each axial station of the inviscid plume solutions. They contain: the gas-phase profiles of velocity flow angle, temperature, and pressure at selected axial stations, and (if appropriate) the particle profiles of velocity, enthalpy and cloud density for all size groups.
2. The Turbulent Mixing Component processes the gas-phase data and constructs vector maps used with the stream function coordinate system. It then predicts the near field plume shear layer overlaid on the vector map(s) of the inviscid near field solution. Values of velocity, temperature, and flow angle for the gas and particles are prescribed along the inner and outer boundaries.
3. At the end of the inviscid file, the Turbulent Mixing Component combines the plume shear layer and inviscid/Mach disc mixing profiles. It then solves the flowfield from the axis to the outer mixing layer boundary. The pressure variation in the subsequent transitional region is approximated by an exponential rule which decays the pressure to ambient on an individual streamline basis. When the radial pressure is constant and ambient, the flow is calculated in the constant pressure mode. Turbulent diffusion causes the particle cloud density to decrease continuously with increasing plume boundary.

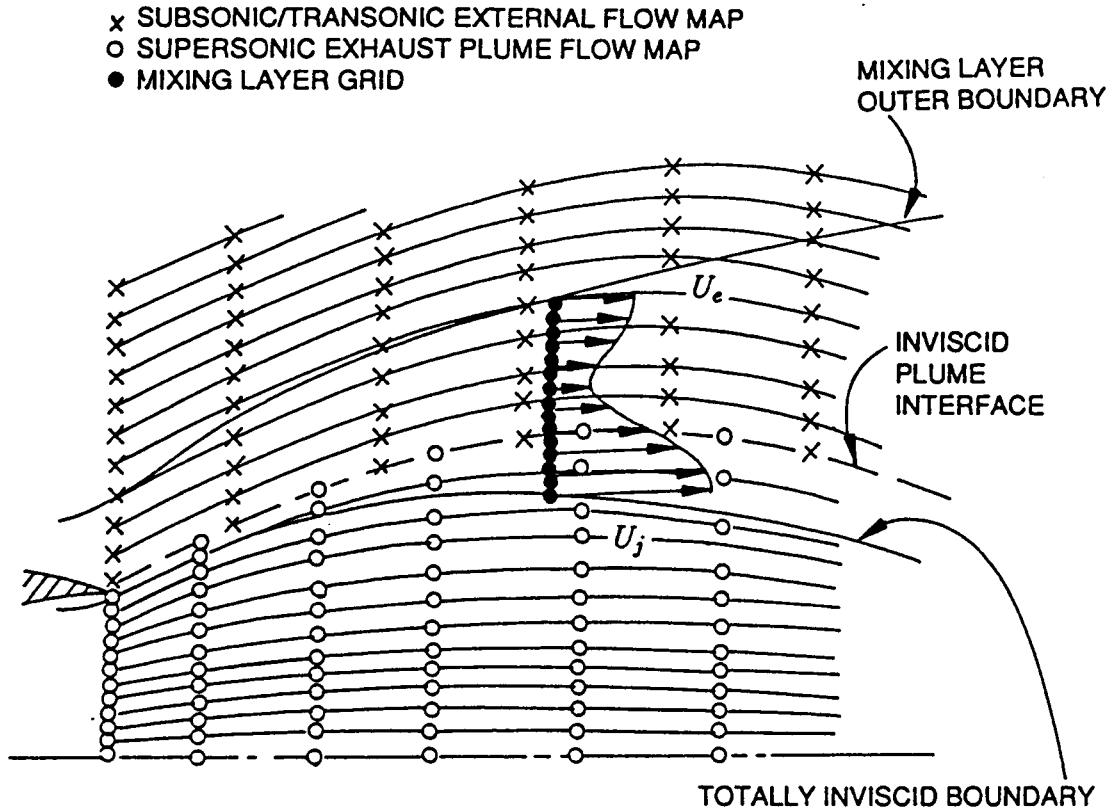


Figure 10: SPF/2 Overlaying Sequence of Operations [13]

As with the Shock-Capturing Component, the gas-phase equations are solved at the current axial station before the particle equations. The gas-phase properties are then passed to the 'stand-alone' particle integration package which solves the particle equations. The resulting gas/particle interaction terms are passed to the gas-phase equations to determine the gas properties at the next axial station. Thus the gas/particle interactions occur in a 'staggered' fashion.

Two options exist for initiating the mixing layer calculation. These are (1) a generalized option where the user specifies the initial profiles, and (2) a shear layer option. In the generalized option, the user inputs a set of values for dependent parameters. Different sets are used depending on the user-specified turbulence model. These variables are input as a function of radial distance from the axis and start at the axis or the lower edge of the shear layer. In using this option in conjunction with the overlaid procedure, the edge conditions must be consistent with the inviscid flow solutions as defined by the exhaust and external flow files. After reading the arbitrarily spaced input data, the mass flow variable is determined at all points and the data are interpolated into an equally spaced array. The same number of grid points is retained throughout the overall calculation.

In general, the user should always input the initial profiles if they are known. However, this is usually not the case; so as a default, the shear layer option has been developed. This duplicates the function properties and their first derivatives. It is used for all nonturbulence and turbulence properties everywhere in the mixing layer.

Several gas-phase two-equation turbulence models are available and used in SPF/2.

The compressibility-corrected turbulence model [14] is an extension of a previous incompressible formulation [15]. It uses a correction factor based on the characteristic Mach number of the turbulence. The model reduces to the standard model in regions of negligible compressibility. Another model is the kW model [16] with the coefficients modified by Ref. [17] to obtain consistency between rocket plume predictions and data.

Although the Prandtl mixing length turbulence model is also available in SPF/2, its use is not advised. This recommendation results from a 1979 assessment of this and other eddy viscosity models [18] which showed their performance to be erratic. None of the 'other' eddy viscosity models are available in SPF/2.

The output of SPF/2 was modified specifically to allow input to PLIMP using the methods documented in Ref. [19] and [20]. Therefore, if the user wants to use the current versions of SFP/2 he must make the same modifications. Then by specifying the correct option (see Volume II) the SPF/2 output now can be directly read and used by PLIMP. This of course aids in calculating and analyzing low altitude plume impingement.

Section 3 PLIMP PROGRAM

3.1 General Description

The original PLIMP Program [21] was introduced over 20 years ago and has experienced a number of modifications to streamline the program operation, enhance existing capabilities, and add new ones. PLIMP uses the flowfield input from one of the sources listed in Section 2.0 and user specified surfaces and options to calculate the forces, moments, pressures, heating rates, and species contamination on the surfaces. In general, the program does this by modeling the desired surfaces with six standard subshapes which are broken down into smaller elements. Local flow conditions are then obtained by locating the centroid of each element in the flowfield and using the conditions at that point. These flow conditions are assumed to act uniformly over the elemental area. The program does this for all flow regimes — continuum, transitional, and free molecular. The following sections describe the previous capabilities and the new ones.

3.2 Previous Capabilities

PLIMP has always been able to calculate forces, moments, pressures, and heating rates in the three flow regimes. It does this for the standard subshapes input by the user to model a specific spacecraft or structural part. These capabilities are documented in Refs. [21–23] and are reviewed here.

3.2.1 Surface Geometry

A series of coordinate systems is used to locate a surface with respect to the engine exhaust plume. Each surface has its own local coordinate system in which the surface local geometry parameters are specified (Fig. 11). The vector to the centroid of each element on the subshape is calculated in the engine coordinate system using the vector equation

$$\bar{R}_E = \{ [T_{R-I}] \{ \bar{R}_I \} + \bar{R}_{R-I} \} [T_{E-R}] + \bar{R}_{E-R} \quad (1)$$

where $[T]$ equals the transformation matrix from one coordinate system to another. For the Cartesian systems used in PLIMP, the matrix is the set of direction cosines that describe the positions of each axis in one system with respect to the other system's axes.

3.2.1.1 Subshapes

The six subshapes available in PLIMP are: (1) conic — cones, cylinders, etc.; (2) rectangular flat plate; (3) circular plate; (4) right triangular plate; (5) body of revolution

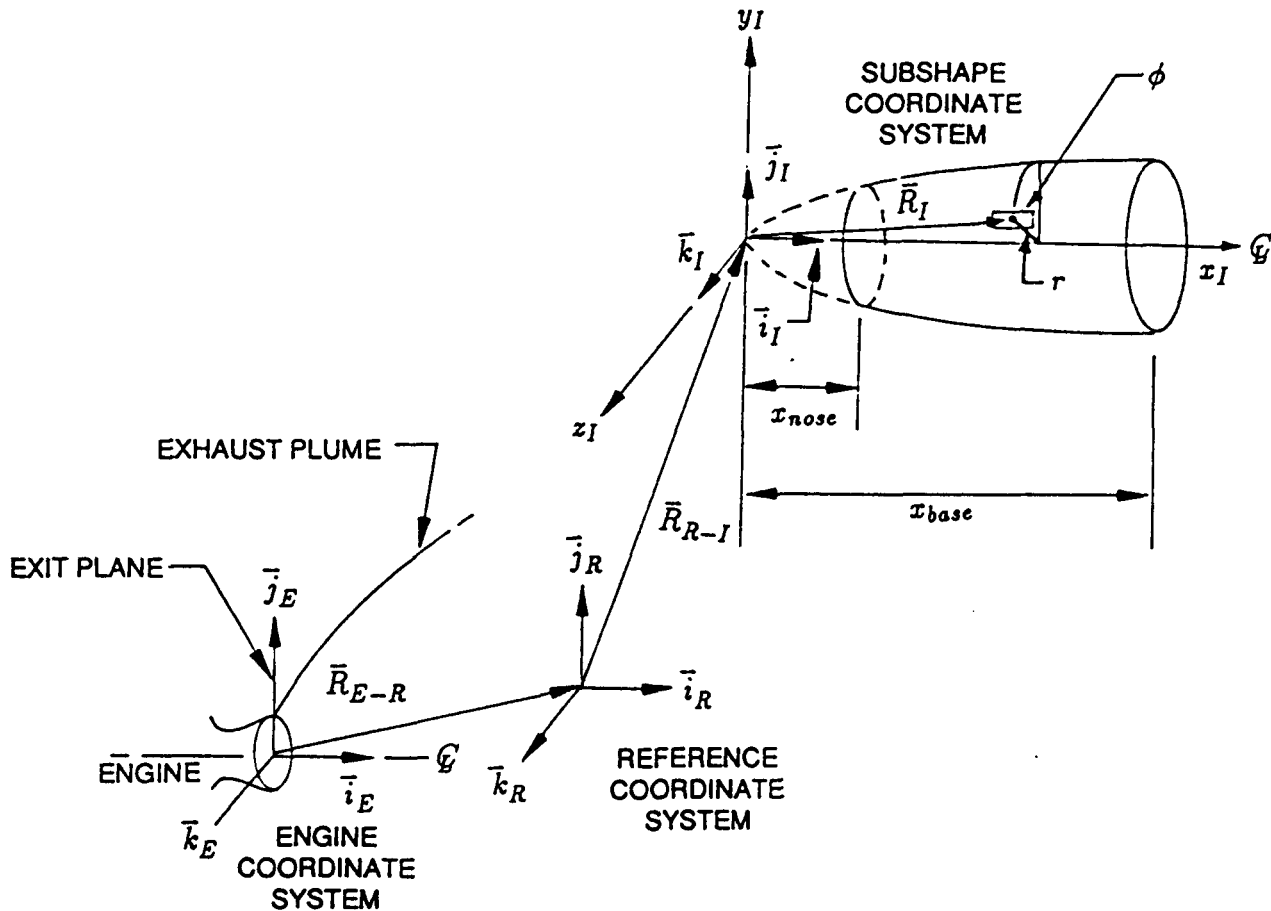


Figure 11: PLIMP Coordinate Systems [19]

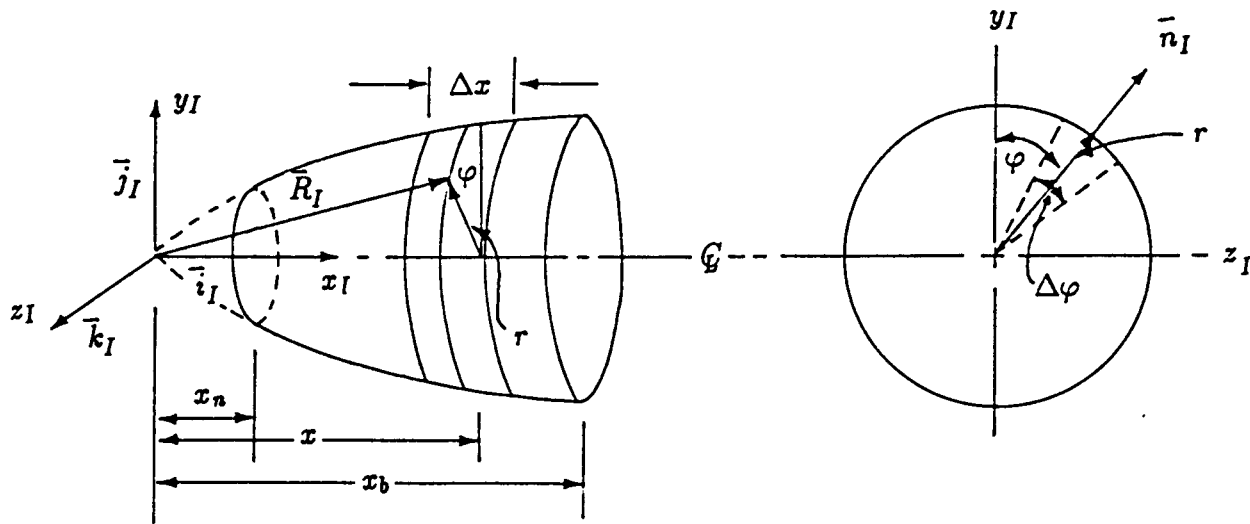
described by a polynomial; and (6) trapezoid. (Note to previous users: The airfoil or wing subshape has been eliminated.)

The position vector, \bar{R}_I , unit normal vector \bar{n}_I , and area, A , of each element in the subshape must be determined from the input parameters. The important parameters for all subshapes are shown in Fig. 12, and Table 2 summarizes the \bar{R}_I , \bar{n}_I , and A calculations.

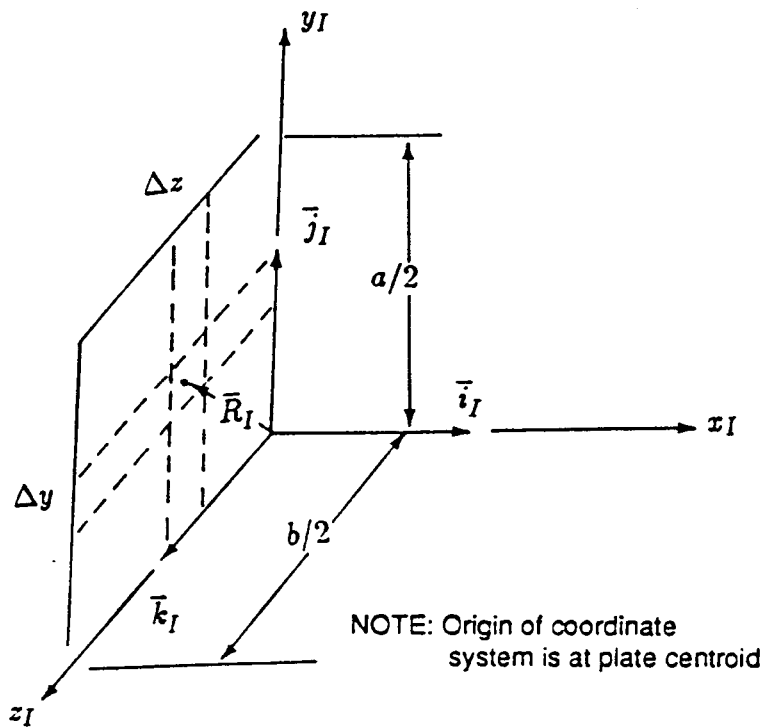
Conic — The conic subshape is one in which

$$r = a(\sqrt{b + cx + dx^2} + e) \tag{2}$$

where r is the radius, a through e are constants describing the subshape boundary, and x is the distance along the x-axis. If a and $b > 0$ and c and $d = 0$, then this is the equation for a cylinder with radius $a\sqrt{b + ae}$; if $a > 0$, b and $c = 0$, and $d > 0$, this is the equation for a cone with a $1/2$ angle = $\tan^{-1} \left(\frac{a\sqrt{dx+ae}}{x} \right)$, etc. Along with the constants a through e , the user inputs x_n for the beginning of the subshape nose and x_b for the ending of the subshape or subshape base, and ϕ_1 and ϕ_2 which begin and end the angular integration (but do not limit the surface which is always 360 deg). Also the number of elements in the axial and angular directions (N and M , respectively) are input. As a result, the following are calculated:

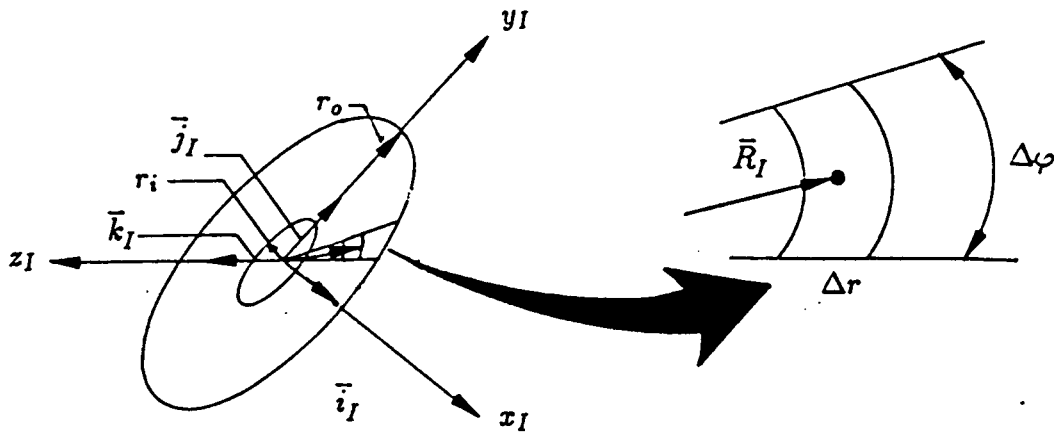


a) Conic and Body of Revolution Subshape Coordinate System and Parameters

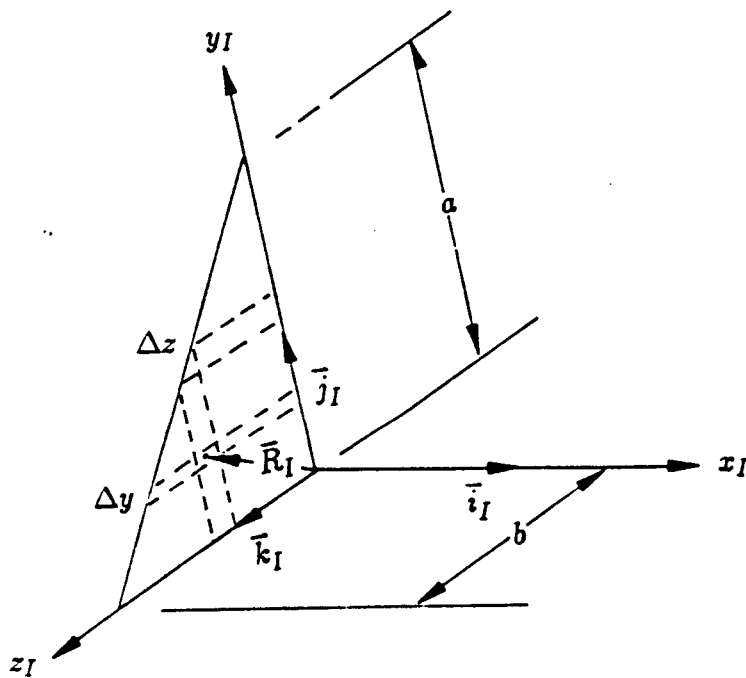


b) Rectangular Plate Subshape Coordinate System and Parameters

Figure 12: Subshape Coordinate Systems and Parameters [19]

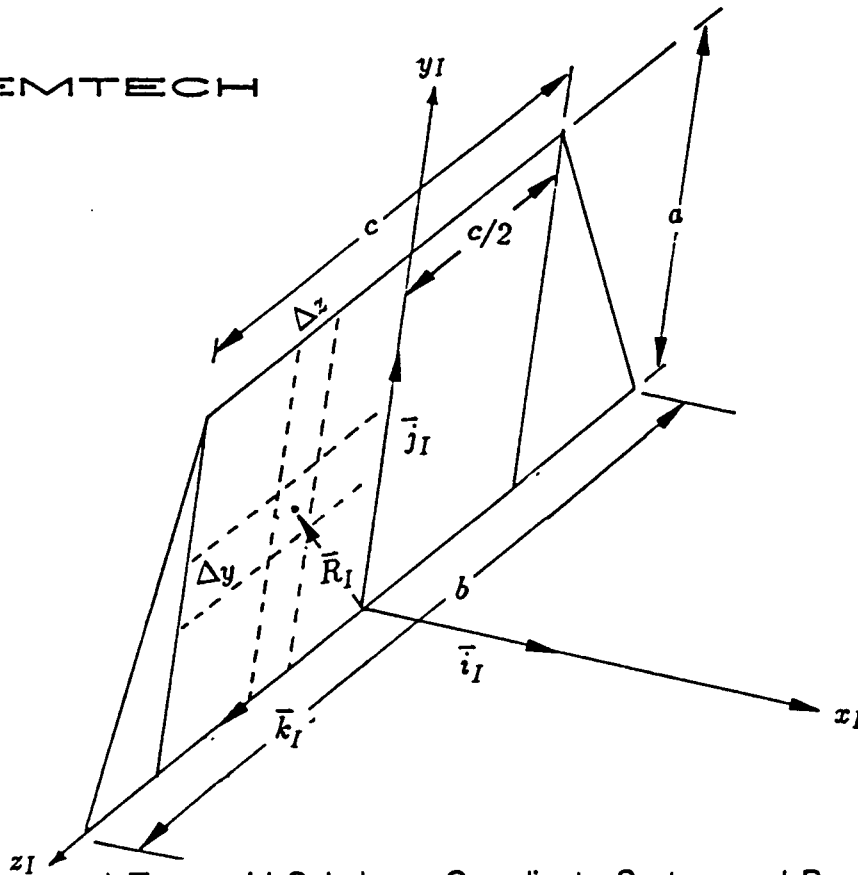


c) Circular Plate Subshape Coordinate System and Parameters



d) Triangular Plate Subshape Coordinate System and Parameters

Figure 12: (Continued) Subshape Coordinate Systems and Parameters [19]



e) Trapezoid Subshape Coordinate System and Parameters

Figure 12: (Concluded) Subshape Coordinate Systems and Parameters [19]

$$\Delta x = \frac{x_b - x_n}{N}, \quad \Delta \phi = \frac{360}{M} \tag{3}$$

$$x = x_n + \frac{\Delta x}{2}(2l - 1), \quad l = 1, N \quad \phi_m = \phi_1 + \Delta \phi(m - 1), \quad m = 1, M \tag{4}$$

Note that for the conic to correctly shade a downstream surface, e in the conic equation must be equal to zero. This is easily done for conic subshapes by simply picking the appropriate values for a and b to represent the surface instead of using e . Although e could have been dropped from the equation, it has been retained for the benefit of previous users.

Rectangular Plate — The rectangular plate subshape is two-dimensional and assumed to be in the Y-Z plane with the origin in the middle of the plate. The length and width, a and b , are input along with the number of elements in the Y and Z directions (N and M , respectively), and the following are calculated:

$$\Delta y = \frac{a}{N}, \quad \Delta z = \frac{b}{M} \tag{5}$$

Circular Plate — The circular plate subshape is similar to the rectangular plate in that it lies in the Y-Z plane. Inner and outer radii (r_i and r_o) and the number of angular and

Table 2: Important Subshape Parameters Calculated by PLIMP

Subshape	Position Vector \vec{R}_I	Surface Normal Vector \vec{n}	Elemental Area A
Conic	$x\vec{i}_I + r \cos \phi \vec{j}_I + r \sin \phi \vec{k}_I$	$\frac{-\frac{a^2}{2} \frac{(c+2dx)}{r-ae} \vec{i}_I + \cos \phi \vec{j}_I + \sin \phi \vec{k}_I}{\sqrt{\frac{a^4}{r(r-ae)^2} (c+2dx)^2 + 1}}$	$r \Delta \phi \sqrt{\Delta x^2 + \Delta r^2}$
Rectangular Plate	$y\vec{j}_I + z\vec{k}_I$	\vec{i}_I	$\Delta y \Delta z$
Circular Plate	$r \cos \phi \vec{j}_I + \sin \phi \vec{k}_I$	\vec{i}_I	$r \Delta r \Delta \phi$
Right Triangle	$y\vec{j}_I + z\vec{k}_I$	\vec{i}_I	$\Delta y \Delta z y \leq n \Delta y;$ $z \leq (N-n) \Delta z$ $n = 1, n-1$ $\frac{1}{2} \Delta y \Delta z y > (n-1) \Delta y;$ $z > (N-n) \Delta z$ $n = 1, N$
Body of Revolution	$x\vec{i}_I + r \cos \phi \vec{j}_I + r \sin \phi \vec{k}_I$	$\frac{(b+2cx+3dx^2+4er^3)\vec{i}_I + \cos \phi \vec{j}_I + \sin \phi \vec{k}_I}{\sqrt{(b+2cx+3dx^2+4er^3)^2 + 1}}$	$r \Delta \phi \sqrt{\Delta x^2 + \Delta y^2}$
Trapezoid	$y\vec{j}_I + z\vec{k}_I$	\vec{i}_I	$\Delta y \Delta z - c/2 \leq z \leq c/2$

radial elements (M and N) are input as well as an initial and final angle which control the integration (not the sector of the plate which is always 360 deg). The resulting calculations are:

$$\Delta r = \frac{(r_o - r_i)}{N}, \quad \Delta \phi = \frac{360}{M} \quad (6)$$

Triangular Plate — The triangular plate subshape is also similar to the rectangular plate and lies in the Y-Z plane. The triangle must be a right triangle. The height and base (a and b) and number of elements (M) in one direction are input by the user. (The number of elements in the other direction is automatically the same.) The resulting calculations are:

$$\Delta y = \frac{a}{M}, \quad \Delta z = \frac{b}{M} \quad (7)$$

The difference between the rectangular and triangular plate is in the triangular elements along the hypotenuse. They have half the rectangular area and their centroids are calculated using $\frac{1}{3}\Delta y$ and $\frac{1}{3}\Delta z$ instead of the $\frac{1}{2}\Delta y$ and $\frac{1}{2}\Delta z$ used for the rectangular elements.

Body of Revolution — The body of revolution is described by the polynomial equation:

$$r = a + bx + cx^2 + dx^3 + ex^4 \quad (8)$$

This is very similar to the conic equation and indeed the computed parameters are nearly the same. The user inputs $a-e$, the number of elements in the axial and angular direction (N and M), and the initial and final axial values (x_n and x_b).

Trapezoid — The trapezoid subshape is treated like the rectangular plate and the right triangle. The only difference is that the coordinate origin is at the center of the rectangle as the baseline. The right angles on either side of the rectangle have the same base and height. The user inputs the width of the base and top the height, and the number of elements in height and the base of the rectangle. The number of elements in the base of each triangle equals the height elements which is the same as discussed above for the triangular plate. Again, the calculated parameters are the same within the rectangle as the rectangular plate and in the triangle as the triangular plate.

3.2.1.2 Rotation of Axes

With $\{\bar{R}_I\}$ established for each subshape, the other elements of Equation 1 must be determined. $\{\bar{R}_{R-I}\}$ and $\{\bar{R}_{E-R}\}$ are determined by the x , y , and z inputs from the reference coordinate origin to each subshape coordinate origin and from the engine coordinate origin to the reference origin. Figure 13 shows the rotation angles used in the determination of $[T_{R-I}]$ and $[T_{E-R}]$. Both these matrices are calculated from input in which the user may specify either the rotation angles ϕ , θ , ψ , or the direction cosines for the X and Y axes. The rotation is always from the reference system, i.e., reference to the engine ($R-E$) and reference to subshape ($R-I$). The order of rotation (which is first, which is second, and which is third) is also specified by the user.

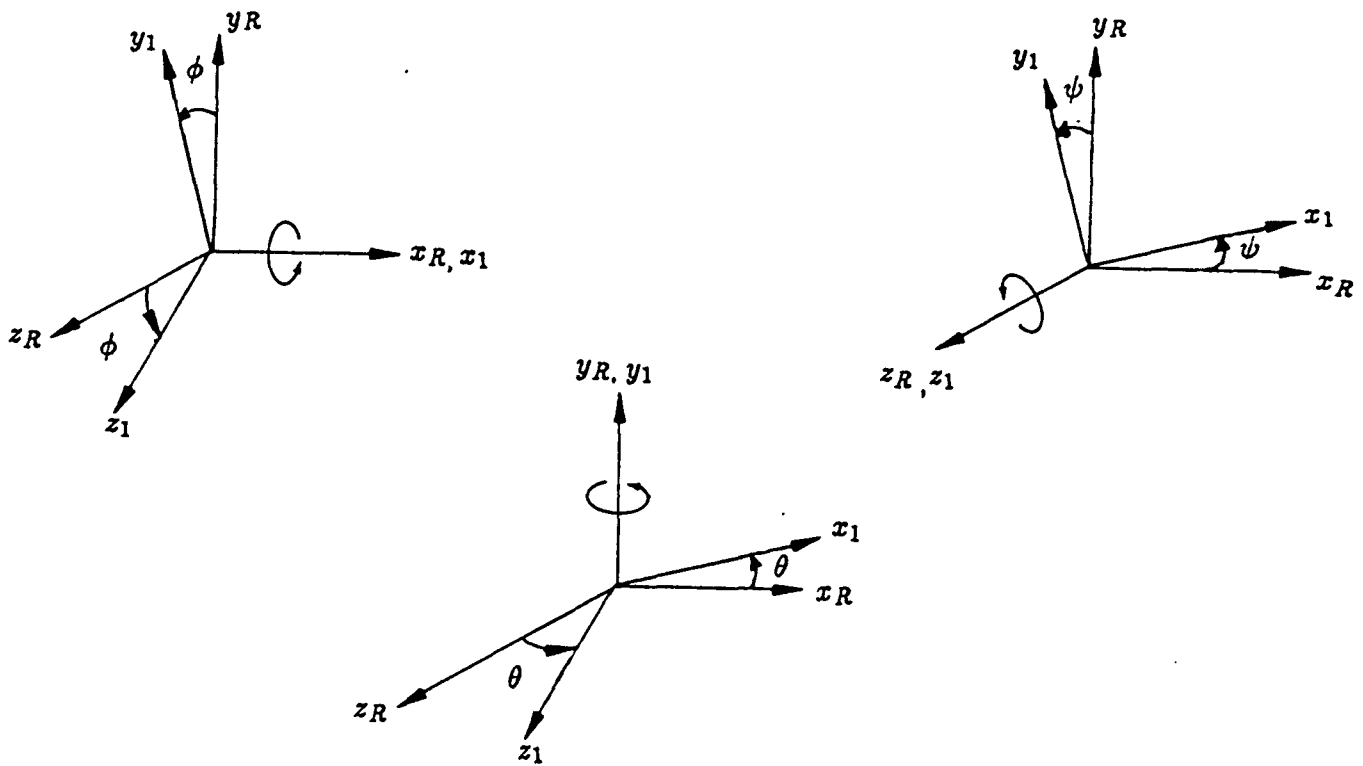


Figure 13: Rotation Angles Between Coordinate Systems

3.2.2 Impingement Properties

Once the position, \bar{R}_E , of the element is determined in the engine coordinates, the properties of the flowfield at the point are interpolated using a four-point scheme. These properties are the Mach number, M_∞ ; flow angle, θ ; entropy, S ; velocity, V ; O/F ratio and species concentration.

3.2.3 Impingement Pressure

Calculation of the impingement pressure of the flowfield on a surface depends on the density regime of the gases which can be continuous, transitional, or free molecular. The Knudsen, Kn , number ($\frac{\text{mean free path}}{\text{reference length}}$) defines the regime where:

$$\begin{aligned}
 0.00 < Kn \leq 0.01 & \quad \text{continuum} \\
 0.01 < Kn \leq 10.0 & \quad \text{transitional} \\
 10.0 < Kn < \infty & \quad \text{free molecular}
 \end{aligned}
 \tag{9}$$

The reference length is:

$$Ref = R_D \cos \alpha + R_L \sin \alpha
 \tag{10}$$

where R_D and R_L are user inputs and α is the angle between the velocity vector and the surface tangent. The mean free path is calculated by:

$$M.F.P. = \frac{2.55}{\rho_{\infty} R d} \quad (11)$$

where ρ_{∞} = local flowfield density, R = local flowfield gas constant, d = molecular diameter calculated by the method of Ref. [24]).

The free-stream conditions must be calculated to determine the impingement pressure. The equations are:

$$P_{\infty} = P_o e^{-S_{\infty}/R} \left(1 + \frac{\gamma-1}{2} M_{\infty}^2 \right)^{-\frac{\gamma}{\gamma-1}} \quad (12)$$

$$T_{\infty} = \frac{T_o}{1 + \frac{\gamma-1}{2} M_{\infty}^2} \quad (13)$$

$$\rho_{\infty} = \rho_o^* \left(1 + \frac{\gamma-1}{2} M_{\infty}^2 \right)^{-\frac{1}{\gamma-1}} \quad (14)$$

$$C_{ps} = \frac{P_s^* - P_{\infty}}{q_{\infty}} \quad (15)$$

where P_o is the total pressure before a shock, T_o is the reference temperature (usually total temperature), ρ_o^* is the density computed from the equation of state using $P_o e^{-S_{\infty}/R}$ and T_o as the reference pressure and temperature. P_s^* is the pitot pressure (post shock stagnation pressure), and q_{∞} is the post shock dynamic pressure. M_{∞} and S_{∞} are the conditions downstream of a locally normal shock parallel to the body surface and are obtained from the normal shock relations.

Continuum Flow — For continuum flow, five methods of impingement pressure calculations are available to the user — Newtonian, two modified Newtonian, isentropic expansion, and oblique shock. For the Newtonian and modified Newtonian, the impingement pressure is:

$$P_{imp} = P_{\infty} \left(1 + \frac{\gamma}{2} K_{cp} M_{\infty}^2 \sin^2 \alpha \right) \quad (16)$$

where $K_{cp} = 2$ (Newtonian), C_{ps} , or $(0.814 + \frac{6.88}{\alpha^{0.8}}) C_{ps}$ (modified Newtonian). As seen in Fig. 14, $K_{cp} = 2$ is only accurate from $\alpha = 50$ to 60 deg. The other options correct for boundary layer flow and are more accurate at different α .

In a stagnation region (e.g. nose of blunt body), the isentropic expansion method should be chosen. This method uses $K_{cp} = (0.814 + \frac{6.88}{\alpha^{0.8}}) C_{ps}$ for each element, then obtains local flow conditions by isentropically expanding from the stagnation conditions to the local impingement pressure.

For small impingement angles the oblique shock options should be chosen. The local flow properties are then calculated using attached oblique shock relations.

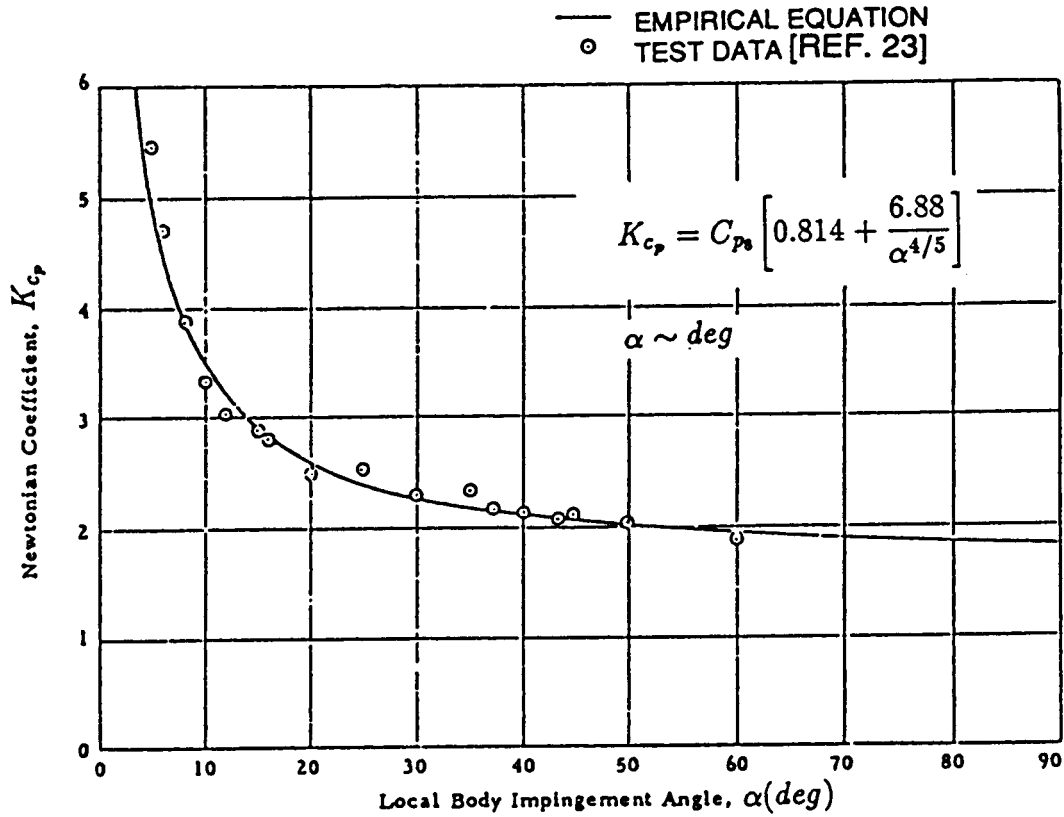


Figure 14: Empirical Fit of Newtonian Coefficient [19]

Free Molecular — Free molecular properties are handled using accommodation coefficients as defined by

$$a = \frac{E_i - E_r}{E_i - E_w} \tag{17}$$

where E_i = total incident energy transported by molecules to a unit area in unit time, E_r = total energy transported by the reflected molecules away from a unit surface area in unit time, and E_w = total energy the reflected molecules would transport away from a unit surface area in unit time if they were re-emitted at the temperature of the surface, T_w . Typical experimental values of the thermal a for surfaces and impinging molecules typical of orbital altitudes are from 0.7 to 1.0. Because of the lack of definitive values to be used in PLIMP cases, a has been set equal to one which experimental data indicate is appropriate for most orbiting spacecraft. This is applied in the force and moment determinations discussed below.

Transitional — Aerodynamic coefficients in the transitional region are combinations of those for free molecular and continuum. Experimental transition force data on spheres, cylinders and reentry vehicles were used to develop the following relationship:

$$AC_{tran} = AC_{cont} + (AC_{fm} - AC_{cont}) \sin^{-2} \left[\pi \left(\frac{1}{3} \right) + \frac{\log Kn}{\delta} \right] \tag{18}$$

where AC_{tran} = aerodynamic coefficient in transition regime
 AC_{fm} = aerodynamic coefficient in free-molecular regime
 AC_{cont} = aerodynamic coefficient in continuum regime

This equation allows a smooth transition from continuum to free-molecular coefficients of drag, pressure, etc.

3.2.4 Forces and Moments

The forces and moments acting on a subshape are shown in Fig. 15. The force acting on the subshape in the continuum regime is calculated by integrating the product of the impact pressures, elemental areas and unit normals. In finite difference form:

$$\bar{F}_I = \sum_{l=1}^N \sum_{m=1}^M (P_{imp} A \cdot \bar{n}_I)_{l,m} \tag{19}$$

For free molecular flow the following assumptions are made:

1. Molecular velocity distribution is Maxwellian.
2. Molecules reflect diffusely (accommodation coefficient, α , = 1.0).
3. Surfaces are non-concave.

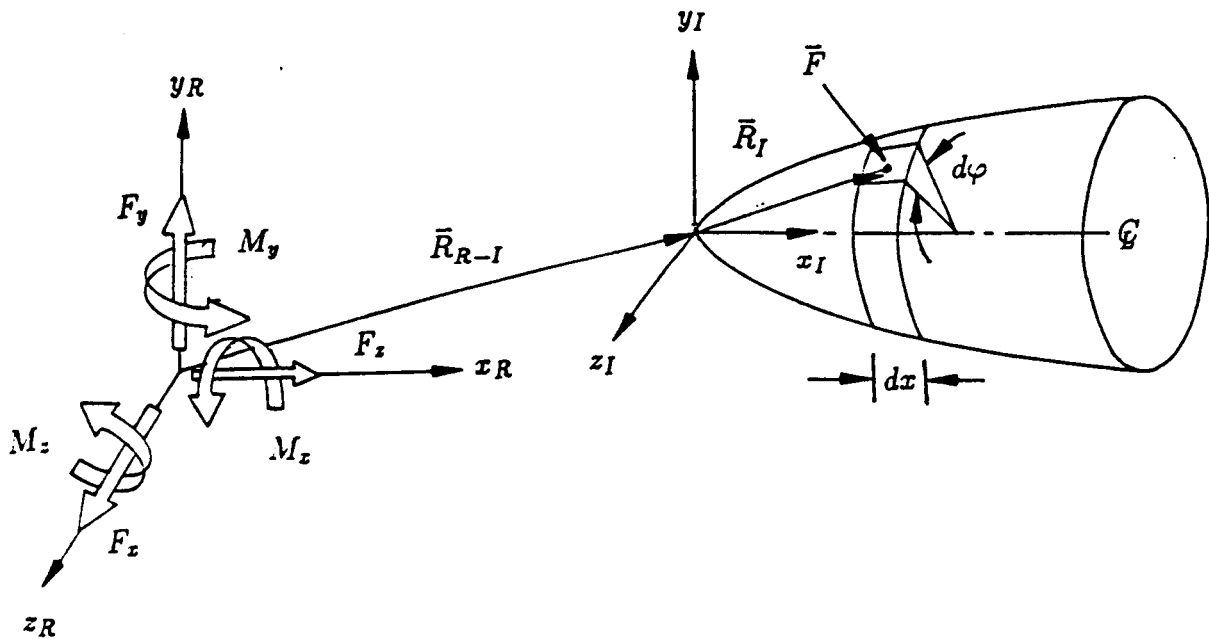


Figure 15: Force and Moment System [19]

The equation for the force on one element is

$$\bar{F} = \frac{A\zeta}{2\beta} \left\{ \frac{1}{\sqrt{\pi}} (k\epsilon + l\gamma + t\eta) \left[\gamma S^2 \sqrt{\pi} (1 + \operatorname{erf} \gamma S) + S e^{-\gamma^2 S^2} \right] + \frac{l}{2} (1 + \operatorname{erf} \gamma S) + \frac{l}{2} \sqrt{\frac{T_r}{T_i}} \left[\gamma S \sqrt{\pi} (1 + \operatorname{erf} \gamma S) + e^{-\gamma^2 S^2} \right] \right\} \quad (20)$$

where

ζ = density of molecules

$\beta = \frac{1}{2RT_i} \left(\frac{sec^2}{f_i^2} \right)$

R = gas constant

T_i = incident molecular temperature (from flowfield)

T_r = reflected molecular temperature (body temperature for a = 1.0)

S = molecular speed ratio = $\frac{\text{mass velocity}}{\text{most probable molecular velocity}}$

= $\frac{V}{\sqrt{2R_i T_i g_c}}$

k, l, t = direction cosines between local X, Y, Z axes and desired force direction

ϵ, γ, η = direction cosines between local X, Y, Z axes and mass velocity vector

$\operatorname{erf} \gamma S$ = error function of γS

The values for each element of the subshape are integrated as in the continuum calculation to determine \bar{F}_I .

The moment for each subshape in either case is calculated as the cross product of the force and displacement vectors and integrated over the subshape.

$$\bar{M}_I = \sum_{l=1}^N \sum_{m=1}^M \left(\bar{R}_I \times \bar{F} \right)_{l,m} \quad (21)$$

These equations are transformed to the reference coordinate system by

$$\bar{F}_R = [T_{R-I}] \bar{F}_I \quad (22)$$

$$\bar{M}_R = [T_{R-I}] \bar{M}_I + \left\{ \bar{R}_{R-I} \times \bar{F}_I \right\} \quad (23)$$

The resultant force and moment on the surfaces under consideration are calculated by adding the subshape force vectors and moment vectors.

The center-of-pressure location is next calculated. This varies for each subshape.

Conic — Using Fig. 16 to define the geometry of the unknown center-of-pressure point, C.P., then

$$\{\bar{C.P.}\}_I = \begin{bmatrix} \cos \omega & -\sin \omega & 0 \\ \sin \omega \cos \phi & \cos \omega \cos \phi & -\sin \phi \\ \sin \omega \sin \phi & \cos \omega \sin \phi & \cos \phi \end{bmatrix} \{\bar{C.P.}\}_\omega \quad (24)$$

where

$$\phi = \tan^{-1} \left(\frac{F_z}{F_y} \right), \quad \omega = \tan^{-1} \frac{\sqrt{F_y^2 + F_z^2}}{F_x} \quad (25)$$

and

$$\{\bar{C.P.}\}_\omega = \frac{M_z}{F_y} \bar{i}_\omega \quad (26)$$

The unit vector \bar{i}_ω is a result of rotating the subshape coordinate system ϕ degrees about the X_I -axis and ω deg about the Z_ϕ -axis. These rotations allow the simple solution of the $\{\bar{C.P.}\}_\omega$ vector, (Eq. 26), which is then rotated back into the original subshape coordinate system using θ and ω and Eq. 24.

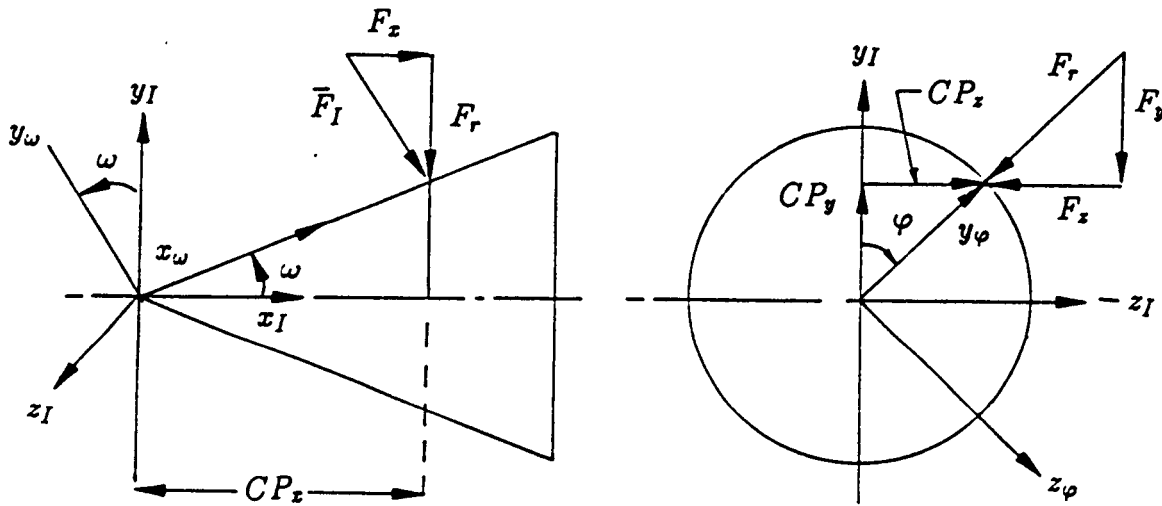


Figure 16: Conical Subshape C.P. Location

Rectangular, Right Triangular, and Trapezoidal Plate — For plates, the force vector is normal to the plane of the plate. Using Fig. 17, it can be proven that

$$\bar{C.P.}_I = -\frac{M_z}{F_x} \bar{j}_I + \frac{M_y}{F_x} \bar{k}_I \quad (27)$$

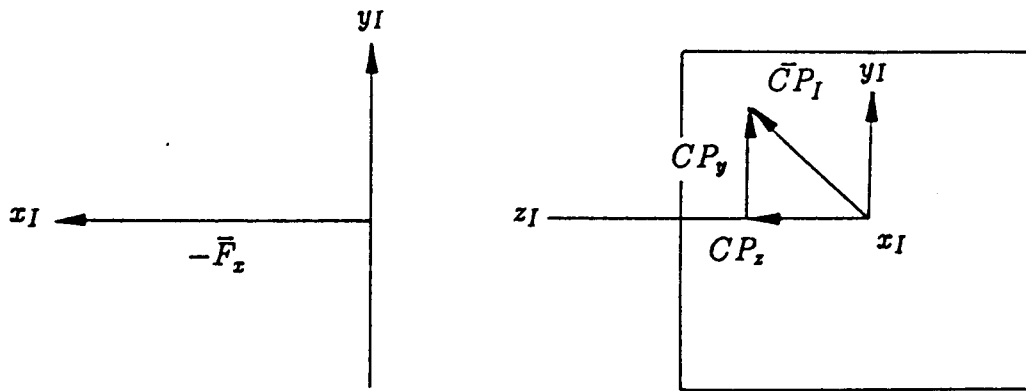


Figure 17: Rectangular, Right Triangular and Trapezoid Plate Subshape C.P. Location

Circular Plate — Figure 18 shows the geometry used in calculating C.P. for circular plates, which is similar to the rectangular and triangular plates. Expressed in the

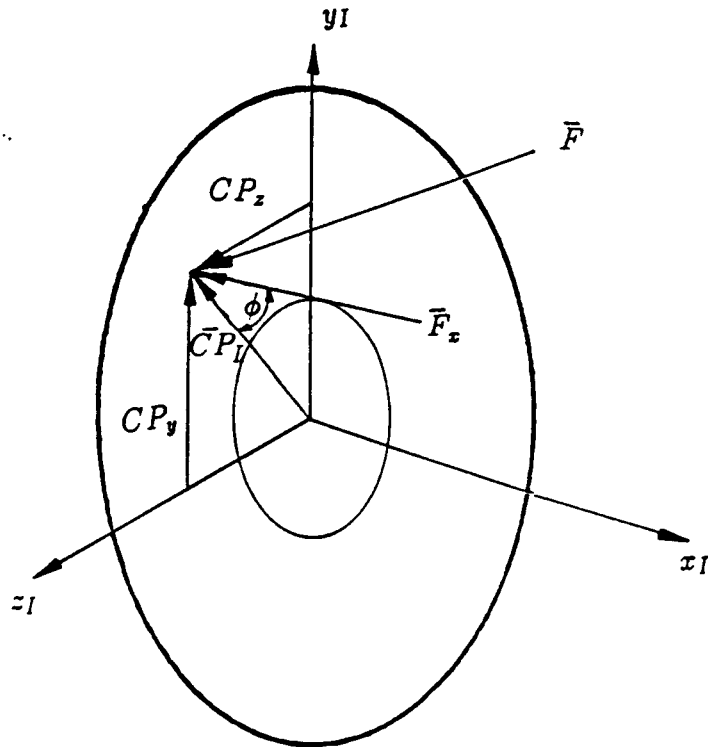


Figure 18: Circular Plate Subshape C.P. Location

cylindrical coordinates more appropriate for this subshape

$$C.P._I = \frac{M_r}{F_x} (\cos \phi \bar{j}_I + \sin \phi \bar{k}_I) \tag{28}$$

Body of Revolution — Figure 19 shows the geometry for the body of revolution which is similar to the conic. The solution is also very similar to the conic.

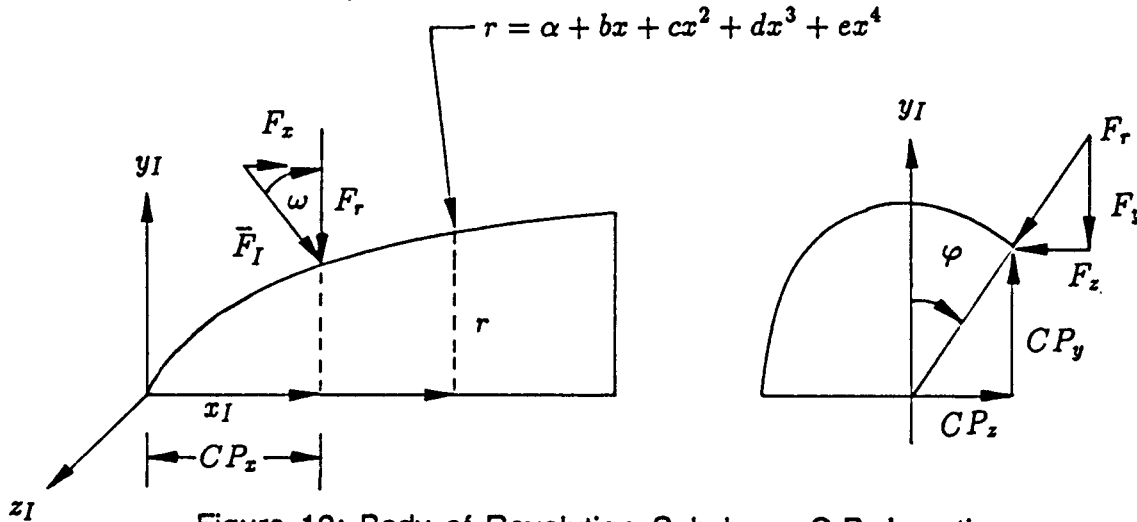


Figure 19: Body of Revolution Subshape C.P. Location

3.2.5 Heating Rates

Several methods of heat transfer analysis are available to the user since no single method adequately suffices for the variety of subshapes and flow regimes modeled by PLIMP.

Continuum — Any one of five continuum heat transfer methods may be selected by the user. The first two use the Eckert reference enthalpy method for (1) unyawed cones and (2) flat plates. For laminar boundary layers (B.L.):

$$\dot{q} = g_h(H_r - H_w) \tag{29}$$

where

$$\begin{aligned} H_r &= \text{the recovery enthalpy} \\ &= \int_0^{T_e} c_p dT + \frac{\sqrt{Pr} \cdot V_e^2}{2Jg_c} \end{aligned} \tag{30}$$

c_p = specific heat of the gas mixture, V_e = gas velocity at the edge of the B.L., T_e = temperature of B.L. edge, H_w = enthalpy of gas mixture at the surface, Pr = Prandtl number, and g_h = enthalpy conductance. The enthalpy conductance is evaluated by:

$$g_h = \frac{0.332}{Pr^{1/3}} \sqrt{\frac{\rho \cdot \mu \cdot V_e}{X_L}} \tag{31}$$

where ρ and μ = density and viscosity. The "*" indicates that these parameters are evaluated at the same temperature as the reference enthalpy H^* .

$$H^* = H_e + 0.5(H_s - H_e) + 0.22(H_r - H_e) \quad (32)$$

where the subscript, s , indicates post shock stagnation conditions. X_L is the reference length which is equal to the plate length (in the direction of flow) for a flat plate and one-third the distance from the vertex to the edge of the base for a cone. The resulting equation is, therefore:

$$\dot{q} = \frac{0.332}{Pr^{*2/3}} \sqrt{\frac{\rho^* \mu^* V_e}{X_L}} (H_r - H_w) \quad (33)$$

For a turbulent B.L. the equation is similar.

$$\dot{q} = \frac{0.0296}{Pr^{*2/3}} (\rho^* \mu^* V_e)^{0.8} \left(\frac{\mu^*}{X_T}\right)^{0.2} (H_r - H_w) \quad (34)$$

and $X_T = X_L$ for a flat plate or 4/9 the distance from the vertex to the edge of the base for a cone. H_r for turbulent calculations is similar to Eq. 30:

$$H_r = \int_0^{T_s} c_p dT + \frac{(Pr^*)^{1/3} V_e^2}{2Jg_c} \quad (35)$$

The next two methods of heat transfer available to the user deal with (1) yawed cones and (2) cylinders and wings. For laminar B.L. stagnation line heating an empirical correlation is used.

$$\dot{q}_s = \frac{0.565}{Pr_w^{2/3}} \sqrt{\rho_w \mu_w \frac{dV}{dR}} \left(\frac{\rho_e \mu_e}{\rho_w \mu_w}\right)^{0.44} (H_r - H_w) \quad (36)$$

where

$$\frac{dV}{dR} = \frac{2V_\infty \sin \alpha}{R} \left[1 - 0.416 (M_\infty \sin \alpha)^2 - 0.164 (M_\infty \sin \alpha)^4\right] \quad (\text{subsonic}) \quad (37)$$

$$= \frac{1}{R} \sqrt{2g_c \left(\frac{P_s - P_\infty}{\rho_s}\right)} \quad (\text{supersonic}) \quad (38)$$

α = angle between V_∞ and shock parallel to the body, and R = cylinder radius.

For turbulent B. L., the swept cylinder theory of Beckwith and Gallagher is applied. This results in the equation:

$$\dot{q}_s = \frac{0.0288}{Pr_w} \left(\frac{V_\infty \cos \alpha}{\mu_s}\right)^{0.6} \left(\frac{dV}{dR}\right)^{0.2} (\rho_w \mu_w)^{0.8} (H_r - H_w) \quad (39)$$

where the parameters have the same definition as the laminar case, except H_r which uses the turbulent recover factor, $(Pr^*)^{1/3}$.

For unyawed cylinders and cones in non-stagnation regions, PLIMP computes the stagnation heat transfer rate and uses a ratio to compute the heating rates for other regions. For laminar flow, the equation is based on work performed by Marvin.

$$\frac{\dot{q}}{\dot{q}_s} = \left(\frac{P}{P_s} \right)^{0.85} \quad (40)$$

This is also useful for hemispherical forebodies and yawed cylinders. For turbulent flow the equation is:

$$\frac{\dot{q}}{\dot{q}_s} = \left(\frac{P}{P_s} \right)^{\frac{3\gamma-1}{2\gamma}} \left[\frac{\left(\frac{P}{P_s} \right)^{\frac{\gamma-1}{\gamma}} - \frac{T}{T_o}}{1 - \frac{T}{T_o}} \right]^{0.375} \quad (41)$$

The final heat transfer option concerns stagnation heating rates in an arbitrary flowfield. An empirical equation developed by Marvin and Deiwert is used:

$$\dot{q}_s = \frac{0.324}{Pr_w} \sqrt{2^n (\rho\mu)_w \left(\frac{dV}{dR} \right)} \left(\frac{1 - \frac{(\rho\mu)_D}{(\rho\mu)_w}}{\frac{H_D - H_w}{H_s}} \right)^{-0.15} (H_s - H_w) \quad (42)$$

where $n = 1$ or 0 (axisymmetric or two-dimensional), $\frac{dV}{dR}$ is evaluated for supersonic flow (Eq. 38), and subscript, D , is dissociation properties defined as the point at which the molecular weight deviates one percent from the wall value. (The dissociation properties are calculated by the TRAN72 program discussed above in Section 2.)

The above calculations depend heavily on the heat transport properties of μ , k (thermal conductivity), and c_p . Accordingly, μ for a pure gas is calculated from the collision integral model:

$$\mu = \frac{2.6693 \times 10^{-6} \sqrt{Mwt T(^{\circ}K)}}{\sigma^2 \Omega^{(2,2)*} T^*} \quad (43)$$

where Mwt is molecular weight, σ is the intermolecular force constant and $\Omega^{(2,2)*}$ is the collision integral. (These latter two quantities have been tabularized for approximately 200 gas species and are available within PLIMP.) Using the Lennard-Jones potential:

$$k = R_M \mu \left(0.45 + 1.32 \frac{c_p}{R_M} \right) \quad (44)$$

The specific heat is evaluated as a fourth order curve fit:

$$c_p = R_M (a + bT + cT^2 + dT^3 + eT^4) \quad (45)$$

where the constants are available within PLIMP.

For gas mixtures a weighted averaging method is used to determine the mixture molecular weight, Mwt , and c_p for m constituents:

$$Mwt = \sum_{i=1}^m (\text{mole fraction})_i Mwt_i \tag{46}$$

$$c_p = \sum_{i=1}^m c_{pi} Mwt_i \tag{47}$$

The method of Wilke is used to calculate the mixture values of μ and k .

$$\mu = \sum_{i=1}^m \mu_i \left\{ 1 + \sum_{\substack{j=1 \\ j \neq i}}^m \frac{\left[1 + \sqrt{\frac{\mu_i}{\mu_j}} \left(\frac{Mwt_j}{Mwt_i} \right)^{\frac{1}{4}} \right]^2}{2\sqrt{2} \sqrt{1 + \frac{Mwt_i}{Mwt_j}}} \frac{(\text{mole fraction})_j}{(\text{mole fraction})_i} \right\}^{-1} \tag{48}$$

$$k = \sum_{i=1}^m k_i \left\{ 1 + 1.0165 \sum_{\substack{j=1 \\ j \neq i}}^m \frac{\left[1 + \sqrt{\frac{k_i}{k_j}} \left(\frac{Mwt_j}{Mwt_i} \right)^{\frac{1}{4}} \right]^2}{2\sqrt{2} \sqrt{1 + \frac{Mwt_i}{Mwt_j}}} \frac{(\text{mole fraction})_j}{(\text{mole fraction})_i} \right\}^{-1} \tag{49}$$

Transition — The Maslen solution is used to determine heating rates on flat plates in the low density, transition flow regime. Maslen adds a correction term to the continuum laminar B.L. solution (Eq. 33).

$$\dot{q} = \frac{0.332}{Pr^{*2/3}} \sqrt{\frac{\rho^* \mu^* V_e}{X_L}} (H_r - H_w) - \frac{0.13816}{Jg_c} \sqrt{\frac{\gamma T_w}{T^*}} \frac{\mu_w^2}{\mu^*} \frac{M_e V_e^2}{X_L} \tag{50}$$

Free Molecular — The assumptions used to compute the impingement pressure in free molecular flow are also used in the heating rate determination. That is Maxwellian velocity distribution for impacting molecules and the use of accommodation coefficients. Essentially the heating rate is equal to the difference in the incident and reflected energies. When the internal energy is accounted for by subtracting the translational energy from the total internal energy and assuming the gas is in thermal equilibrium the

final equation is:

$$\begin{aligned} \frac{\dot{q}}{a} = & \frac{\rho_i R_i T_i}{J} \sqrt{\frac{R_i T_i g_c}{2\pi}} \left\{ e^{-S^2 \sin^2 \theta} \left[2 \left(1 - \frac{T_w}{T_i} \right) + S^2 \right] \right. \\ & \left. + \sqrt{\pi} S \sin \theta (1 + \operatorname{erf} S \sin \theta) \left(S^2 + 2.5 - \frac{2T_w}{T_i} \right) \right\} \\ & + \rho_i \sqrt{\frac{R_i T_i g_c}{2\pi}} \left[H_i - \frac{R_i T_i}{2J} - \frac{R_i}{R_w} \left(H_w - \frac{R_w T_w}{2J} \right) \right] \\ & \left[e^{-S^2 \sin^2 \theta} + \sqrt{\pi} S \sin \theta (1 + \operatorname{erf} S \sin \theta) \right] \end{aligned} \quad (51)$$

where a is the accommodation coefficient (1.0 for PLIMP), θ is the angle between the velocity and the surface, and S is the molecular speed ratio $\left(\frac{V}{\sqrt{2R_i T_i g_c}} \right)$. This heating rate was developed for the forward face only. For the backside the equation is almost the same but several signs are now negative.

$$\begin{aligned} \frac{\dot{q}}{a} = & \frac{\rho_i R_i T_i}{J} \sqrt{\frac{R_i T_i g_c}{2\pi}} \left\{ e^{-S^2 \sin^2 \theta} \left[2 \left(1 - \frac{T_w}{T_i} \right) + S^2 \right] \right. \\ & \left. - \sqrt{\pi} S \sin \theta (1 - \operatorname{erf} S \sin \theta) \left(S^2 + 2.5 - \frac{2T_w}{T_i} \right) \right\} \\ & + \rho_i \sqrt{\frac{R_i T_i g_c}{2\pi}} \left[H_i - \frac{R_i T_i}{2J} - \frac{R_i}{R_w} \left(H_w - \frac{R_w T_w}{2J} \right) \right] \\ & \left[e^{-S^2 \sin^2 \theta} - \sqrt{\pi} S \sin \theta (1 - \operatorname{erf} S \sin \theta) \right] \end{aligned} \quad (52)$$

3.2.6 Shading

Elemental shading occurs in two ways: (1) the element may be facing away from the flow, or (2) the element may be behind another subshape. In the first case the element is unshaded if the dot product of the velocity and unit normal is less than zero (Fig. 20).

$$\vec{V}_I \cdot \vec{n}_I < 0 \quad (53)$$

where

$$\{ \vec{V}_I \} = [T_{R-I}] \{ [T_{E-R}] \{ \vec{V}_E \} \}_E$$

If this test is positive, no further calculations are performed. Otherwise the shading is calculated as follows (see Fig. 21). A position vector is calculated

$$\vec{R}' = [T_{I'-R}] \left\{ \vec{R}_{R-I} + [T_{R-I}] \{ \vec{R}_I \} - \vec{R}_{R-I} + \lambda [T_{R-E}] \{ \vec{V}_E \} \right\} \quad (54)$$

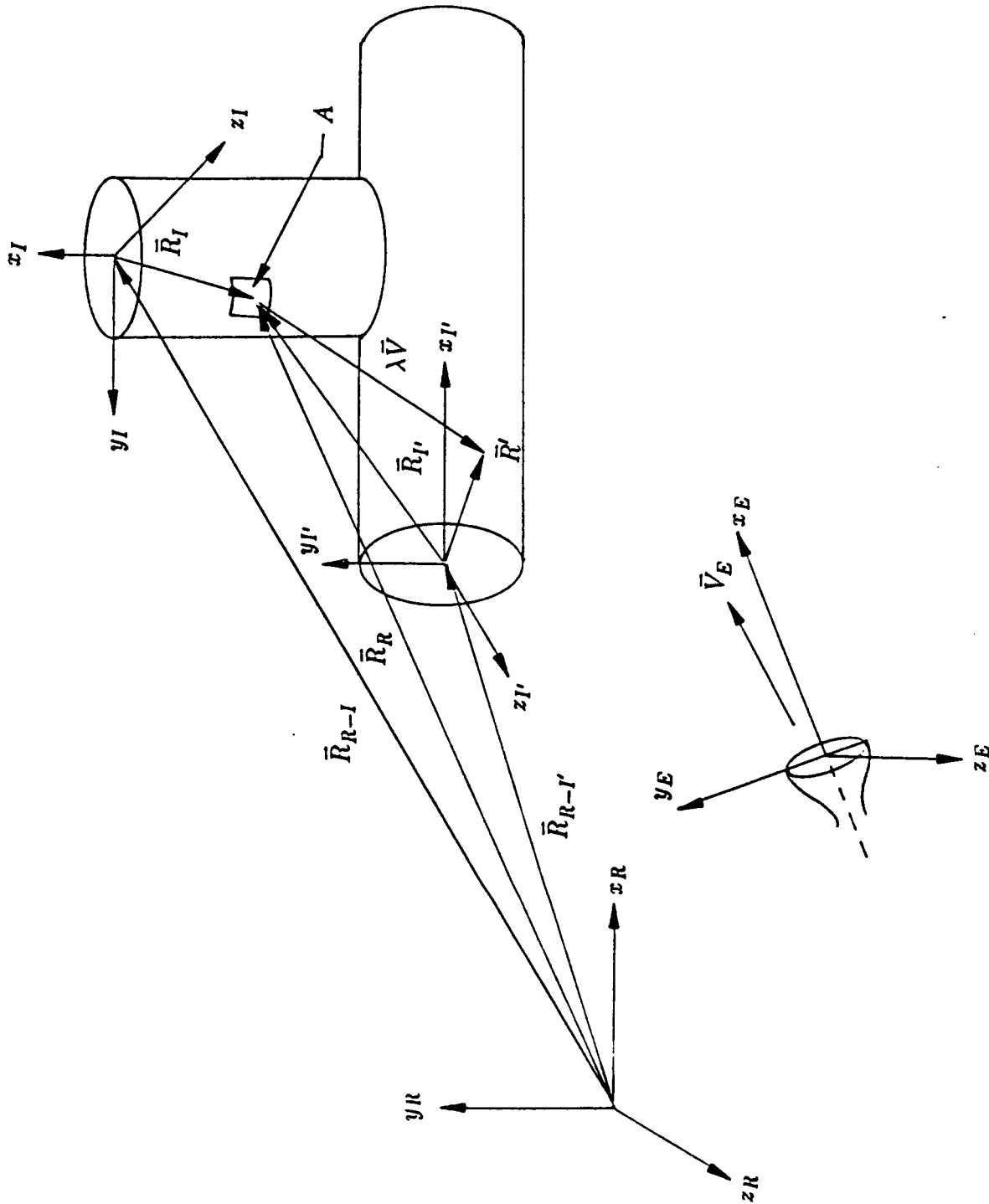


Figure 21: Vectors for Determining Shading of One Subshape by Another

Flat Plate — For the flat plates, λ can be simply calculated because $x_{I'} = 0$ and $R_{x'} + \lambda V_{x'} = x_{I'} = 0$. Therefore;

$$\lambda = \frac{-R_{x'}}{V_{x'}} \tag{59}$$

Again, if λ is real and positive or $V_{x'}$ is zero, no shading occurs. However, if λ is negative, shading occurs if:

Rectangular Plate:

$$-\frac{a}{2} < R_{y'} + \lambda V_{y'} < \frac{a}{2} \text{ and } -\frac{b}{2} < R_{z'} + \lambda V_{z'} < \frac{b}{2} \tag{60}$$

Circular Plate:

$$r_i < \sqrt{(R_{y'} + \lambda V_{y'})^2 + (R_{z'} + \lambda V_{z'})^2} < r_0 \tag{61}$$

Right Triangular Plate:

$$0 < R_{y'} + \lambda V_{y'}, 0 < R_{z'} + \lambda V_{z'}, \tag{62}$$

and

$$\frac{b}{a}(R_{y'} + \lambda V_{y'}) + R_{z'} + \lambda V_{z'} < b \tag{63}$$

Trapezoid:

$$0 < R_{y'} + \lambda V_{y'} < a, R_{z'} + \lambda V_{z'} - \frac{b-c}{2a}(R_{y'} + \lambda V_{y'}) > -\frac{b}{2}, \tag{64}$$

and

$$R_{z'} + \lambda V_{z'} + \frac{b-c}{2a}(R_{y'} + \lambda V_{y'}) < \frac{b}{2} \tag{65}$$

Body of Revolution— The body of revolution shading is solved in a manner similar to the conic except that the equation for λ becomes a very difficult expression:

$$r^2 = y^2 + z^2 = (a + bx + cx^2 + dx^3 + ex^4)^2 \tag{66}$$

where

$$\begin{aligned} x &= R_{x'} + \lambda V_{x'} \\ y &= R_{y'} + \lambda V_{y'} \\ z &= R_{z'} + \lambda V_{z'} \end{aligned}$$

Bairstow's method [26] is used to solve this eighth order polynomial. This is an iterative method which involves guessing u and v and finding quadratic factors of the polynomial, $f(x) = x^2 + ux + v$. Upon obtaining these two roots, the process is repeated on the polynomial resulting from the extraction of prior quadratic factors until all the roots of the original polynomial are found. Then, new approximations for u and v are made, and the process is repeated for convergence on u and v . This results in real and imaginary roots which are evaluated for shading using the criteria for a conic.

3.3 Changes and Added Capabilities

A number of changes have been made to PLIMP to improve the speed, accuracy, computer compatibility, and abilities. Many of these changes are not necessarily apparent to a user as they do not affect input or output. However, all changes have improved impingement analyses performed using PLIMP.

3.3.1 Internal Improvements

PLIMP coding has been updated to FORTRAN 77 which makes it compatible with most compilers. It has also had a number of changes to eliminate redundancies and improve speed and accuracy. It has further been compiled and linked on a UNIX-based computer which makes it compatible with most users' computers.

Several modifications have been made to improve PLIMP's input and output. It is now possible to specify SI units. The program still makes all its calculations in English units since SI values are converted to English and output values are reconverted to SI before being stored.

The printed output has also been changed. Previously, 132 columns were used which made reproduction on $8\frac{1}{2}$ x 11 inch paper difficult. The current output is 80 columns wide.

To aid the user, a number of input parameters have been given default values. They are based on the most common values typically used in impingement analysis. These parameters and values are discussed in Volume II.

Two changes were made to increase the versatility of the geometry subroutines. First, the total number of subshapes has been increased from 10 to 50 to allow complex structures such as the Space Station central beam to be modeled. Second, the centroids of adjacent subshapes are automatically aligned so that easy comparison of parameters on adjacent surfaces can be made.

3.3.2 Particle Impingement

The original PLIMP code could perform particle impingement force and heating rate calculations for two-phase RAMP2 plumes. However, separate executions of the PLIMP code were required to handle both gaseous and particulate calculations. RAMP2 has now been modified to pass both the particle and gas property data to the PLIMP code in a single run. Also, PLIMP's particle impingement option has been made fully operational for calculating particle contributions to forces and moments (pressures and heating rates were previously operational), thus allowing two-phase impingement cases to be analyzed in a single execution. This modification, documented in Ref. [19], greatly reduces the amount of computer time and postprocessing of the data which were previously required when two executions were necessary.

The particle impingement model uses a simplified method for calculating particle effects to the surface. More explicitly, it uses a user input accommodation coefficient similar to the base molecular gaseous one discussed in Section 3.2.3 to determine the percentage of particle momentum and energy actually transferred to the surface.

The accommodation coefficient, which is determined experimentally, accounts for the interaction of the particles in the shock layer and at the surface. It can vary over a significant range depending on the aluminum oxide loading (mass flux) and the shock layer ahead of the body. For calculations where the experimental value is unknown, a value of 0.5 is suggested for conservative results.

PLIMP now calculates the forces and moments for particulates and summarizes the particulate impingement environments, in addition to the gaseous environments, in its output. A summary of the particle contributions to forces and moments has also been added.

Simple PLIMP cases have been compared with hand calculations for a flat plate inserted at the point in a RAMP2 plume where the particle properties are known from the RAMP2 results. The force and moment calculations produce reasonable values.

3.3.3 SFPGEN

Calculating rocket exhaust plume flowfields to very large distances in near-vacuum conditions is very time consuming using the methods of Section 2. It is also a lengthy process to use these flowfields in PLIMP because of the numerous interpolations necessary to order the flowfields for use in impingement calculations. As a result a source flow plume generator program, SFPGEN [27], has been coded to produce very long, PLIMP-compatible exhaust plumes from RAMP2 calculations.

RAMP2 is run to the length desired but at least to the point where the streamlines no longer change slope (e.g., 80–100 exit radii for Space Station altitudes). SFPGEN is run with the RAMP2 flowfield as input and it outputs the local total enthalpy, velocity, and density at up to 50 centerline locations. It also calculates the local-to-centerline ratios of density, velocity, and temperature for 25 angular increments at each centerline location. The centerline locations begin 1.5 exit radii from the exit and use a cosine distribution so that more near field locations are generated for increased accuracy in this area. The maximum flow angle is taken from the RAMP2 input. To increase accuracy in high flow angle areas where boundary layer effects are significant, an additional flow angle increment is added at each centerline location.

The major advantages of using SFPGEN for PLIMP are:

1. The flowfield is portable from computer to computer because it is written as an ASCII formatted file instead of a binary file like RAMP2.
2. The flowfield requires considerably less storage than RAMP2. For example, 0.06 megabytes instead of 4–5 megabytes for a typical plume.
3. The PLIMP calculations are much faster than using RAMP2 input.
4. The plume flowfield can be calculated much further from the exit than is practical with RAMP2.

It should be noted, however, that the mach numbers may get very large and the temperature very low due to continuum flow assumption of the source flow model. However, at large distances from the exit plane the impingement will probably be free molecular. For free molecular impingement density and velocity are the important

variables. The source flow model does an excellent job of modeling the density and velocity so it should result in good predictions for free molecular pressure and heating rates at large distances.

3.3.4 Contamination Determination

A major improvement to the PLIMP Program has been the addition of a tool to estimate the types and amounts of contamination on a surface due to flow impingement. The complete documentation of this model is Ref. [28], but basically the model's premise is that a net deposition occurs when the arrival rate of a given species is greater than the evaporation rate.

Table 3 lists all the species for which PLIMP has stored thermodynamic data. The asterisks indicate that vapor pressure data is incorporated as a table of partial pressure versus temperature at the critical pressure. Therefore for a given surface temperature if the partial pressure is higher than critical, condensation occurs. Species without an asterisk have no stored data and are assumed to deposit regardless of the surface temperature. If a species exists on the flowfield tape and is not in Table 3, it is not considered for deposition.

Evaporation rate data for HCl, CO₂, NH₃, H₂O, N₂H₄ have been incorporated into PLIMP as well; however, the lack of data for other species has required the conservative assumption that they do not evaporate. Other special considerations have also been accounted for: (1) all species deposit below 40°K with no evaporation, (2) the N₂H₄ mole fraction is assumed 0.05 for cold starts and 0.004 for pulsed operation, (3) a 0.2 mass fraction for MMN nitrate deposits at all temperatures, (4) all hydrazine evaporates above 180°K — no deposition, and (5) if more than 25 species are present in the flowfield, PLIMP selects only the 25 most dominate species for analysis.

To perform the contamination calculation the temperature of each subshape must now be input. PLIMP will calculate pressure as described in Section 2 and make the deposition determination in accordance with the above guidelines. The output can be the incident species mass flux only or the incident flux and net deposition. A conservative approach would be to use the incident flux for design purposes and the net deposition for prediction.

3.3.5 Graphics

3.3.5.1 Introduction

A graphics ability has been developed using the NCAR graphics package to display PLIMP subshapes and results. This program has enhanced NCAR's capabilities and permits the user to view the subshapes and surfaces before running PLIMP so that adjustments may be made. Using a straight line-of-sight method the program predicts possible shading as well. In postprocessing the PLIMP output is used to show the subshapes and surfaces with color contours representing surface conditions such as temperature, heat rate, pressure, etc.

Table 3: Species Contained in PLIMP Data File

*Al	*CF ₄	*H ₂ S	Na ₂
AlCl	CH	He	*Ne
AlClH ₃	ICH ₄	I	O
AlF	CN	*I ₂	OH
AlF ₃	*CO	*Li	O ₂
AlN	*COS	*LiCl	P
AlO	*CO ₂ **	*LiF	PCl ₃
*Ar	CP	LiO	PF
B	CS	*Li ₂	PH ₃
BCl	C ₂	Li ₃ O	PN
BCl ₂	*C ₂ H ₂	*Mg	PO
*BCl ₃	*C ₂ H ₄	MgCl	PS
BF	*C ₂ N ₂	*MgCl ₂	P ₂
BF ₂	Cl	MgF	P ₄
*BF ₃	ClCN	MgF ₂	*S
BO	*ClF	N	*SF ₆
B ₂	*ClF ₃	*N ₂	SO
B ₂ O ₃	*ClO	NF ₃	*SO ₂
Be	*Cl ₂	NH	S ₂
BeCl	*F	*NH ₃ **	*Si
*BeCl ₂	FCN	*NO	SiCl
BeF	*F ₂	*NOCl	SiCl ₄
BeF ₂	H	*N ₂ O	SiF
*C	*HCN**	*Na	SiF ₄
CCl	*HCl**	*NaCl	SiH ₄
CF	HF	*NaF	SiO
CF ₂	*H ₂	NaO	*SO ₂
CF ₃	*H ₂ O**	*NaOH	SiS
			Sl ₂
			*UA (unreacting ammonia)

*Vapor Pressure Data Available

**Evaporation Rate Data Available

The software developed assumes the subshape to be composed of three or four-sided elements, each read by the program and depth sorted according to the projection of its centroid onto an axis perpendicular to the screen – the eye Z-vector. Once sorted, the elements are projected onto the eye vector's X-Y plane for screen drawing. The color contours are determined by varying the hue as a function of the intensity of the surface condition displayed. Each individual element is assigned a color; no interpolation is performed; therefore, more elements yield a better graphical representation. Eye vectors are "hard-wired" into the program, although different or additional eye vectors can be substituted or added. NCAR uses frames to store the various view angles of the surfaces as well as the views of the individual subshapes composing the surface. The user only has to click a mouse to view the previous or following frame.

The burden of details concerning input and execution of the pre- and postprocessing software has been made transparent to the user. PLIMP output has been modified to be directly read into the postprocessing subroutines that generate vertices, depth sort, and draw to the screen. The user types only ONE command to execute the entire graphics package.

The overall graphics package developed can be discussed as two separate but coupled parts: a graphical preprocessor for viewing PLIMP input surface data before actual PLIMP solutions are executed and a graphical post processor to view surface contours resulting from the solution. The preprocessor requires the user to input only minimal data such as subshape type, overall dimensions and spatial relationships with the reference coordinate system. Once this data is input, full three-dimensional pictures, including line of sight shading (if requested), are available for the user to view. This feature is seen as a way to avert many "trash-runs" that result because of geometry or other input errors. The preprocessor can be run as a part of PLIMP (see Volume II User's Input Guide Section 2.1) or separately as discussed below in "Preprocessing."

The various graphics routines developed and their logical association and flow are illustrated in Fig. 22. The overall control of the individual subroutines and data files has been divided between a main FORTRAN routine and a UNIX bourne shell script. Initially, it is assumed that the user enters the graphics package with one or more of the following PLIMP output data files: `plimp-graphics.dat`, `picture.dat`, and `plimp-graphics.cgm`. The software interface questions the user to determine which file the user wants to dictate execution path flow. More than one of the above files may exist, however, only one can be acted upon by the graphics package at any single execution of the graphics software. Each data file and algorithm depicted by a box in Fig. 22 is discussed in detail below.

3.3.5.2 Subshape Drawing

Vertex Calculations — Initially the vertices for the elemental areas associated with the centroids input from the PLIMP data are calculated. Vertex calculations are performed for each centroid by assuming a flat plane element and using the PLIMP data for the subshape type and dimensions. Once vertices are calculated they are passed to the rotational matrix transformation:

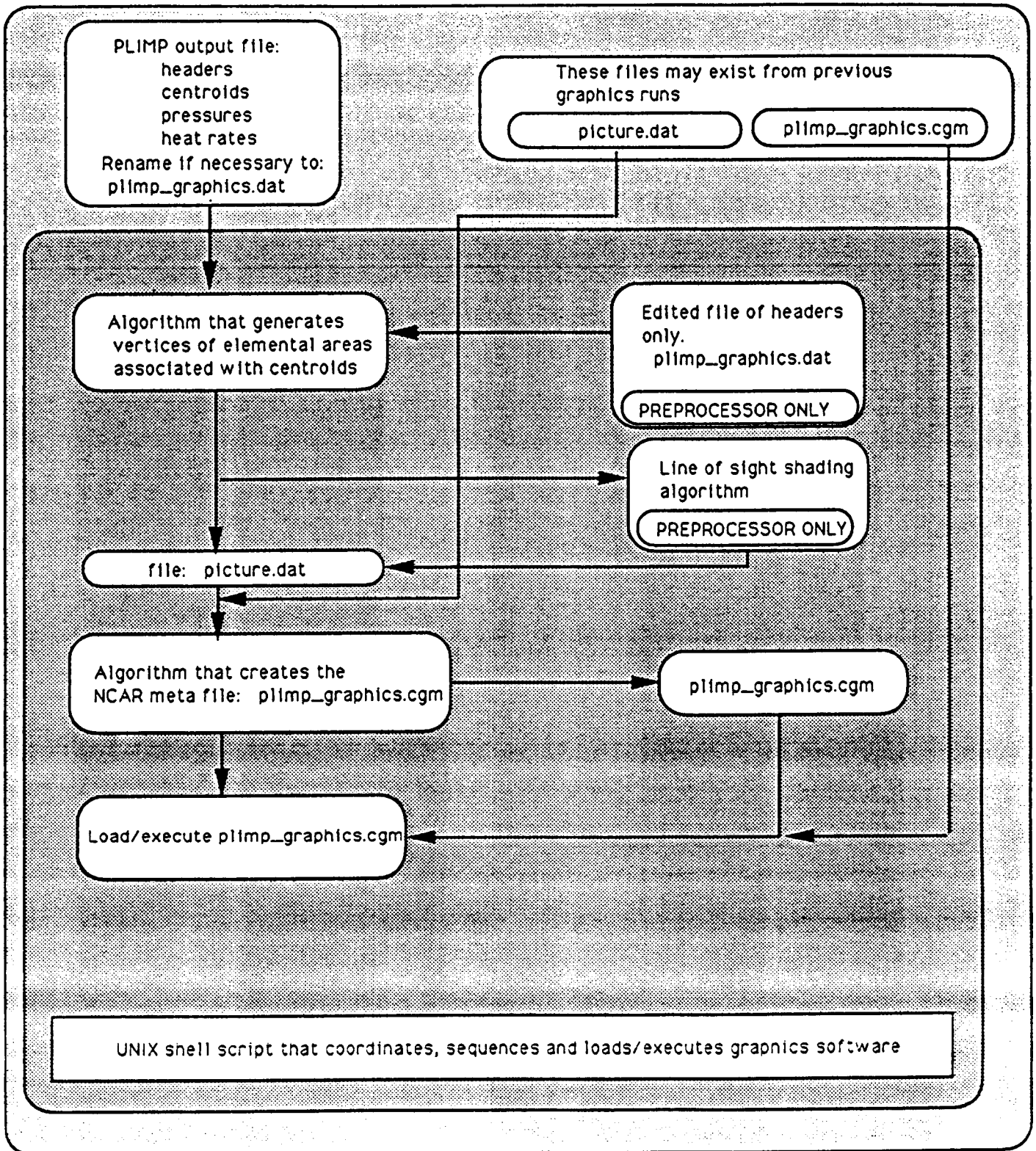


Figure 22: Flow Chart for Graphics Program

$$\begin{Bmatrix} x \\ y \\ z \end{Bmatrix}_R = \begin{bmatrix} T_1 \end{bmatrix} \times \begin{bmatrix} T_2 \end{bmatrix} \times \begin{bmatrix} T_3 \end{bmatrix} \begin{Bmatrix} x \\ y \\ z \end{Bmatrix}_I \quad (68)$$

where

T_1 = Rotation about the subshape x axis (θ)

T_2 = Rotation about the subshape y axis (ϕ)

T_3 = Rotation about the subshape z axis (ψ)

or

$$\begin{aligned} [T_1] &= \begin{bmatrix} 1 & 0 & 0 \\ 0 & \cos \theta & -\sin \theta \\ 0 & \sin \theta & \cos \theta \end{bmatrix}, \\ [T_2] &= \begin{bmatrix} \cos \phi & 0 & \sin \phi \\ 0 & 1 & 0 \\ -\sin \phi & 0 & \cos \phi \end{bmatrix}, \\ [T_3] &= \begin{bmatrix} \cos \psi & -\sin \psi & 0 \\ \sin \psi & \cos \psi & 0 \\ 0 & 0 & 1 \end{bmatrix} \end{aligned} \quad (69)$$

This transformation results in reference coordinates. Following is a discussion of the vertex calculations for each subshape.

Conic and Body of Revolution — Figure 23 illustrates the plane generation methodology for the conics and bodies of revolution. The planes generated are straight edged and do not curve with the surface. The vertex calculations conform to the sign convention shown in the figure and are:

$$x_1 = x - \Delta x/2$$

$$y_1 = r_1 \cos (\theta - \Delta\theta/2)$$

$$z_1 = r_1 \sin (\theta - \Delta\theta/2)$$

$$x_4 = x_1$$

$$y_4 = r_1 \cos (\theta + \Delta\theta/2)$$

$$z_4 = r_1 \sin (\theta + \Delta\theta/2)$$

$$x_2 = x + \Delta x/2$$

$$y_2 = r_2 \cos (\theta - \Delta\theta/2)$$

$$z_2 = r_2 \sin (\theta - \Delta\theta/2)$$

$$x_3 = x_2$$

$$y_3 = r_2 \cos (\theta + \Delta\theta/2)$$

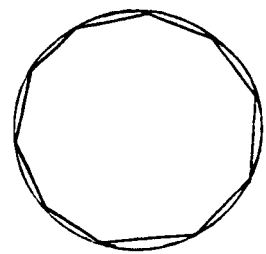
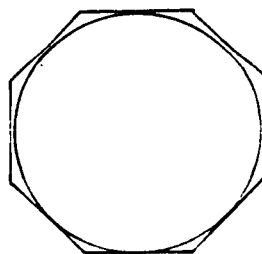
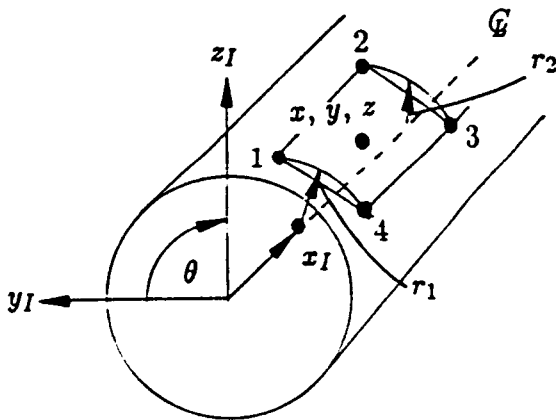
$$z_3 = r_2 \sin (\theta + \Delta\theta/2)$$

$\Delta\theta = \Delta\phi$ from Eq. 3

$$\theta = \tan^{-1} \left(\frac{z}{y} \right)$$

Positive θ rotates Y into Z.

r_1 and r_2 are functions of x_1, x_2, x_3, x_4 defined by conic and body of revolution functions.



More Theta Divisions Result in Better Graphics

Figure 23: Plane Generation for the Conic or Body of Revolution Subshapes

Rectangular Plate — Figure 24 illustrates the plane generation methodology for the rectangular plate. The vertex calculations are:

All x 's = 0

$$y_1 = y + \Delta y/2$$

$$z_1 = z + \Delta z/2$$

$$y_3 = y_4$$

$$z_3 = z_2$$

$$y_2 = y_1$$

$$z_2 = z - \Delta z/2$$

$$y_4 = y - \Delta y/2$$

$$z_4 = z_1$$

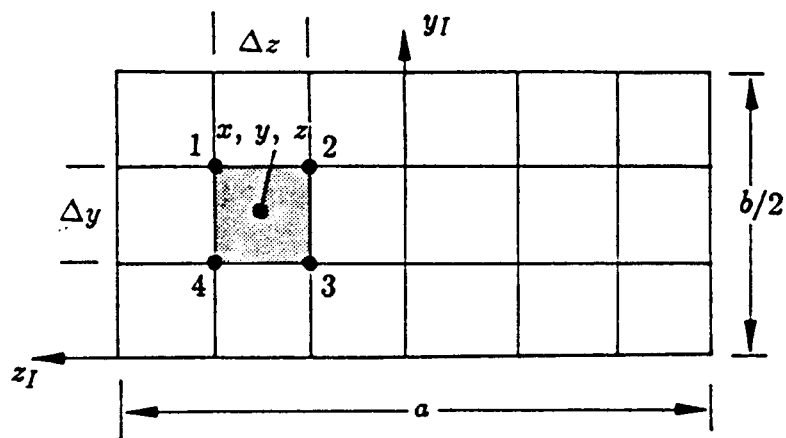


Figure 24: Plane Generation for Rectangular Plate Subshape

Circular Plate — Figure 25 illustrates the plane generation methodology for a circular plate. The element generated is a polygon of four edges, except for the case where $r_i = 0$. At $r_i = 0$, the most interior planes are triangles with a vertex at (0, 0, 0). The vertex calculations are:

$$y_1 = \cos (\theta + \Delta\theta/2) (r + \Delta r/2)$$

$$y_3 = \cos (\theta - \Delta\theta/2) (r - \Delta r/2)$$

$$z_1 = \sin (\theta + \Delta\theta/2) (r + \Delta r/2)$$

$$z_3 = \sin (\theta - \Delta\theta/2) (r - \Delta r/2)$$

$$y_2 = \cos (\theta - \Delta\theta/2) (r + \Delta r/2)$$

$$y_4 = \cos (\theta + \Delta\theta/2) (r - \Delta r/2)$$

$$z_2 = \sin (\theta - \Delta\theta/2) (r + \Delta r/2)$$

$$z_4 = \sin (\theta + \Delta\theta/2) (r - \Delta r/2)$$

$\Delta\theta = \Delta\phi$ from Eq. 6

Positive θ rotated Y into Z.

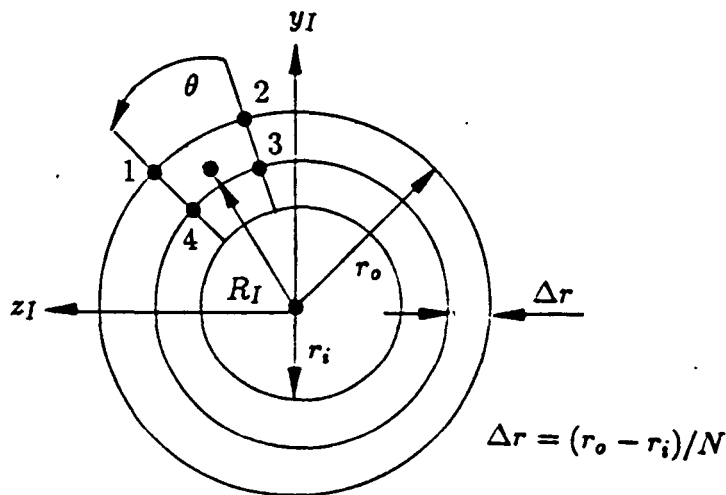
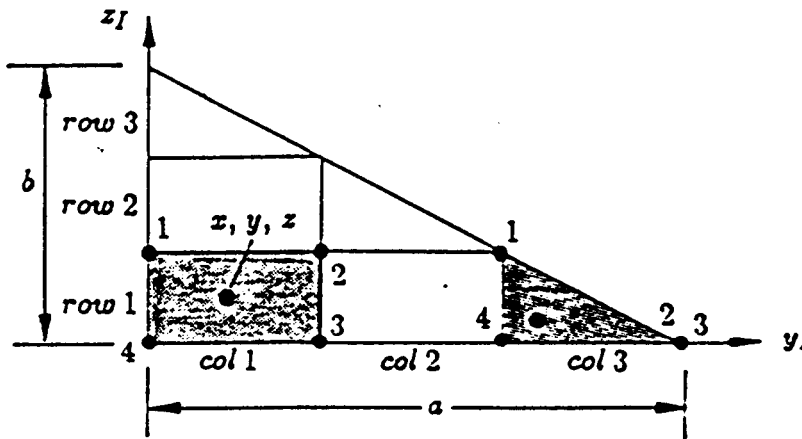


Figure 25: Plane Generation for Circular Plate Subshape

Triangular Plate — Figure 26 illustrates the plane generation methodology for the triangular plate. The elements generated are four-sided polygons, except at the edge where triangles are used. The triangle is divided into the same number of rows as columns; however, dimensions A and B can be different. The vertex calculations are:

<u>For Edge Planes</u>	<u>For Non-edge Planes</u>
$y_1 = n \Delta y - \Delta y$	$y_1 = y - \Delta y/2$
$y_2 = n \Delta y$	$y_2 = y + \Delta y/2$
$y_3 = y_2$	$y_3 = y_2$
$y_4 = y_1$	$y_4 = y_1$
$z_1 = m \Delta z$	$z_1 = z + \Delta z/2$
$z_2 = m \Delta z - \Delta z$	$z_2 = z_1$
$z_3 = z_2$	$z_3 = z - \Delta z/2$
$z_4 = z_3$	$z_4 = z_3$

n = number of column, m = number of row
 Centroids at $1/3 \Delta y$, $1/3 \Delta z$ into plane for edge planes.



Total number of columns must equal total number of rows

Figure 26: Plane Generation for Triangular Plate Subshape

Trapezoidal Plate — Vertex calculations for the trapezoid subshape are determined by breaking the subshape into a rectangle and two triangles and using rectangular and triangular plate methodologies.

Preprocessing (plimp_graphics.dat) and Shading — PLIMP input can be viewed without executing the PLIMP solution to allow easy and fast verification of angular and spatial subshape relationships as well as subshape dimensional inputs. In addition to basic geometric viewing, the graphics preprocessor will allow the user to view the results of line-of-sight shading. This feature can be used as both a check to the PLIMP shading results as well as a tool for identifying regions or zones on the composite body that are shaded. Such knowledge could be used to reduce the number of subshapes in the solution and avoid modeling a subshape that is know to be shaded.

Edited file of headers (modified plimp_graphics.dat) — The preprocessor version of plimp_graphics.dat is the same file that the postprocessing graphics algorithm reads with one modification and one deletion. The file plimp_graphics.dat must be modified such that the initial data item at the top of the file is either a zero or a one. A one indicates that the centroids, pressures and heat rates do not exist, and therefore, should be used for preprocessing needs. Second, the centroids, pressures and heat rate data are omitted from the normal PLIMP output file. An example plimp_graphics.dat for preprocessing is shown in Fig. 27.

Shading — Line-of-sight shading is an option available in the preprocessing algorithm. The algorithm initially sorts all the individual centroids, generated by the graphics code in the order of their distance from the nozzle. The algorithm starts with the last plane (N) in the sorted array and checks all planes preceding it, starting at (N-1), for shading plane N. Once a plane preceding it is determined to cause shading on plane N, no

	1	←	FLAG INDICATING A PREPROCESSOR FILE
NUMBER OF SUBSHAPES ←	4		SUBSHAPE A IDENTIFICATION NUMBER
	6	←	
	24 24 0 1 1		
	0.05 0 0 0 0		
	0.2 -0.18 0 0 0 0 1 2 3		SUBSHAPE B IDENTIFICATION NUMBER
	6	←	
	22 22 0 1 1		
	0.075 0 0 0 0		
	0.6 -0.18 -0.5 0 -90 0 1 2 3		SUBSHAPE C IDENTIFICATION NUMBER
	6	←	
	6 10 10 0.3 1		
	0.007 0 0 0 0		
	0.75 -0.13 0.0 0 0 90 1 2 3		SUBSHAPE D IDENTIFICATION NUMBER
	6	←	
	6 15 15 0.45 1		
	0.04 0 0 0 0		
	0.95 -0.13 0.0 0 0 90 1 2 3		

Figure 27: Input for Preprocessing Subshapes

further checking is done and the (N-1) plane is checked for shading starting with plane N-2, etc. Three assumptions are required before a plane is determined to shade another plane. The first assumption is: only planes closer to the nozzle have the potential to shade planes farther away. The second requirement is that the angle between the vector going from the nozzle to the closer plane and vector going from the nozzle to the plane being checked for shading must be less than 90 deg. This check eliminates the obvious case of the closer plane being behind the nozzle. Finally, the third check is that a line passing between the nozzle and the centroid of the farther away plane must intersect the closer plane. The logic in the algorithm checks these assumptions in an order that results in the fastest elimination of planes that have no potential of shading. Sorting and then looping the check logic on the ordered array assures an efficient first assumption check. The dot product check of angles between vectors provides the second check. If these two checks are made without causing the closer plane to be eliminated, then the more lengthy process of checking for the last requirement is initiated. This last check is performed using a multistep process.

First, the vertices of the closer plane are used to determine the plane equation:

$$ax + by + cz + d = 0 \quad (70)$$

Second, the parametric equation of a line in 3D space is found for the line connecting the nozzle and the centroid of the potentially shaded plane.

$$\begin{aligned} x &= x_0 + (x_1 - x_0)t \\ y &= y_0 + (y_1 - y_0)t \\ z &= z_0 + (z_1 - z_0)t \end{aligned} \quad (71)$$

Third, these equations are plugged into the plane equation, solved for t , and an intersection point is found.

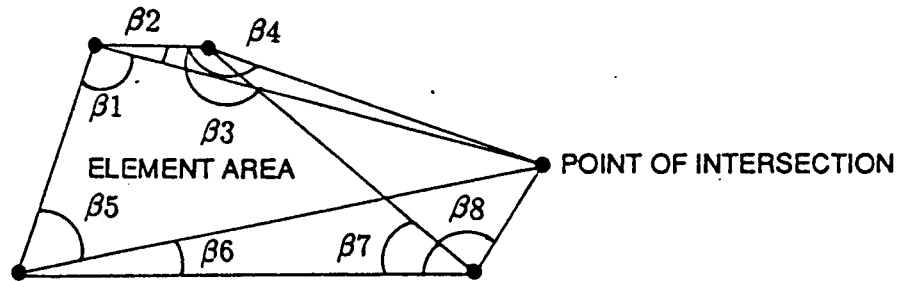
The following rationale is now used to determine if the intersection is inside the boundaries. The vectors bounding the plane are defined as vector 1, vector 2, vector 3, and vector 4 for a four-sided element. A triangle would have one of these vectors zero length. Another four vectors are defined between each vertex and the intersection point.

In order for the point to be in the element, $\sum_{i=1}^8 \theta_i = 360$ deg for a four-sided element and 180 deg for a triangle. Figure 28 illustrates this.

The shading algorithm has great potential for divide-by-zero floating point errors, but certain known causes can be averted by the user. For example, a Cramer's rule algorithm in the plane definition calculation can cause a floating point divide by zero. This occurs if plates and triangles that have all zero x-value coordinates in the subshape coordinate system are set up such that these x-values (for all points) are also maintained in the reference coordinate system. For example a plate with a (0, 0, 0) offset from the reference system and with a (0, 0, 0) angle orientation.

As a final note on shading, it is pointed out that by using only centroids to establish the 3D line in space to perform intersection calculations, visual "bleed-through" of shaded

PLANS RESULTING FROM PLANE EQUATION



FOR 4 SIDED, IF $\beta_1 + \beta_2 + \beta_3 + \beta_4 + \beta_5 + \beta_6 + \beta_7 + \beta_8 = 360$, POINT OF INT IS IN AREA
 FOR 3 SIDED, IF $\beta_1 + \beta_2 + \beta_3 + \beta_4 + \beta_5 + \beta_6 + \beta_7 + \beta_8 = 180$, POINT OF INT IS IN AREA

Figure 28: Shading Determination Using Summation of Angles at Vertices

planes often results. Figure 29 illustrates this. The shading is exact and correct; however, the user may question the apparent shaded planes along the intersecting lines where impingement obviously exists. These blue colors exist because the centroid of these planes is shaded, and the portion of the plane visible reflects the centroid calculations. A finer mesh will help attenuate this, but it will come at the expense of slower preprocessing run time.

Three frames of different perspectives of the composite model are drawn along with one perspective for each subshape in the composite and stored in NCAR's meta file under the name `plimp_graphics.cgm`. The color scheme used to color each picture is based on the magnitude of the specific surface condition being plotted.

The entire plane, defined by its vertices, which are projected from 3D to 2D screen coordinates is filled with the color associated with this hue value. The color code was set up so that red is associated with hot or high magnitude and blue is associated with cold or low magnitude. The large variations in magnitudes between centroids representing hot regions and centroids representing cold regions necessitated use of the log function. A simple linear function would leave the picture with a small zone of red and a large zone of blue. The hue is, therefore, set to:

$$hue = 36 \log_{10}(Magnitude) \tag{72}$$

Figures 30 through 33 illustrate examples of pre- and postprocessing results using the graphics software. Figure 30 illustrates the preprocessing graphics resulting from the input shown in Fig. 27. Figure 31 illustrates the shading available in the preprocessing graphics. The blue region represents shaded surface area and the coordinate axis represents the nozzle origin with +z as the general flow direction. Figure 32 depicts the results of postprocessing a PLIMP solution for the geometry defined in Fig. 27. Note that the postprocessing graphics includes a color bar associating color regions with surface intensity. Finally, Fig. 33 illustrates another frame of the same drawing as Fig. 32. Recall

x - axis is nozzle centerline
y-z plane is nozzle exit

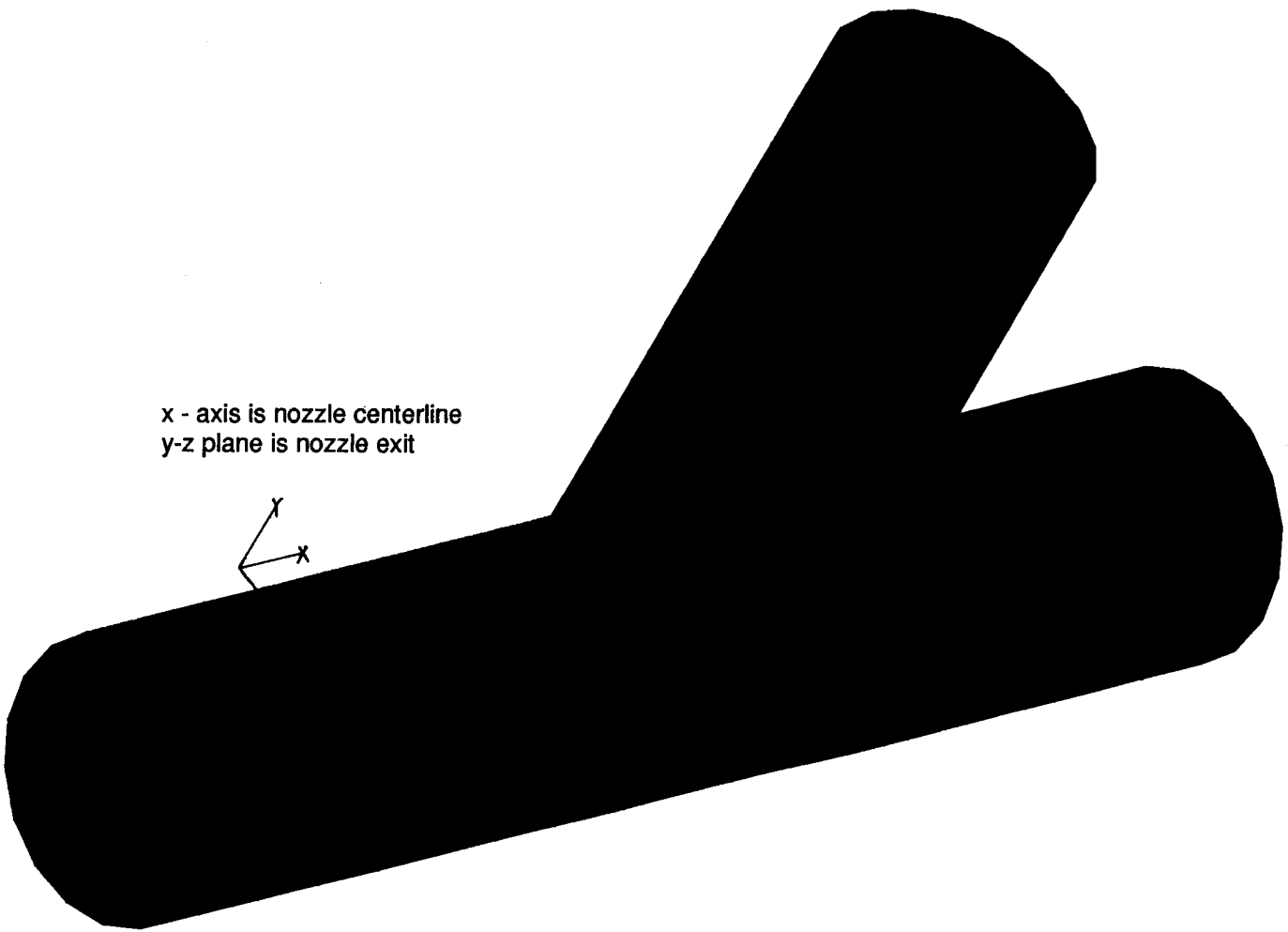


Figure 29: "Bleed-Through" Caused by Centroid Shading but Element Not Completely Shaded

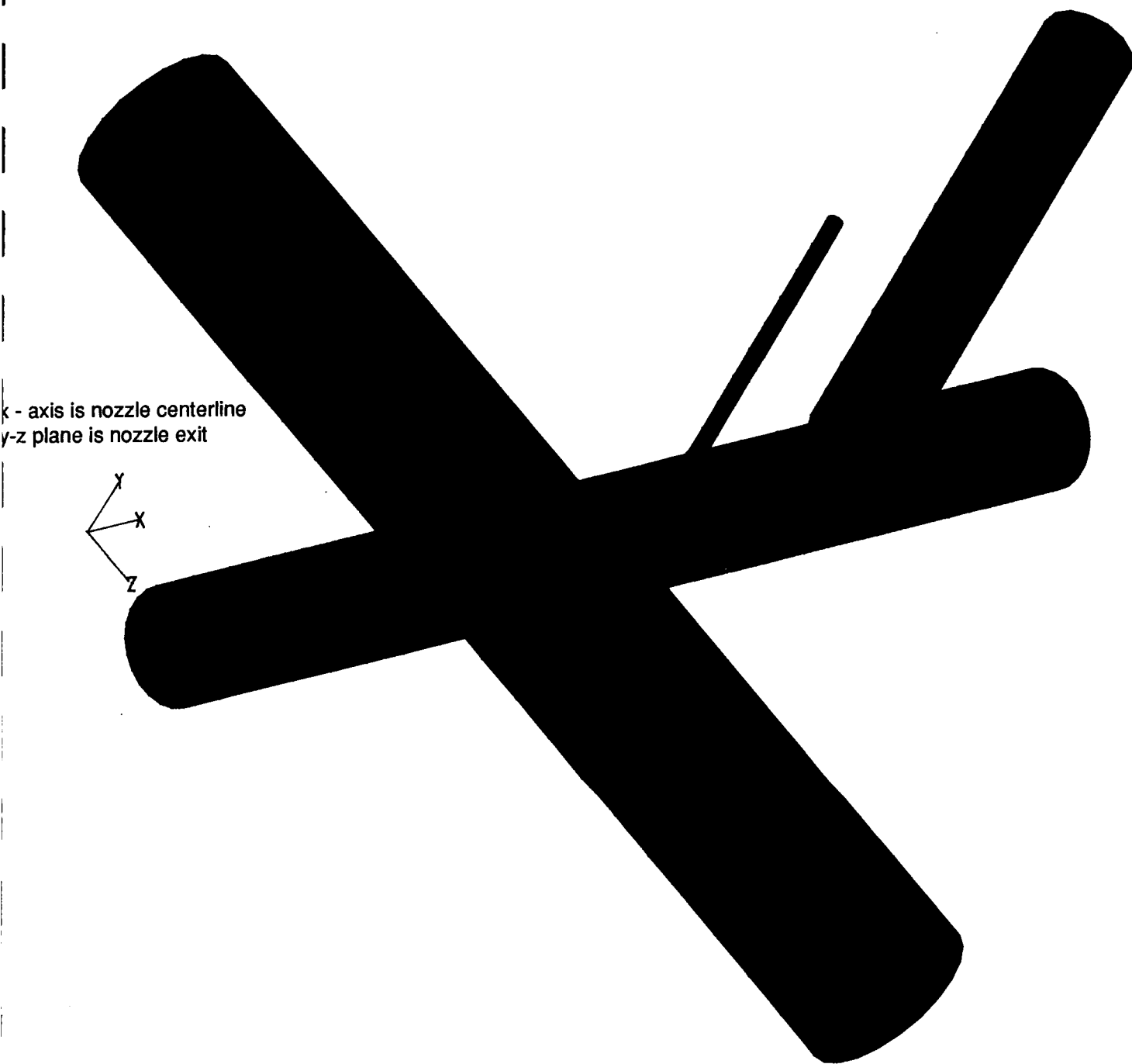


Figure 30: Preprocessing Results with No Shading

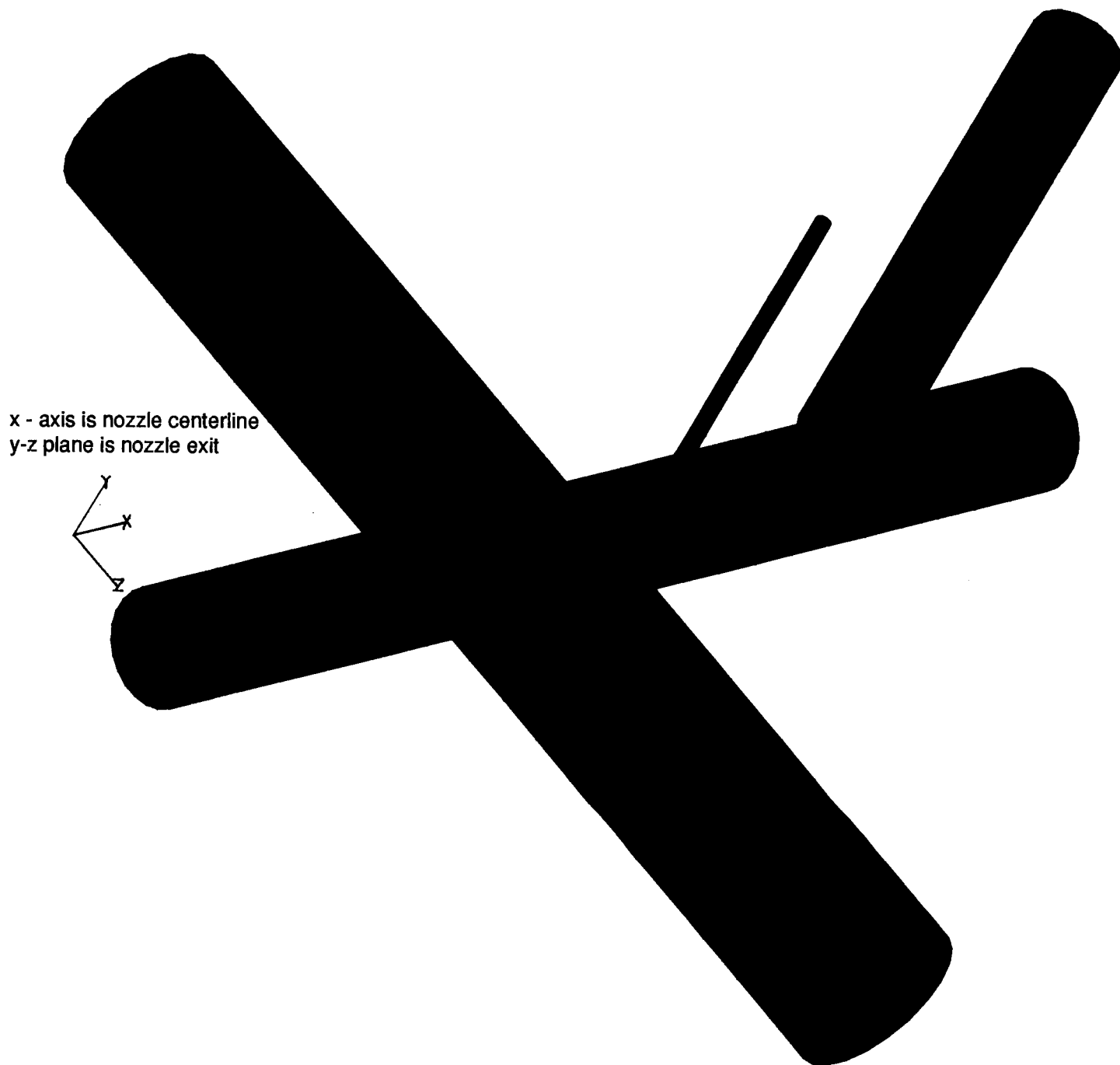


Figure 31: Preprocessing Results with Predicted Shading

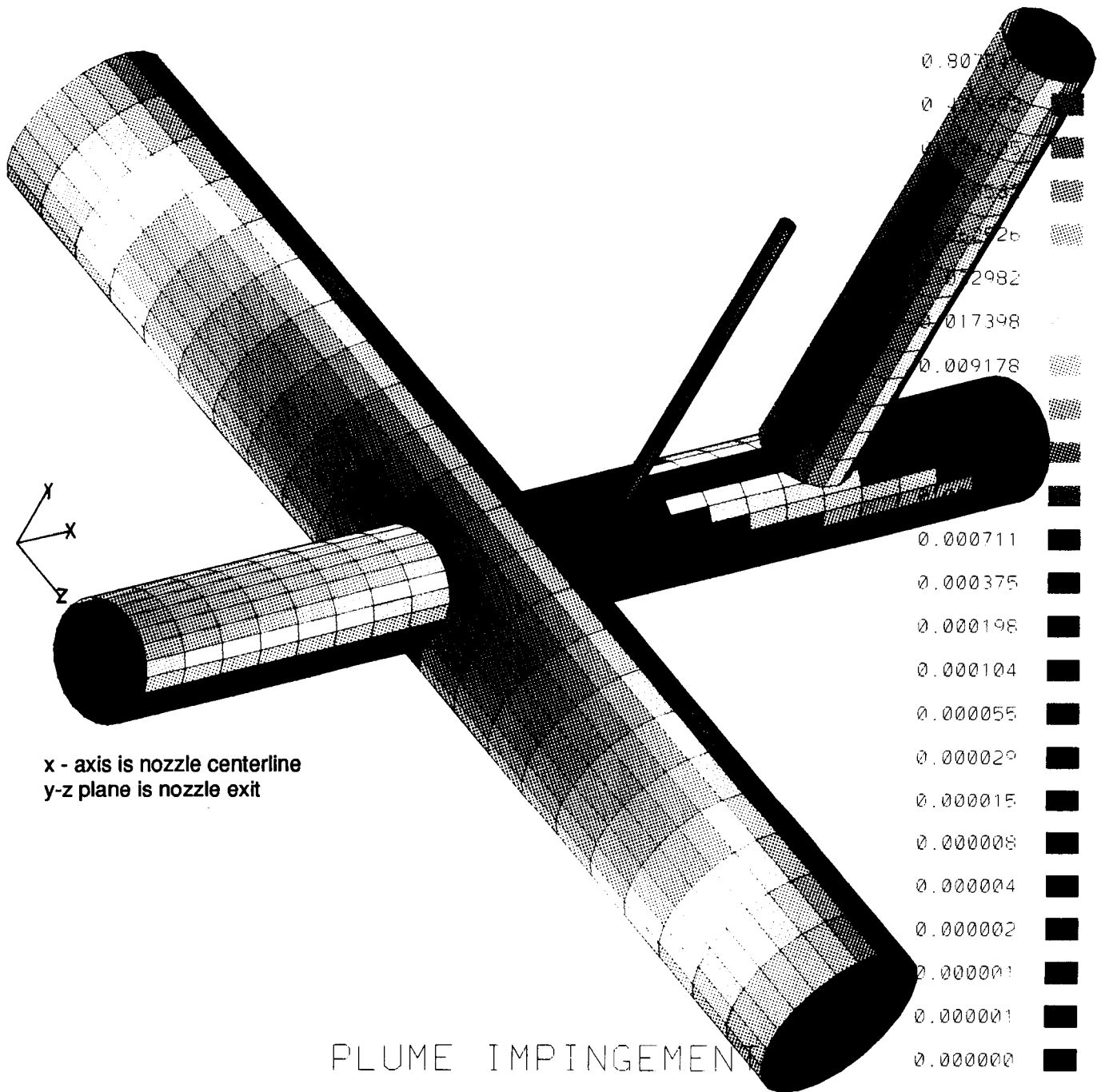
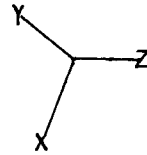
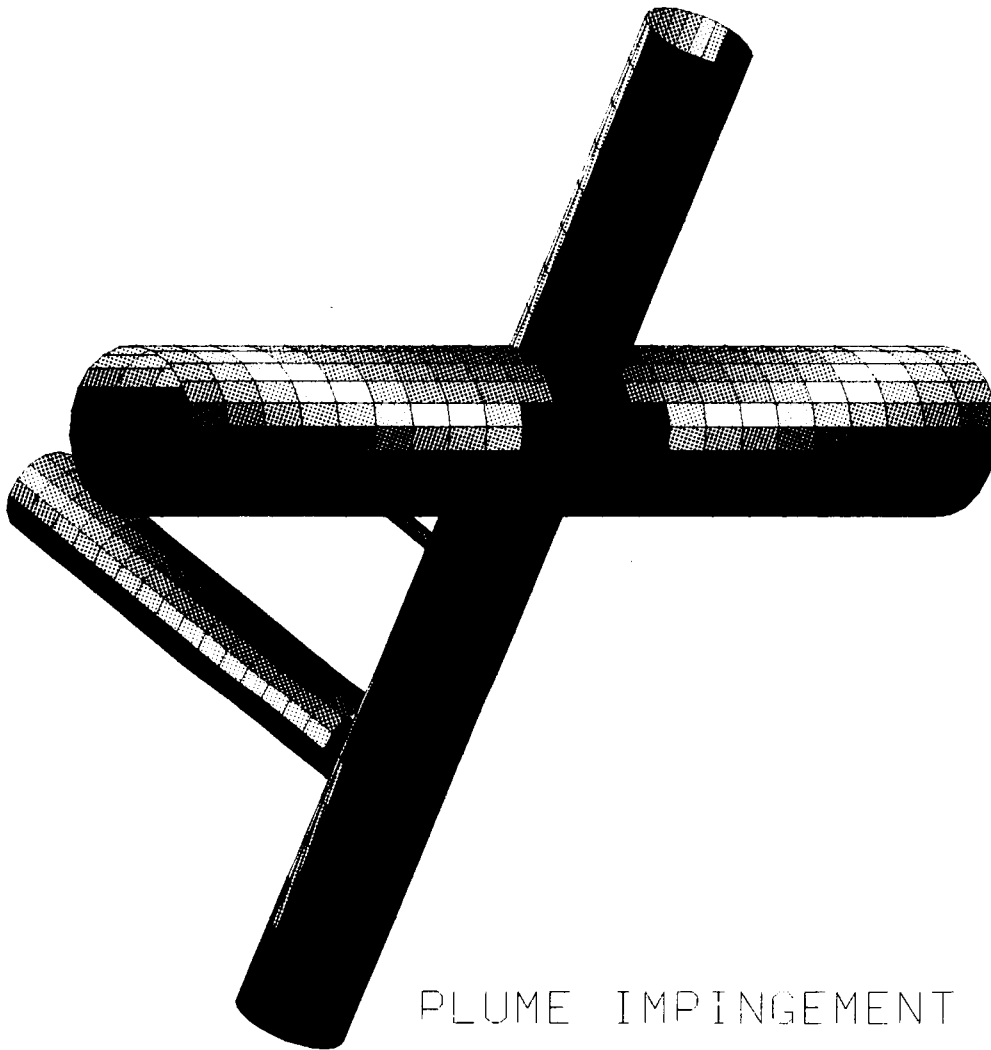


Figure 32: Post Processing Results — Top View



x - axis is nozzle centerline
y-z plane is nozzle exit



0.807549	■
0.425982	■
0.224705	■
0.118532	■
0.062526	■
0.032982	■
0.017398	■
0.009178	■
0.004841	■
0.002554	■
0.001347	■
0.000711	■
0.000375	■
0.000198	■
0.000104	■
0.000055	■
0.000029	■
0.000015	■
0.000008	■
0.000004	■
0.000002	■
0.000001	■
0.000001	■
0.000000	■

Figure 33: Postprocessing Results — Bottom View

that three frames representing different views of the composite geometry and frame depicting one view of each subshape are available.

3.3.5.3 Code Execution and Use

The file `plimp_graphics.f` contains all the FORTRAN routines, and the file `run_ncar` contains the UNIX code that interfaces with the FORTRAN algorithms and coordinates file activity.

To execute the graphics software, for either pre or postprocessing, type the command:

```
run_ncar plimp_graphics
```

This command will spawn the graphics process. If the `plimp_graphics` is omitted from the command, the shell script will not execute properly. Once compiled, the program will not need recompiling.

Initially, the shell script asks you if you want to plot an existing `.cgm` file. As mentioned, a `.cgm` file is a meta file generated by NCAR that contains device independent drawing commands pertaining to a previous execution of the code. If such a file exists from a previous run and you want to view it again, simply type "yes" in lower case. If you did not rename the file, it will be called `plimp_graphics.cgm`; however, if you renamed it to another name, (retaining the suffix `.cgm`) then simply type the new name.

Assuming you did not want to plot an existing `.cgm` file, the software will ask you if you need to rename the output file from PLIMP. This question pertains to postprocessing and is needed because the post processor reads PLIMP output from the file `plimp_graphics.dat`. The PLIMP code was modified to format output compatible with input requirements and only the PLIMP output file name needs to be checked. If you have called the PLIMP output any name other than `plimp_graphics.dat`, then enter "yes" (lower case).

The next prompt from the terminal concerns a file called `picture.dat`. This is the file generated by the FORTRAN routines that contains all vertex data in the reference coordinate system. Because the code is written as if this file is new, an error will occur if it already exists in your directory.

The software will next question the user if recompilation is needed. If compilation was already performed, it does not have to be recompiled.

Now that basic file activities are handled, the program inquires as to what processor you intend to use; pre or post. Three options are given:

1. PREPROCESSING
2. POSTPROCESSING (without `picture.dat` existing)
3. POSTPROCESSING (with `picture.dat` already existing)

The last option informs the processor that vertices have already been generated and this chore does not have to be performed, so the already existing `picture.dat` file can be used.

The next prompt is:

1. CREATE AND PLOT `picture.dat`?

2. USE GRAPHICS PREPROCESSOR?

This prompt directs the path of execution toward either pre or postprocessing. Regardless of your answer, the program expects that the file `plimp_graphics.dat` exists. If you are postprocessing, it will be output from PLIMP, otherwise you must have generated it using an editor to type in the headers for each subshape. If postprocessing is being performed, then the software will pause for up to several minutes before displaying a self-explanatory, mouse-driven NCAR menu that you just follow. If preprocessing is being performed, an additional prompt will ask you if shading is requested. Note that the addition of shading will slow processing speed. Again, up to several minutes will pass before the NCAR menu is displayed.

3.4 Ordered Flowfields

One of the objectives of this study was to establish a data base of precomputed plume flowfields that can be used by PLIMP to predict high altitude plume induced environments. Over the course of the past several years, numerous plumes have been computed using the RAMP2 computer code. As a result, there are a wide variety of input cases previously prepared for computing various exhaust plumes. The plume flowfields were recomputed using the RAMP2 code on an in-house DEC MicroVAX computer. The resulting flowfields were archived onto magnetic tape [29]. Due to the complexity of the RAMP2 execution sequence, several flowfields required modifications to the RAMP2F computer code, and different executables were required to generate these plumes. Therefore, the TRAN72, BLIMPJ, and RAMP2F source codes, executables, and VAX command files were also included on this tape. A brief summary of the contents of each file on this tape is presented in Appendix B.

Sourceflow approximations were calculated using the SFPGEN computer code for each of these flowfields. The major advantages of using SFPGEN to produce these flowfields for PLIMP are: the flowfield is portable between different computers; the flowfield requires considerably less storage than the RAMP2 flowfield; the PLIMP calculations are faster; and the sourceflow plume can be determined to much larger distances than are practical using the RAMP2 code.

Five categories of engines were included in this study: bi-propellant engines; H₂/O₂ engines; hydrazine (monopropellant) engines; cold gas thrusters; and solid propellant engines. The engine types are summarized in Table 4 which also lists output sourceflow data files for those plumes input to SFPGEN. These data files are also archived on magnetic tape [30].

3.4.1 Bi-Propellant Engines

The following six engines were included in this section:

1. Space Shuttle Vernier RCS Engine
2. Space Shuttle Primary RCS Engine (Constant and Variable O/F)
3. AJ10-181

4. BP14
5. Marquart R2
6. R6C

RAMP2 and SFPGEN sourceflow plume flowfields were generated for all six engines. The propellants consisted of an oxidizer (nitrogen tetroxide — N_2O_4) and a fuel (monomethylhydrazine — MMH). A complete set of engine geometric and operating characteristics is shown in Figs. 34 through 40 along with a plot of the density contours for each engine.

3.4.2 H₂/O₂ Engines

This section consisted of liquid hydrogen, liquid oxygen engines. The following engines were analyzed:

1. Space Station ACS Engine
2. Space Shuttle Main Engine
3. Nuclear Engine

RAMP2 and SFPGEN sourceflow plume flowfields were generated for the ACS engine and the nuclear engine. The density contours and operating characteristics for these engines are presented in Figs. 41 and 42. The nozzle solution was calculated for the SSME; neither a boundary layer nor a plume restart was performed.

3.4.3 Hydrazine Engines

Seven engines were included in the monopropellant section:

1. 0.5 Newton Hydrazine Engine
2. 1 lbf Thrust Hydrazine Engine
3. REA-MONO-A
4. MRE15
5. AFE 30 lbf RCS
6. 7.49 lbf Thrust Hydrazine Engine
7. REA-15

RAMP2 and SFPGEN sourceflow plume flowfields were generated for all seven engines. The engine geometric and operating characteristics, along with the density contours are presented in Figs. 43 through 49.

3.4.4 Cold Gas Thrusters

This section consisted of helium thrusters, nitrogen thrusters, and carbon dioxide and air sonic orifices. RAMP2 and SFPGEN flowfield files were generated for the following engines:

1. AFE Gaseous Helium Thruster
2. OMV Nitrogen Thruster
3. AEDC CO₂ Sonic Orifice

4. JPL GN2
5. Space Station EVA Free Sonic Vent (4 inch diameter)
6. Space Station EVA Stringer Vent (1 inch diameter)
7. Space Station EVA Stringer Vent (4 inch diameter)
8. Space Station Hyperbaric Vent

The density contours and engine geometric and operating characteristics are presented in Figs. 50 through 57 for each thruster.

3.4.5 Solid Propellant Engines

RAMP2 and SFPGEN plume flowfields were generated for only one engine, the STAR63 engine (AFE Ignition Motor). The Advanced Solid Rocket Motor (ASRM) and the Space Shuttle High Performance Motor are mainly low altitude engines and therefore sourceflow plumes cannot be generated for them. The nozzle solutions for each engine are included on magnetic tape [29]. Figure 58 presents the density contours and operating characteristics for the STAR63 motor.

Table 4: Flowfields Generated for "Canned" Plume Data Base

Bi-Propellant Engines	Space Shuttle Vernier RCS Engine •SDF: VERNUN16.DATSOR Space Shuttle Primary RCS Engine ($A/A^* = 22$) •Constant O/F SDF: RCSCONSTUN16.DATSOR •Variable O/F SDF: RCSVOFUN16.DATSOR AJ10-181 ($A/A^* = 93$; 5 lbf Thrust) •SDF: AJ10UN16.DATSOR BP14 (21 lbf Thrust; $A/A^* = 45$) •SDF: BP14UN16.DATSOR Marquart R2 (11 lbf Thrust) •SDF: LMSCUN16.DATSOR R6C ($A/A^* = 150$; 5 lbf Thrust) •SDF: R6CUN16.DATSOR
H2/O2 Engines	Space Station ACS Engine •SDF: ACSUN16.DATSOR Space Shuttle Main Engine (SSME) Nuclear Engine (Solid Cone; $A/A^* = 200$; 70000 lbf Thrust) •SDF: NUCUN16.DATSOR
Hydrazine Engines (Monopropellant)	0.5 Newton; $A/A^* = 41$ •SDF: MONO5UN16.DATSOR 1 lbf Thrust; $A/A^* = 50$ •SDF: FONG1UN16.DATSOR

Table 4: (Continued) Flowfields Generated for "Canned" Plume Data Base

<p>Hydrazine Engines (Monopropellant)</p>	<p>REA-MONO-A (30 lbf Thrust; $A/A^* = 79$) •SDF: MONO3BUN16.DATSOR MRE15 (OMV RCS) ($A/A^* = 50$) •SDF: MRE15UN16.DATSOR AFE 30 lbf RCS •SDF: RCS30UN16.DATSOR Hydrazine Engine ($A/A^* = 50$) •SDF: MOD2UN16.DATSOR REA 15 ($A/A^* = 50$) •SDF: REA15UN16.DATSOR</p>
<p>Cold Gas Thrusters</p>	<p>AFE Gaseous Helium Thruster •SDF: AFE GHEUN16.DATSOR OMV Nitrogen Thruster •SDF: OMVGN2UN16.DATSOR Sonic Orifices AEDC CO2 Sonic Orifice •SDF: AEDCSOINICUN16.DATSOR Air (Space Station) •EVA Free Sonic Vent (4" dia.) SDF: EVASON4UN16.DATSOR •Space Station EVA Stringer Vent (1" dia.) SDF: EVAST1UN16.DATSOR •Space Station EVA Stringer Vent (4" dia.) SDF: EVAST1UN16.DATSOR •Space Station Hyperbaric Vent SDF: HYPBARUN16.DATSOR JPL GN2 Nozzle •SDF: JPL1GN2UN16.DATSOR</p>
<p>Solid Propellant Engines</p>	<p>STAR63 (AFE Ignition Motor) •SDF: STAR63UN16.DATSOR Advanced Solid Rocket Motor (ASRM) Space Shuttle High Performance Motor (HPM)</p>

NOTE:
 SDF = Sourceflow Data File

SPACE SHUTTLE VERNIER RCS ENGINE	
THROAT RADIUS	0.01708333 ft
EXIT RADIUS	0.0782708 ft
AREA RATIO	21
NOZZLE LENGTH	0.2854167
CHAMBER PRESSURE	110 psia
AMBIENT PRESSURE	6.944E-08 psia
PROPELLANT	
Fuel	Monomethylhydrazine (MMH)
Oxidizer	N ₂ O ₄ (Nitrogen Tetroxide)
MASS FLOW RATE	0.082157 lb/sec
THRUST	25 lb
O/F RATIO	1.648

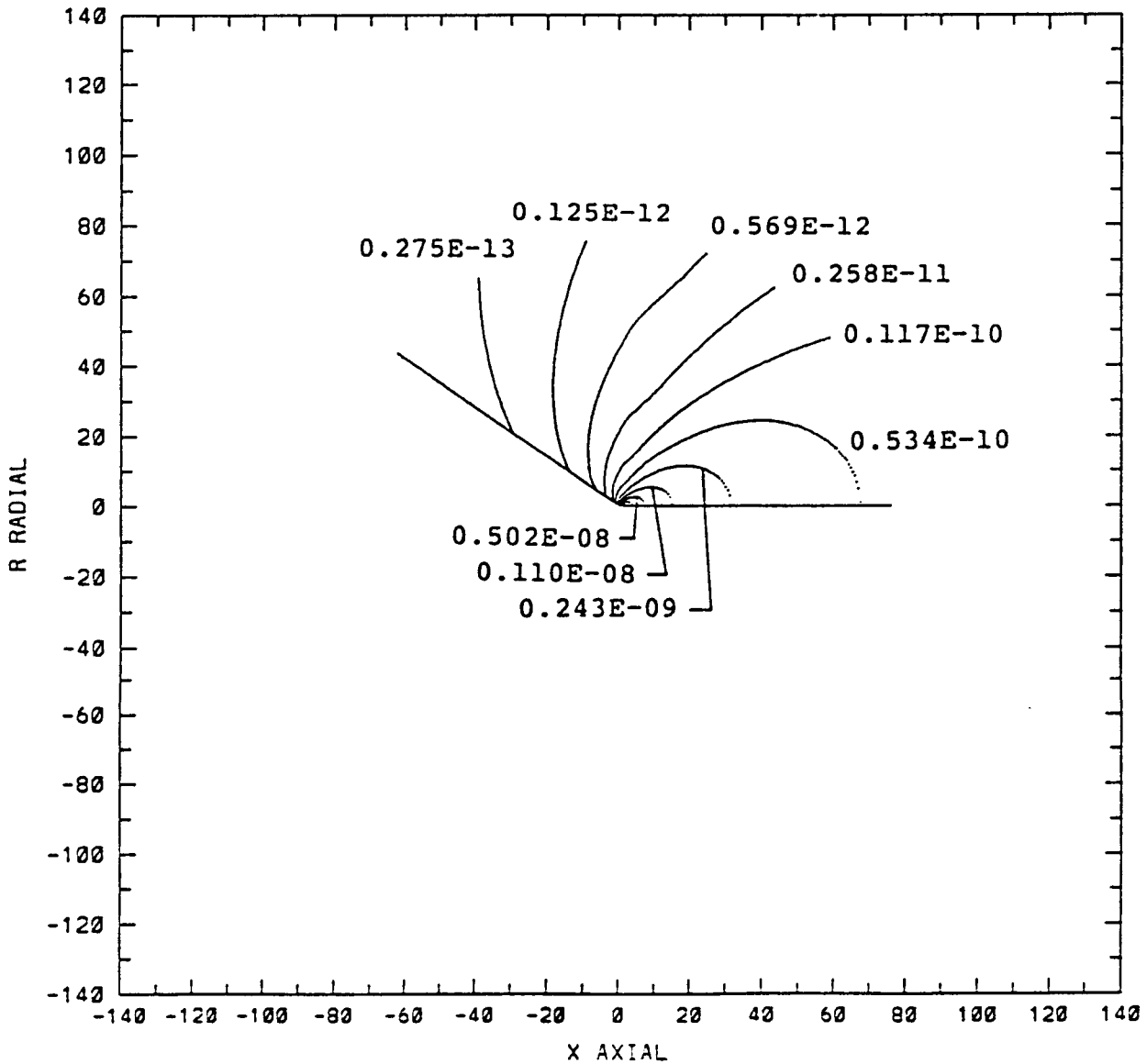


Figure 34: Density Contours: Space Shuttle Vernier RCS Engine

RCS ENGINE (CONSTANT O/F) ($A/A^* = 22$)	
THROAT RADIUS	0.0850833 ft
EXIT RADIUS	0.399917 ft
AREA RATIO	22
NOZZLE LENGTH	0.775 ft
CHAMBER PRESSURE	153 psia
AMBIENT PRESSURE	5.20E-08 psia
PROPELLANT	
Fuel	Monomethylhydrazine (MMH)
Oxidizer	N_2O_4 (Nitrogen Tetroxide)
MASS FLOW RATE	2.8295 lb/sec
THRUST	879.7 lb
O/F RATIO	1.6

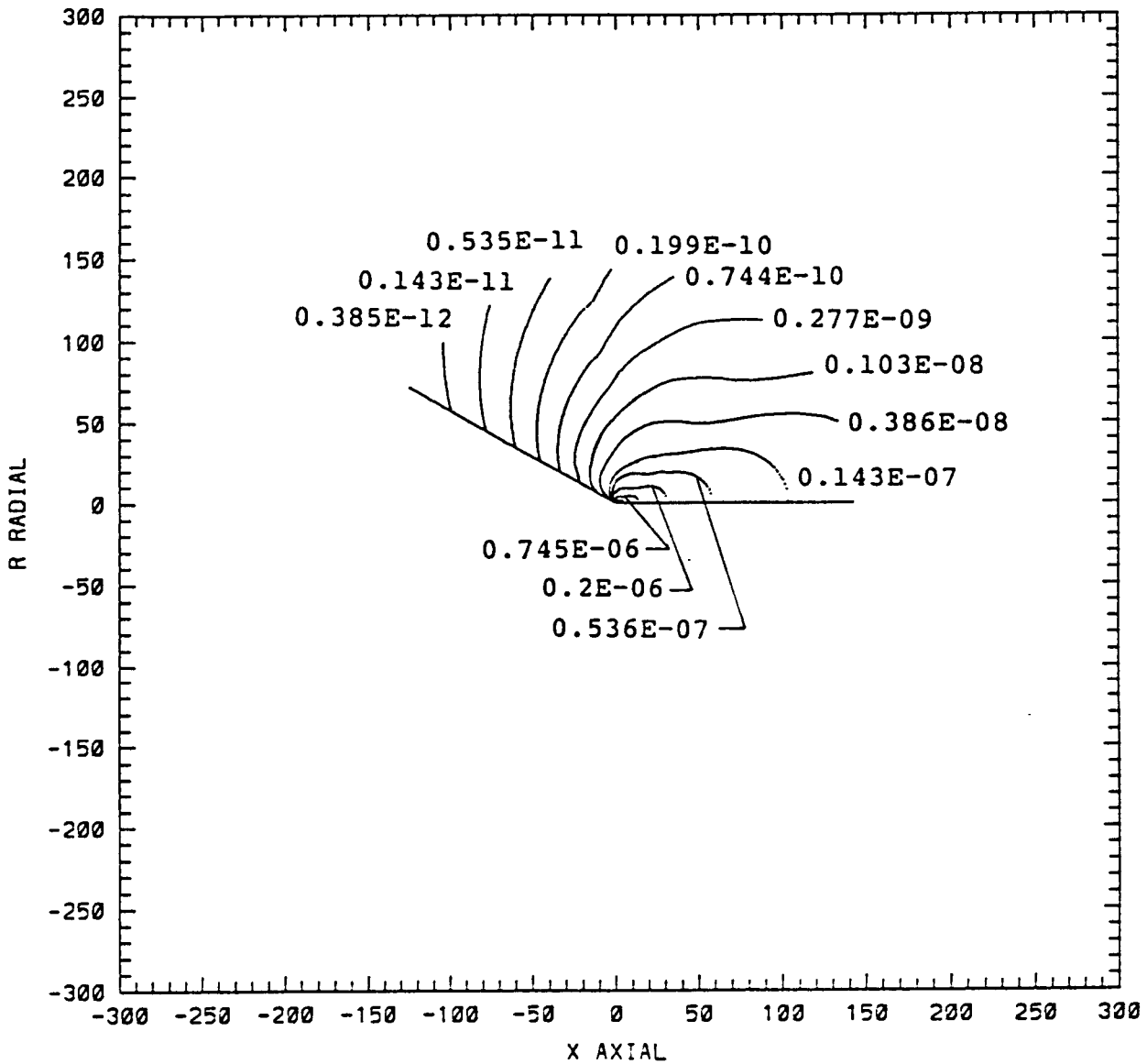


Figure 35: Density Contours: Space Shuttle Primary RCS Engine
 ($A/A^* = 22$) Constant O/F

RCS ENGINE (Variable O/F) ($A/A^* = 22$)	
THROAT RADIUS	0.0850833 ft
EXIT RADIUS	0.399917 ft
AREA RATIO	22
NOZZLE LENGTH	0.775 ft
CHAMBER PRESSURE	153 psia
AMBIENT PRESSURE	5.20E-08 psia
PROPELLANT	
Fuel	Monomethylhydrazine (MMH)
Oxidizer	N_2O_4 (Nitrogen Tetroxide)
MASS FLOW RATE	2.8506 lb/sec
THRUST	877 lb
O/F RATIO	Variable

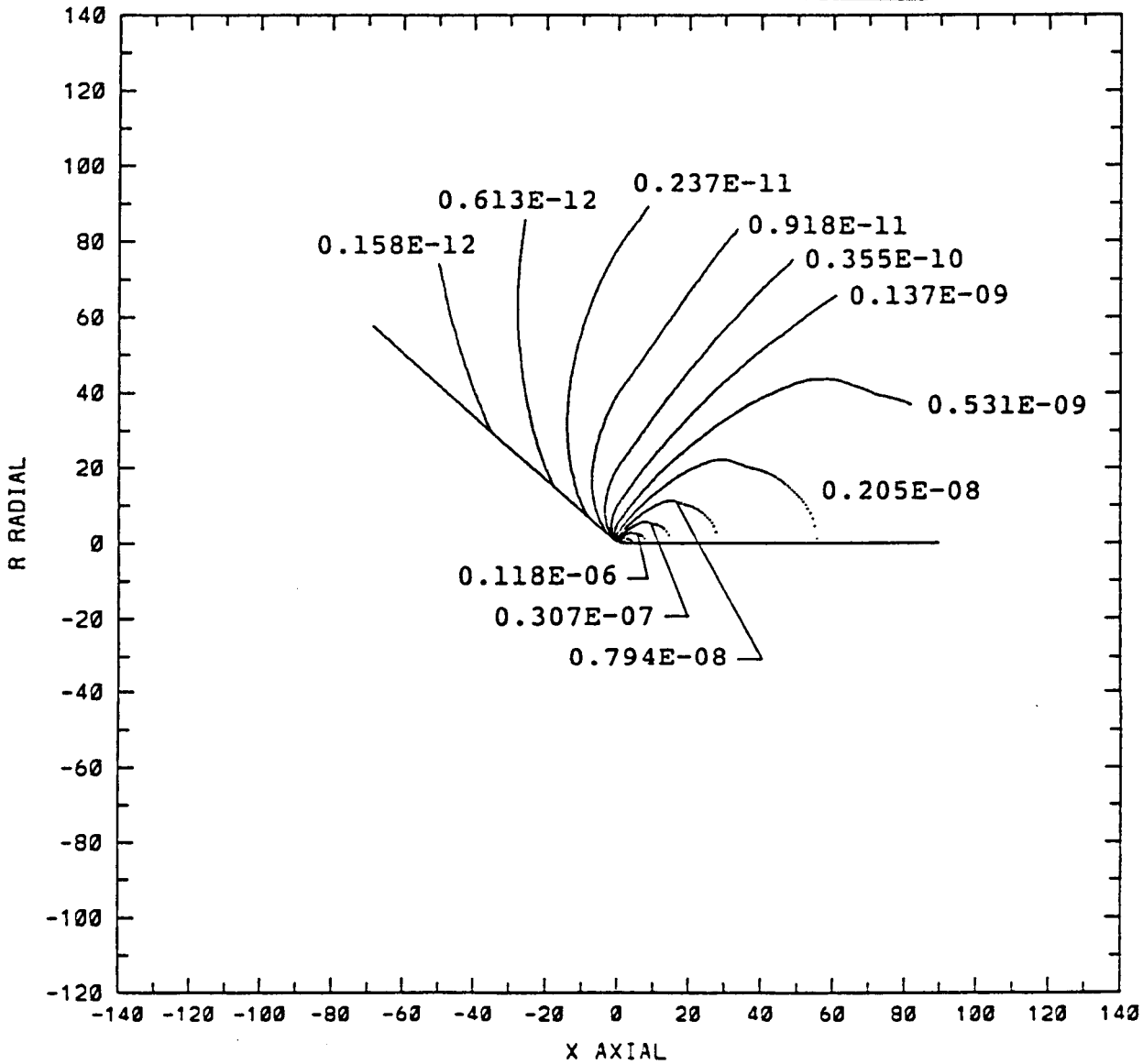


Figure 36: Density Contours: Space Shuttle Primary RCS Engine ($A/A^* = 22$) Variable O/F

AJ10-181 (A/A* = 93; 5 lbf thrust)	
THROAT RADIUS	0.0063333 ft
EXIT RADIUS	0.061106 ft
AREA RATIO	93
NOZZLE LENGTH	0.18247 ft
CHAMBER PRESSURE	100 psia
AMBIENT PRESSURE	7.986E-08 psia
PROPELLANT	
Fuel	Monomethylhydrazine (MMH)
Oxidizer	N ₂ O ₄ (Nitrogen Tetroxide)
MASS FLOW RATE	0.01024 lb/sec
THRUST	5 lb
O/F RATIO	1.6

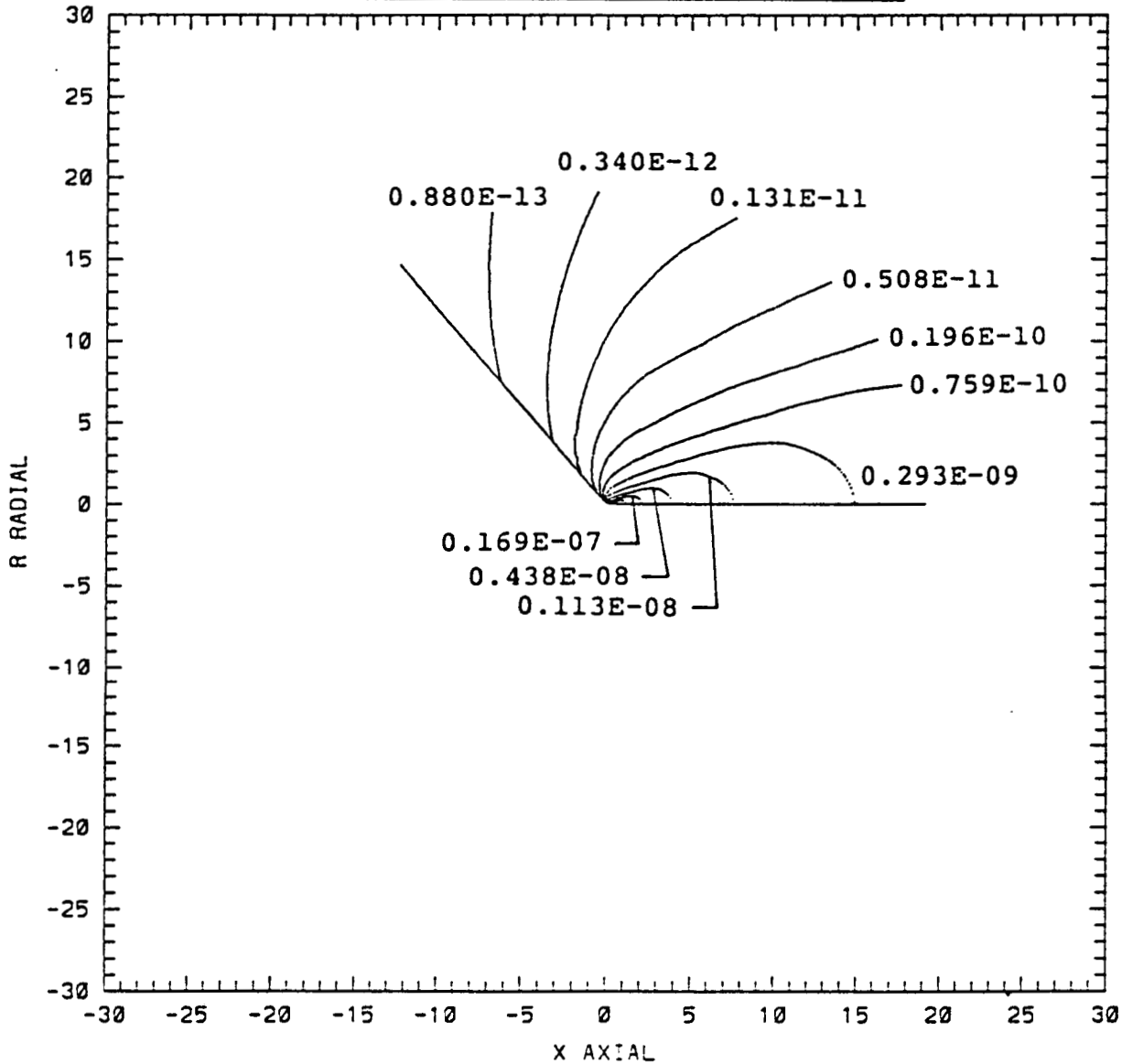


Figure 37: Density Contours: AJ10-181 (A/A* = 93; 5 lbf Thrust)

BP14 (A/A* = 45; 521lbf thrust)	
THROAT RADIUS	0.0135833 ft
EXIT RADIUS	0.09173 ft
AREA RATIO	45
NOZZLE LENGTH	0.3311667 ft
CHAMBER PRESSURE	140 psia
AMBIENT PRESSURE	7.548E-09 psia
PROPELLANT	
Fuel	Monomethylhydrazine (MMH)
Oxidizer	N ₂ O ₄ (Nitrogen Tetroxide)
MASS FLOW RATE	0.065756 lb/sec
THRUST	21 lb
O/F RATIO	1.65

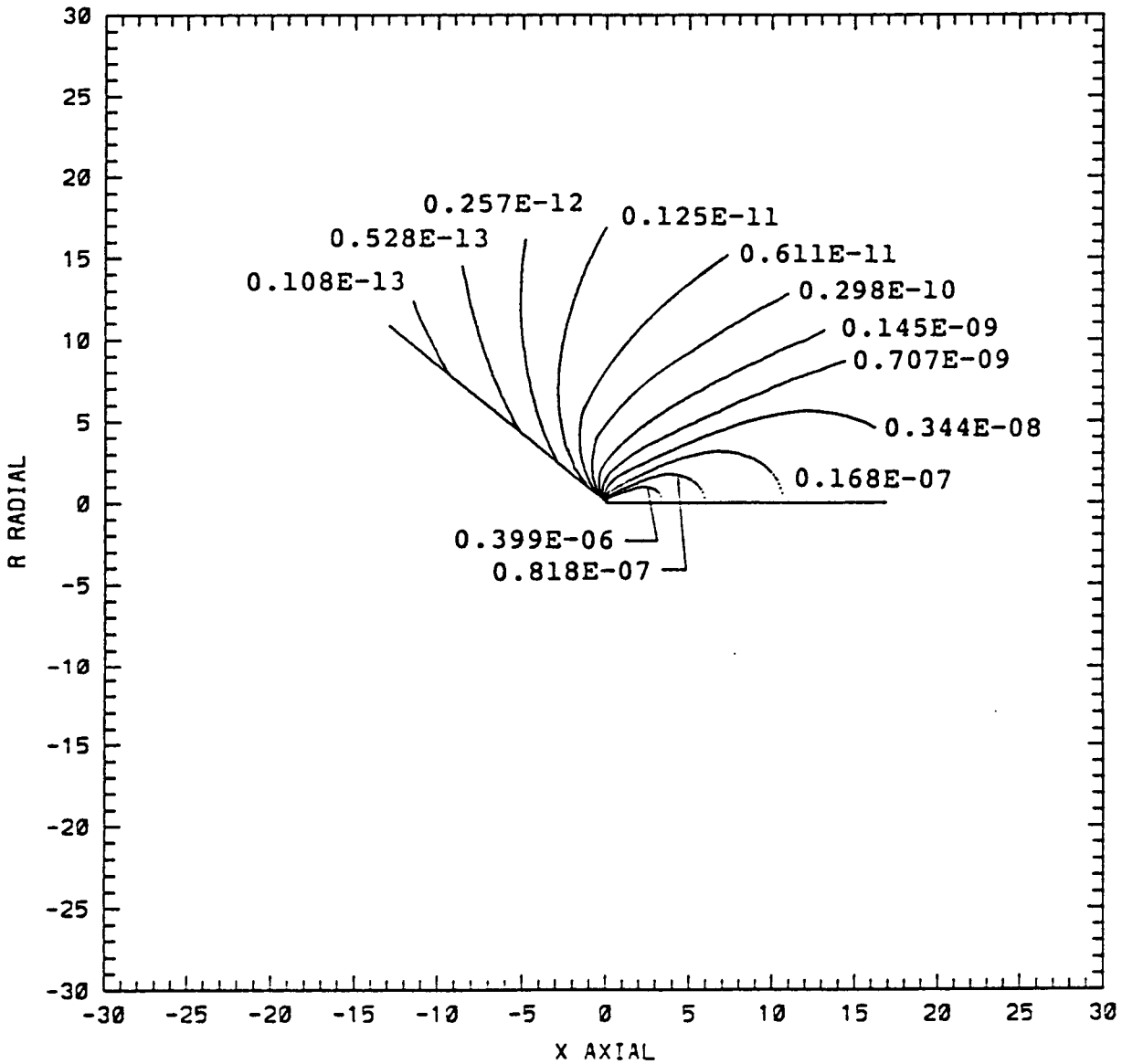


Figure 38: Density Contours: BP14 (A/A* = 45; 21 lbf Thrust)

MARQUART R2 (11lbf thrust)	
THROAT RADIUS	0.0034583 ft
EXIT RADIUS	0.037292 ft
AREA RATIO	116
NOZZLE LENGTH	0.10775 ft
CHAMBER PRESSURE	105.61 psia
AMBIENT PRESSURE	1.041E-09 psia
PROPELLANT	
Fuel	Monomethylhydrazine (MMH)
Oxidizer	N ₂ O ₄ (Nitrogen Tetroxide)
MASS FLOW RATE	0.003217 lb/sec
THRUST	1 lb
O/F RATIO	1.65

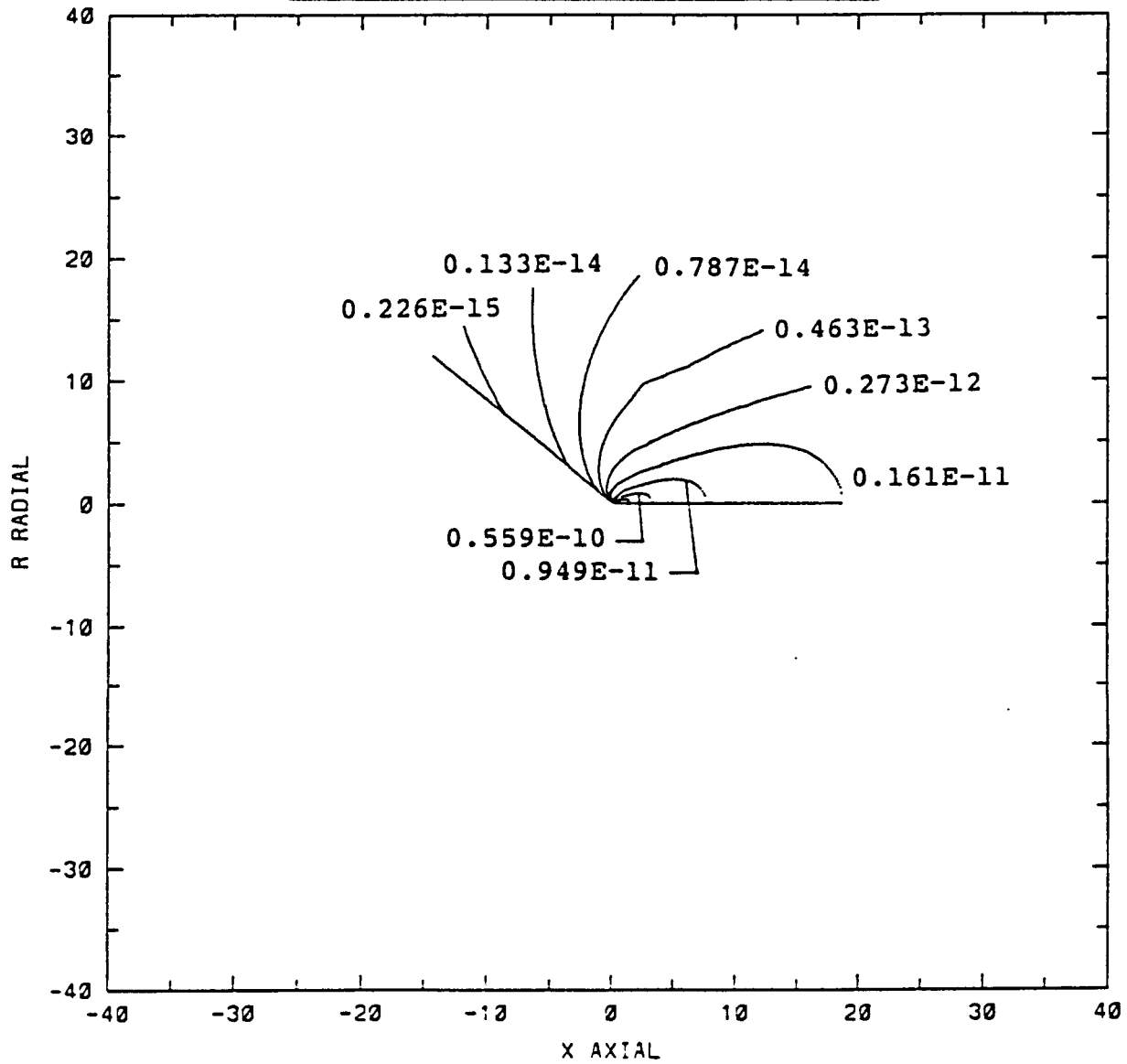


Figure 39: Density Contours: Marquart R2 (11 lbf Thrust)

R6C (A/A* = 150; 5 lbf thrust)	
THROAT RADIUS	0.0075833 ft
EXIT RADIUS	0.09287 ft
AREA RATIO	150
NOZZLE LENGTH	0.27475 ft
CHAMBER PRESSURE	125 psia
AMBIENT PRESSURE	7.548E-09 psia
PROPELLANT	
Fuel	Monomethylhydrazine (MMH)
Oxidizer	N ₂ O ₄ (Nitrogen Tetroxide)
MASS FLOW RATE	0.018329 lb/sec
THRUST	5 lb
O/F RATIO	1.6

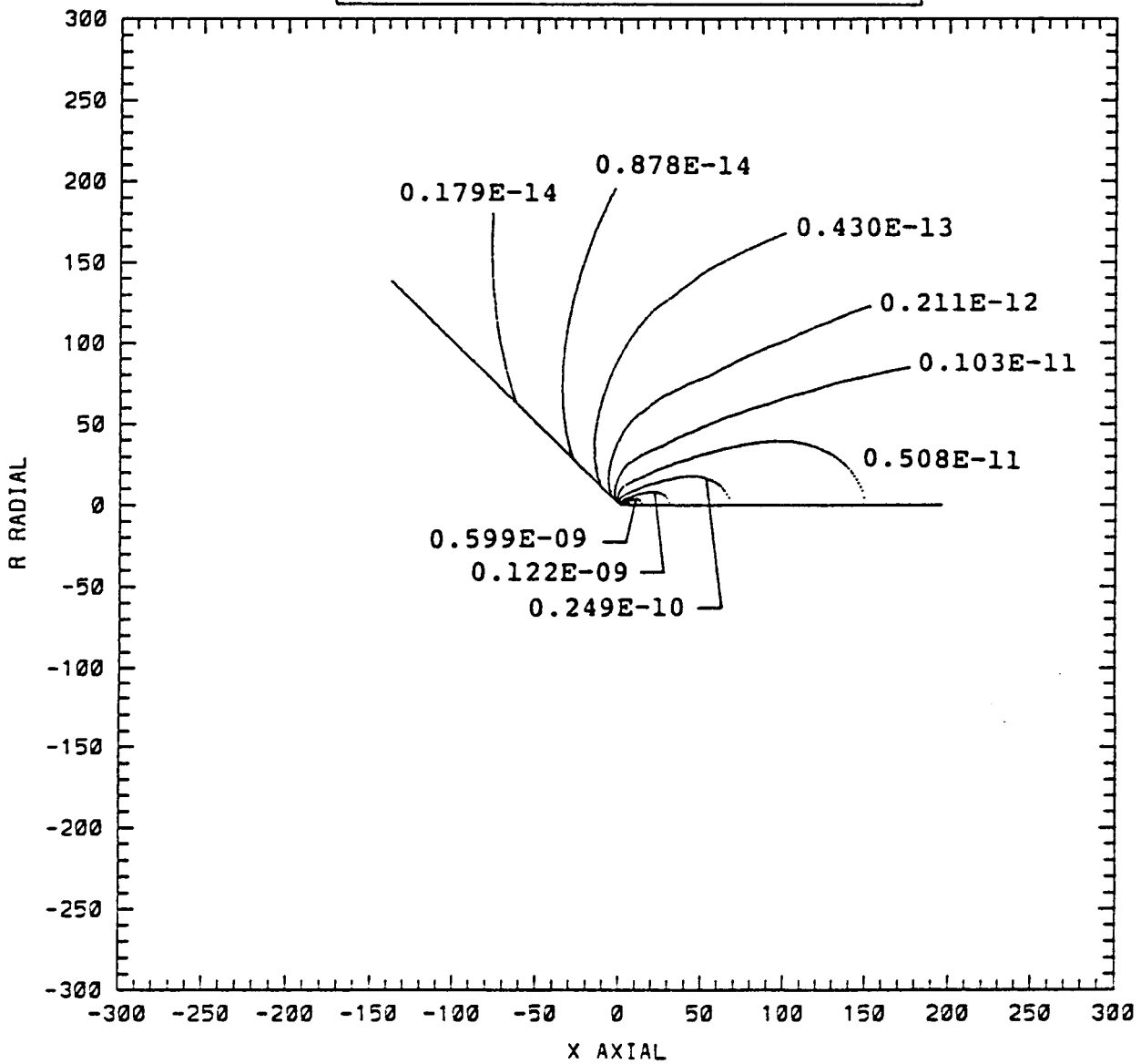


Figure 40: Density Contours: R6C (A/A* = 150; 5 lbf Thrust)

SPACE STATION ACS ENGINE	
THROAT RADIUS	0.02083333 ft
EXIT RADIUS	0.2946 ft
AREA RATIO	199
NOZZLE LENGTH	1.056 ft
CHAMBER PRESSURE	75 psia
AMBIENT PRESSURE	1.3888E-08 psia
PROPELLANT	
Fuel	Hydrogen (H ₂)
Oxidizer	Oxygen (O ₂)
MASS FLOW RATE	0.06798 lb/sec
THRUST	25 lb
O/F RATIO	8

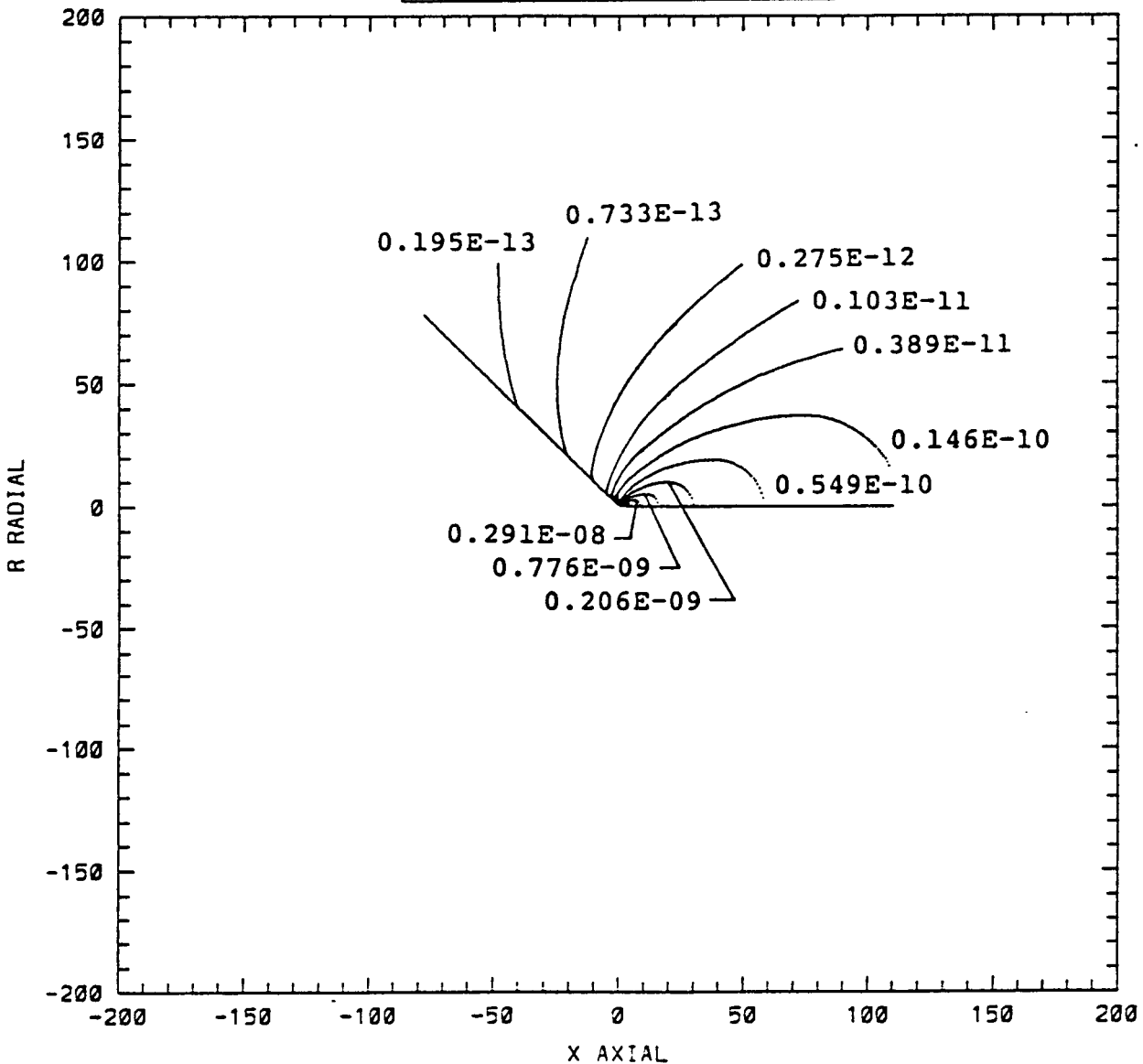


Figure 41: Density Contours: Space Station ACS Engine

NUCLEAR ENGINE (Solid Cone; $A/A^* = 200$, 70,000 lbf Thrust)	
THROAT RADIUS	0.436135 ft
EXIT RADIUS	6.1678 ft
AREA RATIO	200
NOZZLE LENGTH	21.45 ft
CHAMBER PRESSURE	440 psia
AMBIENT PRESSURE	$1.368E-09$ psia
PROPELLANT	Hydrogen (H/H_2)
MASS FLOW RATE	68.746 lb/sec
THRUST	70000 lb
O/F RATIO	0.0

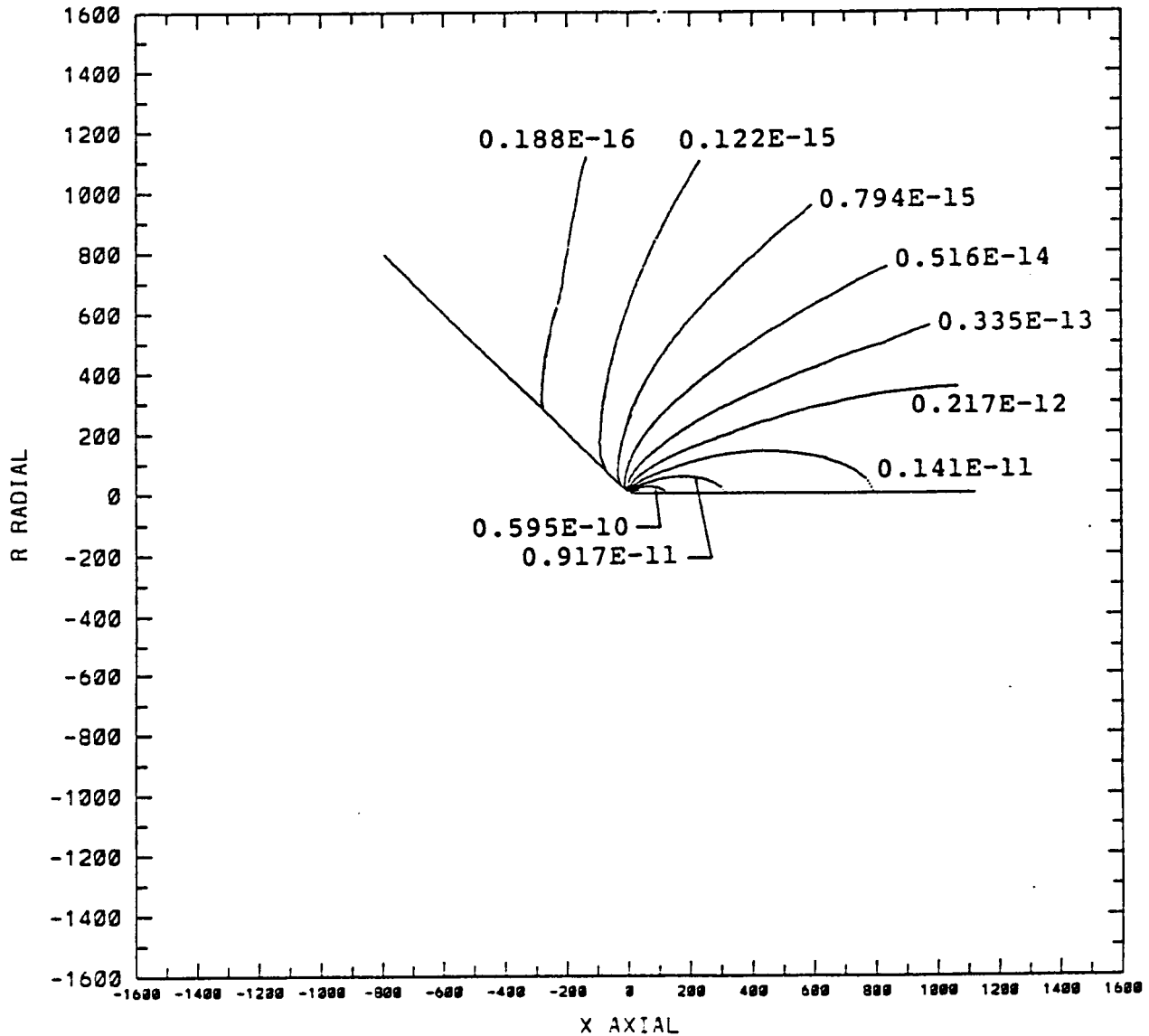


Figure 42: Density Contours: Nuclear Engine (Solid Cone; $A/A^* = 200$; 70,000 lbf Thrust)

MONOS (A/A* = 41, 0.5 Newton)	
THROAT RADIUS	0.00098425 ft
EXIT RADIUS	0.0063083 ft
AREA RATIO	40.1
NOZZLE LENGTH	0.02546ft
CHAMBER PRESSURE	227.7 psia
CHAMBER TEMPERATURE	1350 K
AMBIENT PRESSURE	1.388E-08 psia
PROPELLANT	Hydrazine (N ₂ H ₄)
MASS FLOW RATE	0.0007585 lb/sec
THRUST	0.5 N

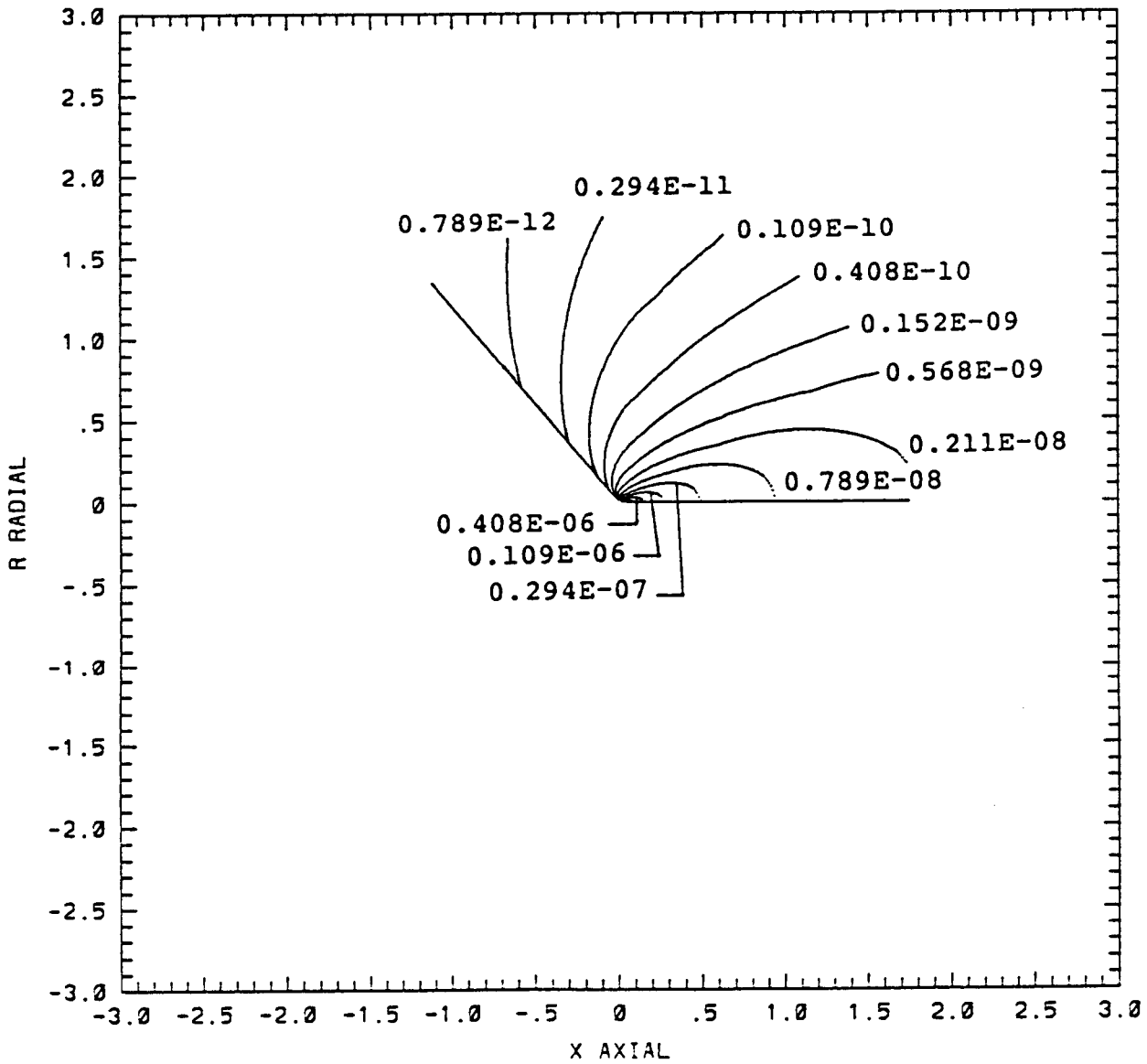


Figure 43: Density Contours: 0.5 Newton Hydrazine Engine (A/A* = 41)

FONG1 (A/A* = 50, 1 lbf Thrust)	
THROAT RADIUS	0.002604 ft
EXIT RADIUS	0.016328 ft
AREA RATIO	50
NOZZLE LENGTH	0.04228 ft
CHAMBER PRESSURE	172.8 psia
AMBIENT PRESSURE	6.944E-08 psia
PROPELLANT	Hydrazine (N ₂ H ₄)
MASS FLOW RATE	0.003738 lb/sec
THRUST	1 lb

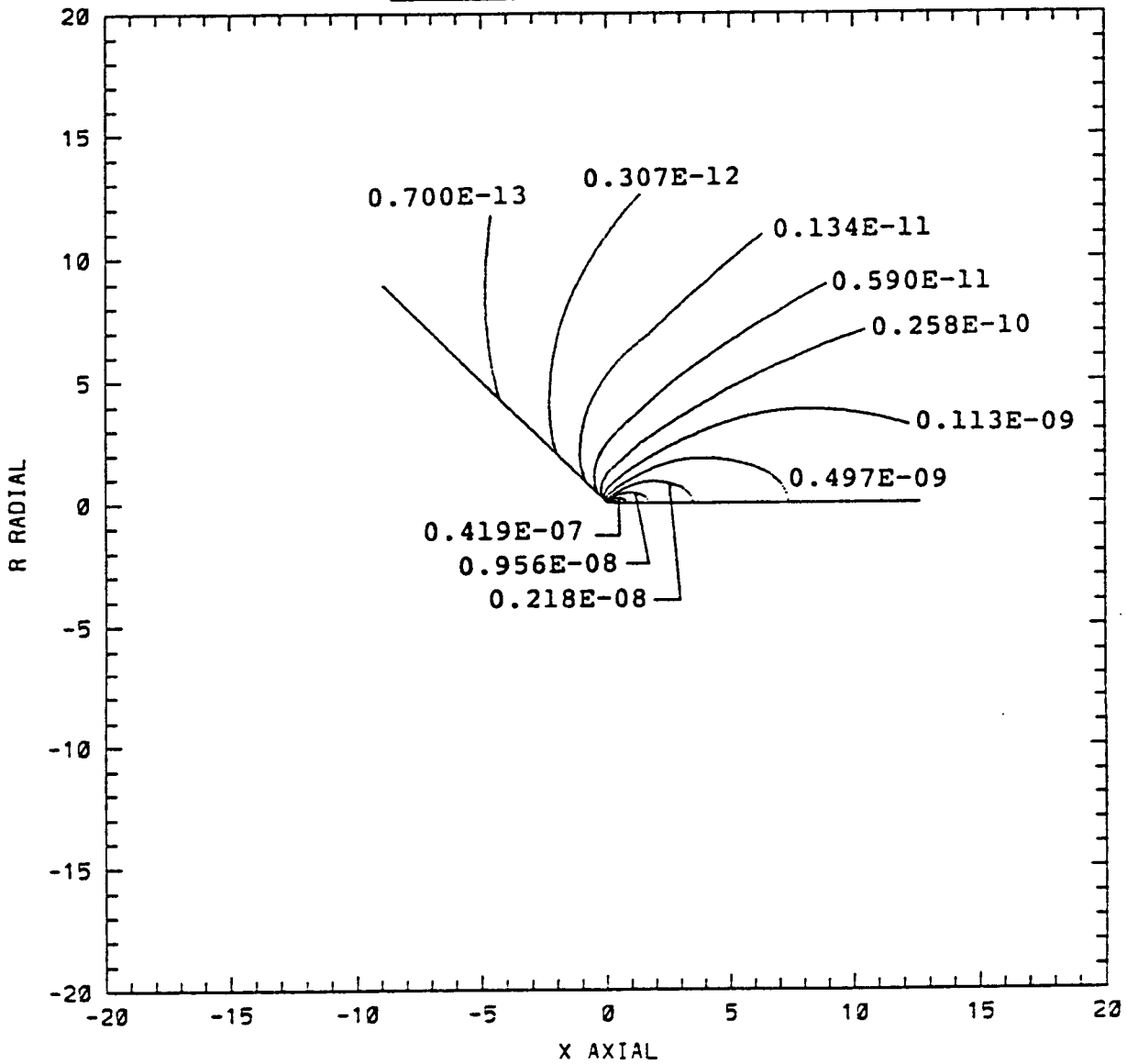


Figure 44: Density Contours: 1 lbf Thrust Hydrazine Engine (A/A* = 50)

MONO3B (REA-MONO-A) ($A/A^* = 79$, 30 lbf Thrust)	
THROAT RADIUS	0.01525 ft
EXIT RADIUS	0.13592 ft
AREA RATIO	79
NOZZLE LENGTH	0.3615 ft
CHAMBER PRESSURE	133 psia
AMBIENT PRESSURE	6.94E-09 psia
PROPELLANT	Hydrazine ($N_2 H_4$)
MASS FLOW RATE	0.10394 lb/sec
THRUST	30 lb

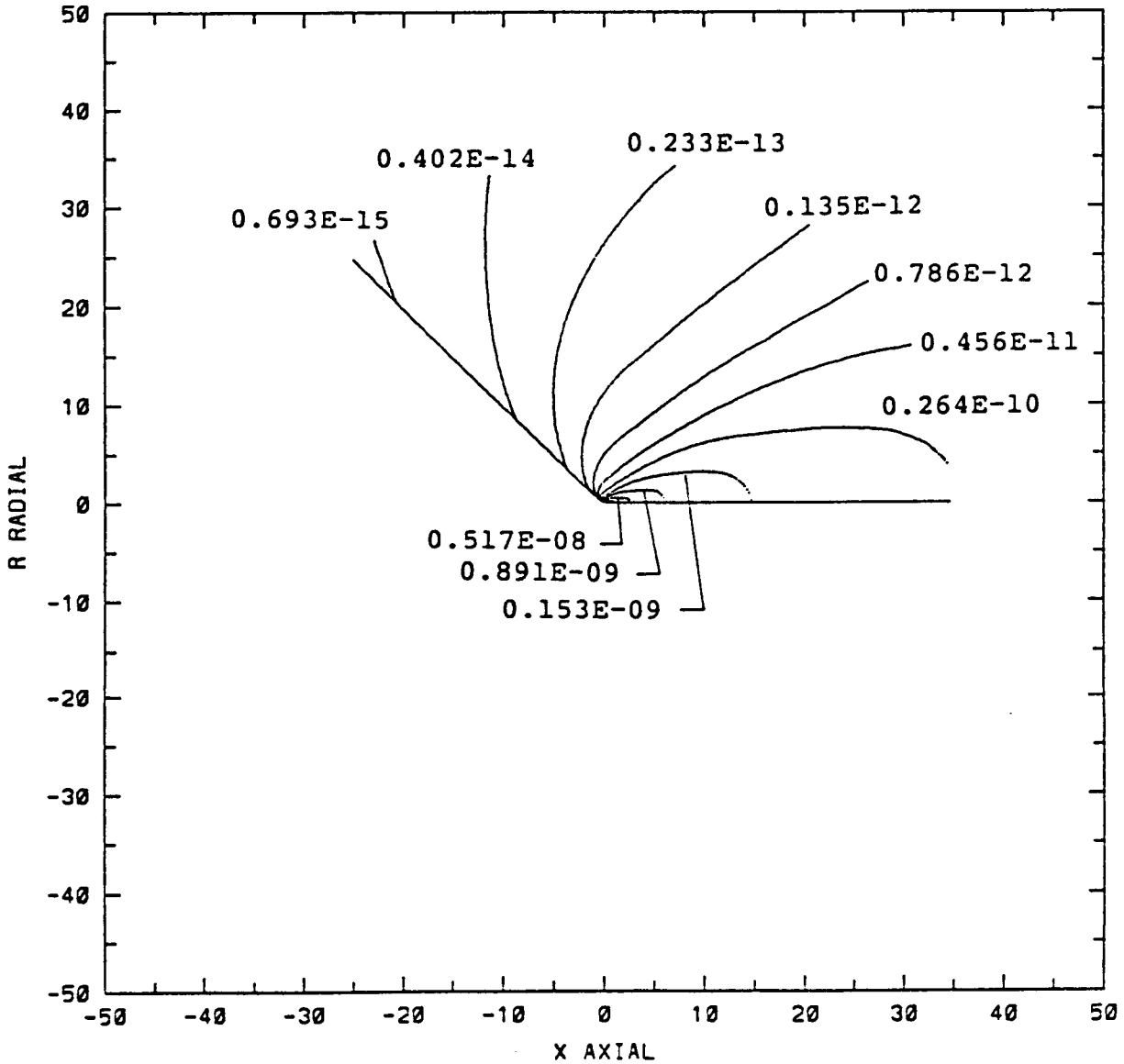


Figure 45: Density Contours: REA-MONO-A (30 lbf Thrust; $A/A^* = 79$)

MRE15 (OMV RCS) ($A/A^* = 50$)	
THROAT RADIUS	0.01233 ft
EXIT RADIUS	0.0872 ft
AREA RATIO	50
NOZZLE LENGTH	0.2212 ft
CHAMBER PRESSURE	134.7 psia
AMBIENT PRESSURE	2.08E-08 psia
PROPELLANT	Hydrazine ($N_2 H_4$)
MASS FLOW RATE	0.06559 lb/sec

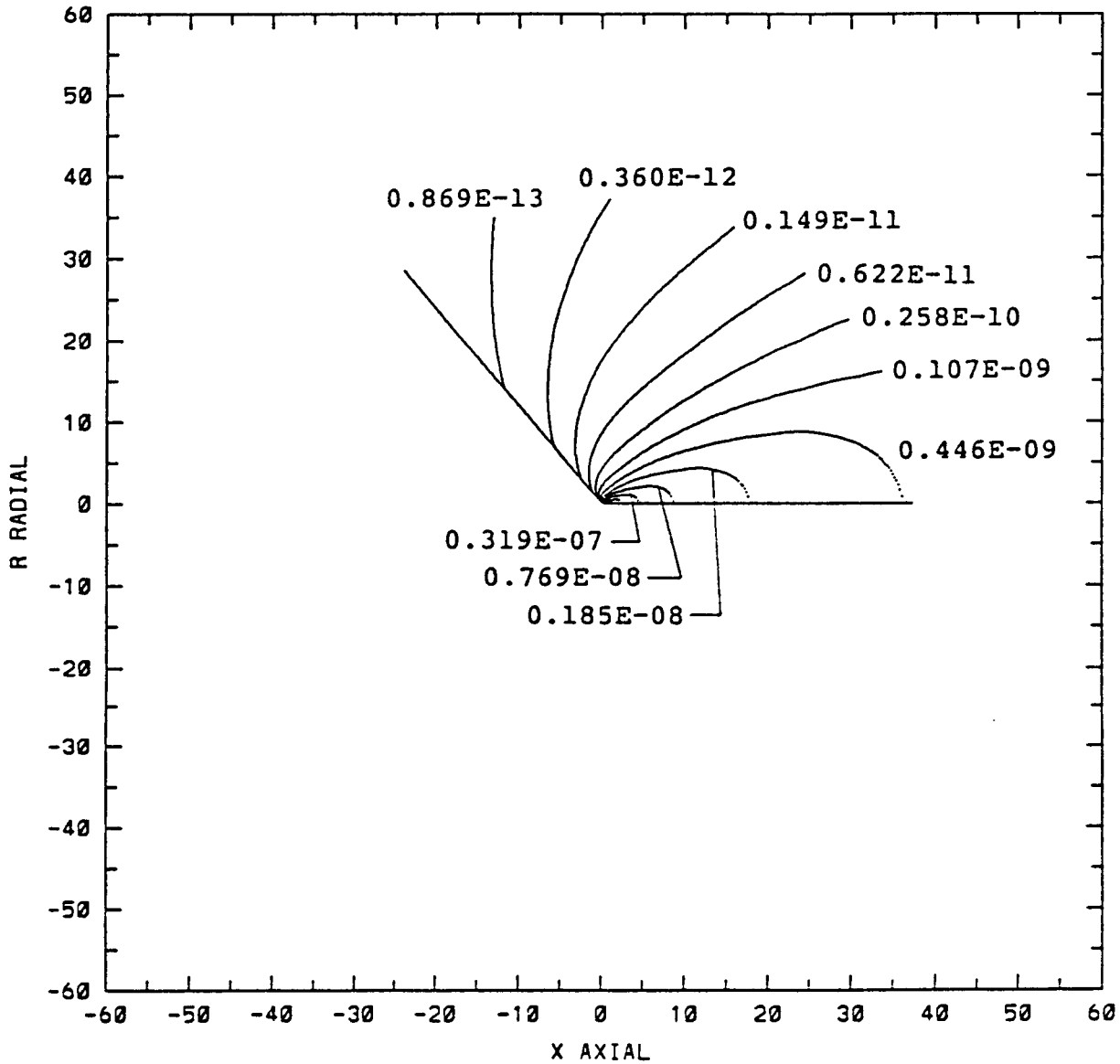


Figure 46: Density Contours: MRE15 (OMV RCS) ($A/A^* = 50$)

AFE RCS30 (AFE 30 lbf RCS)	
THROAT RADIUS	0.01554 ft
EXIT RADIUS	0.094815 ft
AREA RATIO	37
NOZZLE LENGTH	0.2381 ft
CHAMBER PRESSURE	160 psia
AMBIENT PRESSURE	1.388E-08 psia
PROPELLANT	Hydrazine (N ₂ H ₄)
MASS FLOW RATE	0.13098 lb/sec
THRUST	30 lb

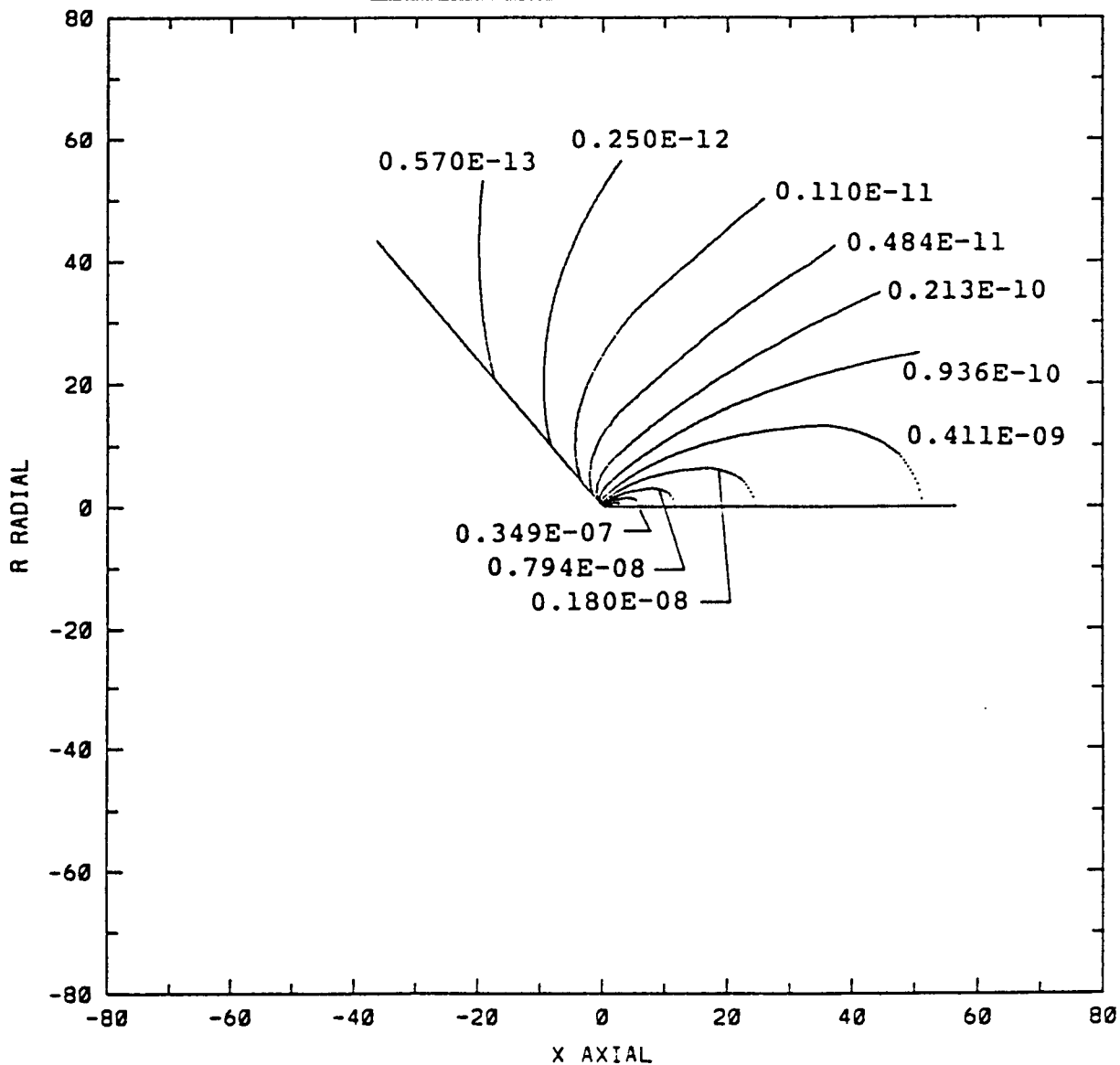


Figure 47: Density Contours: AFE RCS 30 lbf

MOD2 (Hydrazine Engine; A/A* = 50)	
THROAT RADIUS	0.0083333 ft
EXIT RADIUS	0.058915 ft
AREA RATIO	50
NOZZLE LENGTH	0.148825 ft
CHAMBER PRESSURE	135 psia
AMBIENT PRESSURE	6.944E-08 psia
PROPELLANT	Hydrazine (N ₂ H ₄)
MASS FLOW RATE	0.031845 lb/sec
THRUST	7.49 lb

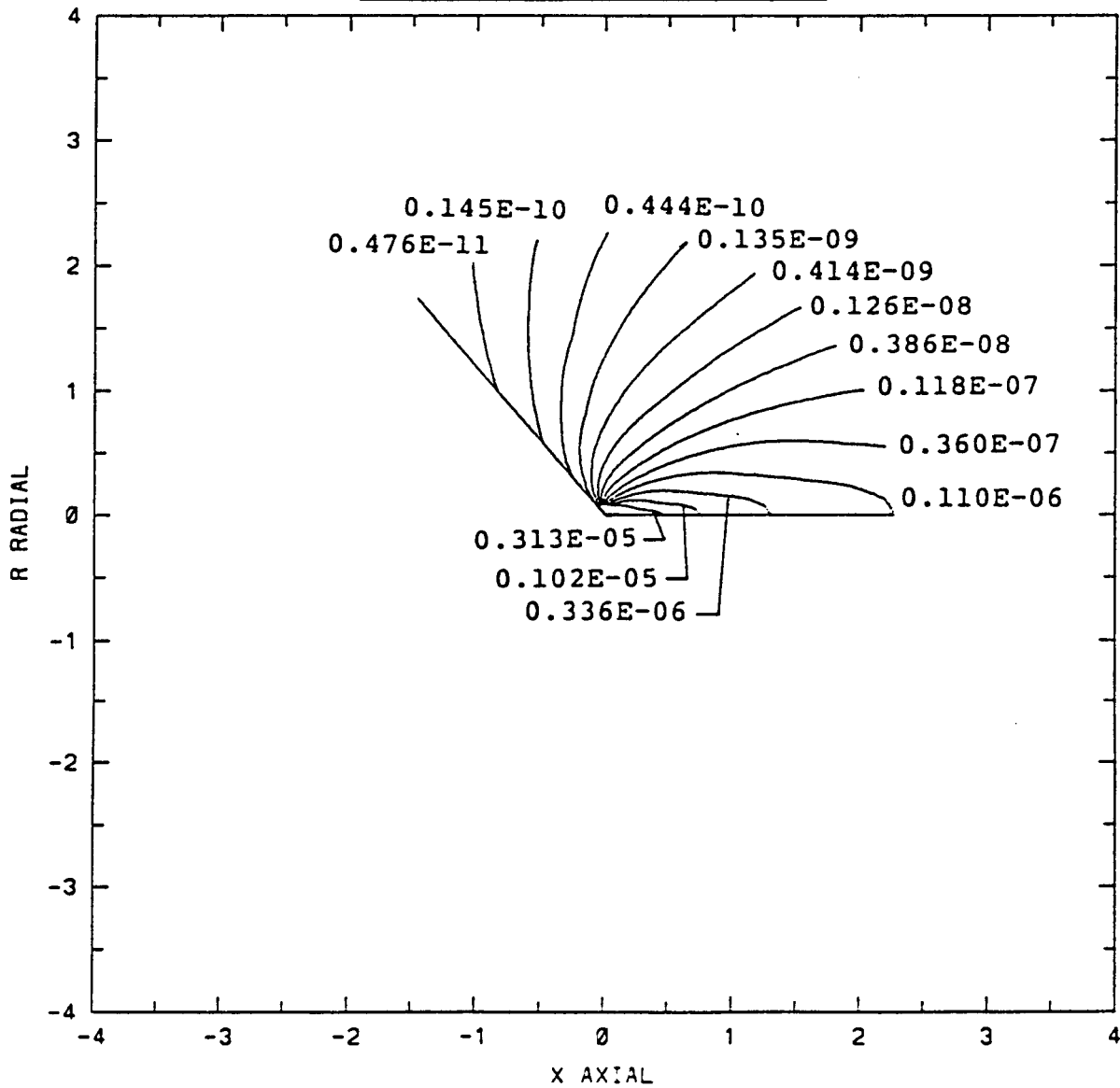


Figure 48: Density Contours: 7.49 lbf Hydrazine Engine (A/A* = 50)

REA 15 (REA15; A/A* = 50)	
THROAT RADIUS	0.03383 ft
EXIT RADIUS	0.2391172 ft
AREA RATIO	50
NOZZLE LENGTH	0.60417 ft
CHAMBER PRESSURE	180 psia
AMBIENT PRESSURE	6.944E-08 psia
PROPELLANT	Hydrazine (N ₂ H ₄)
MASS FLOW RATE	0.699767 lb/sec
THRUST	164.4 lb

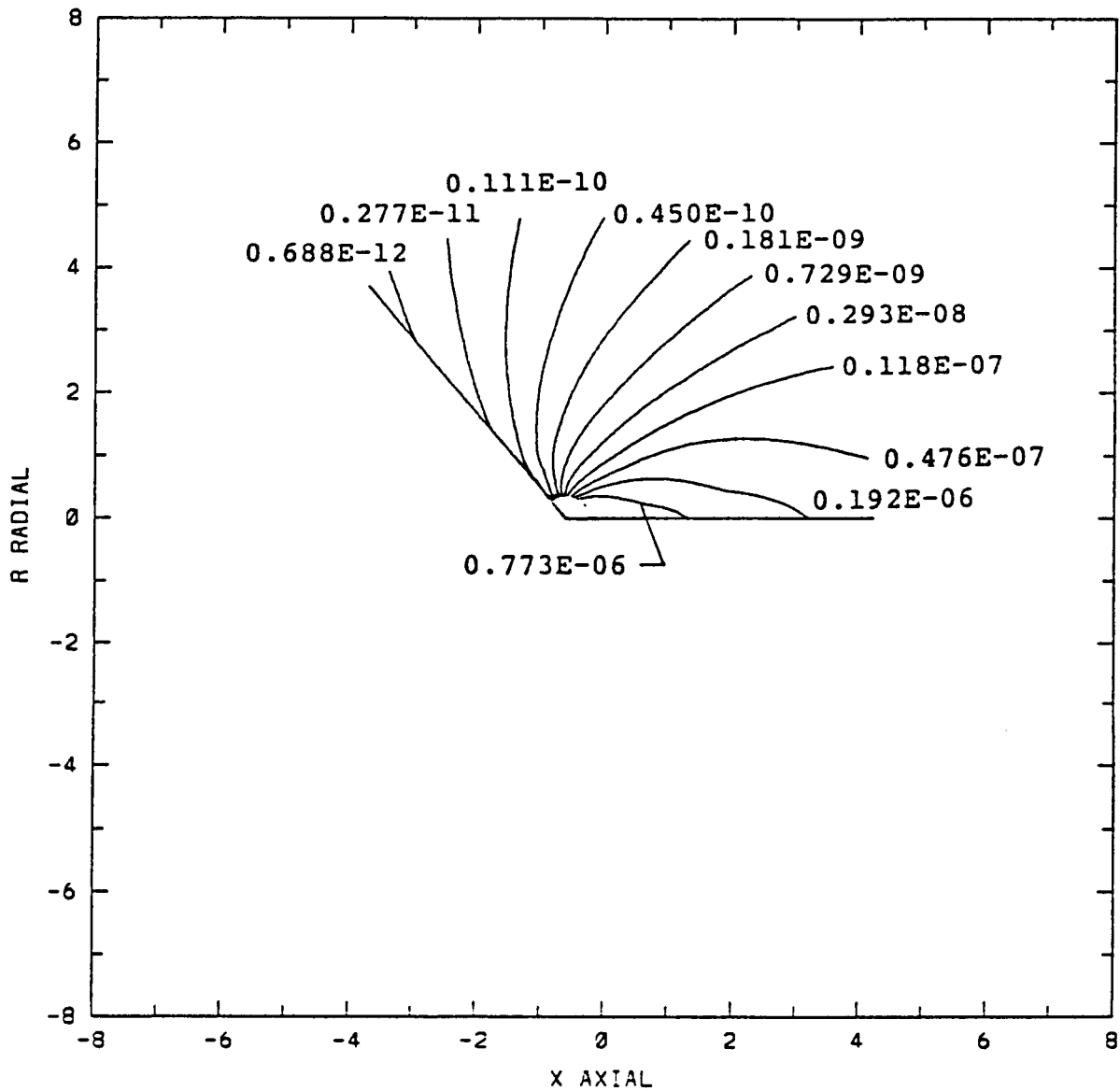


Figure 49: Density Contours: REA 15 (A/A* = 50)

AFE GASEOUS HELIUM THRUSTER	
THROAT RADIUS	0.003125 ft
EXIT RADIUS	0.01975 ft
AREA RATIO	40
NOZZLE LENGTH	0.07831 ft
CHAMBER PRESSURE	150 psia
AMBIENT PRESSURE	6.944E-09 psia
PROPELLANT	Helium (H_e)
MASS FLOW RATE	0.0060335 lb/sec
THRUST	1.05 lb

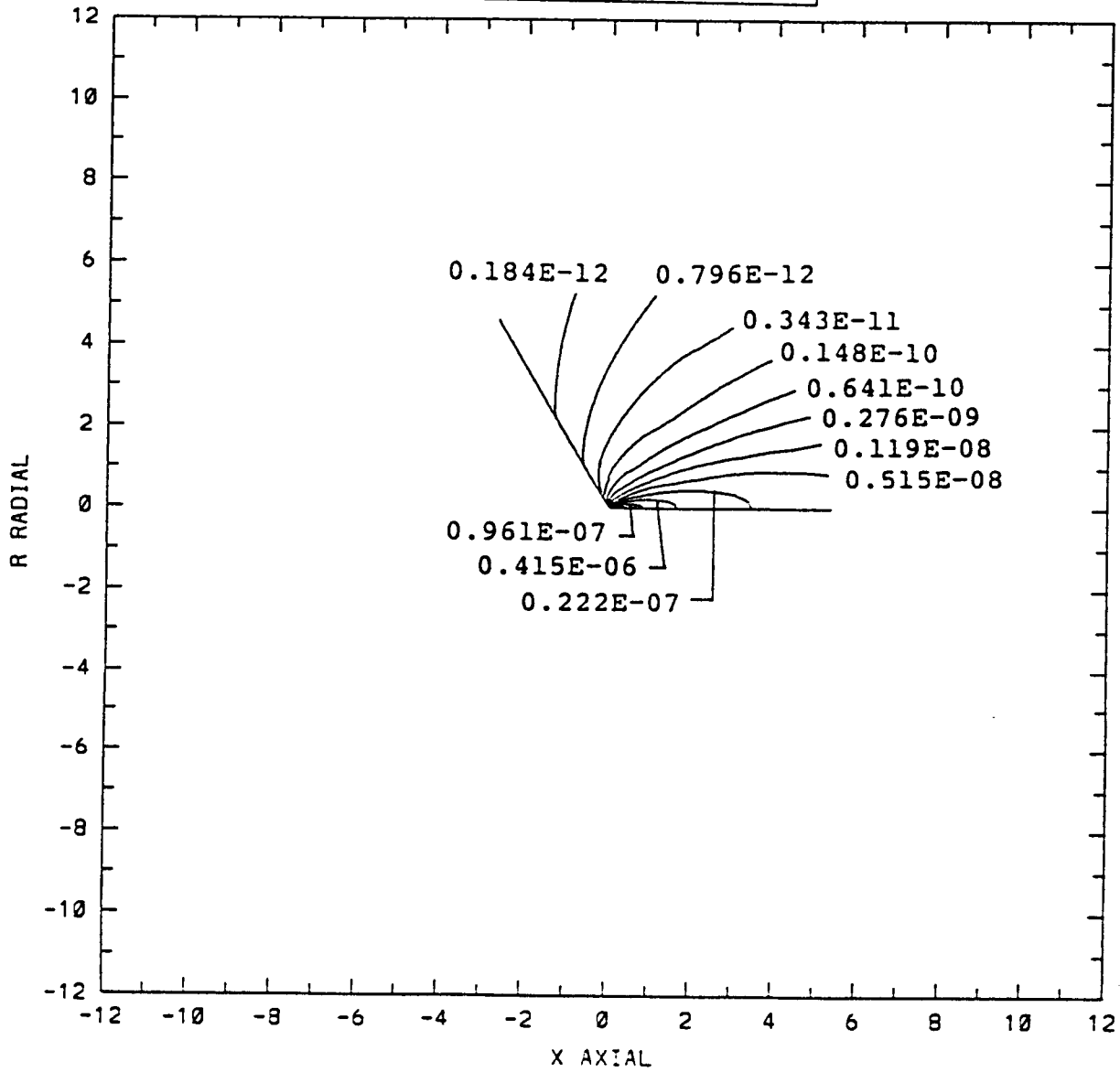


Figure 50: Density Contours: AFE Gaseous Helium Thruster

OMV NITROGEN THRUSTER	
THROAT RADIUS	0.010416 ft
EXIT RADIUS	0.032917 ft
AREA RATIO	10
NOZZLE LENGTH	0.08794 ft
CHAMBER PRESSURE	63 psia
AMBIENT PRESSURE	294 K
PROPELLANT	Nitrogen (N ₂)
MASS FLOW RATE	0.067327 lb/sec
THRUST	4.77 lb

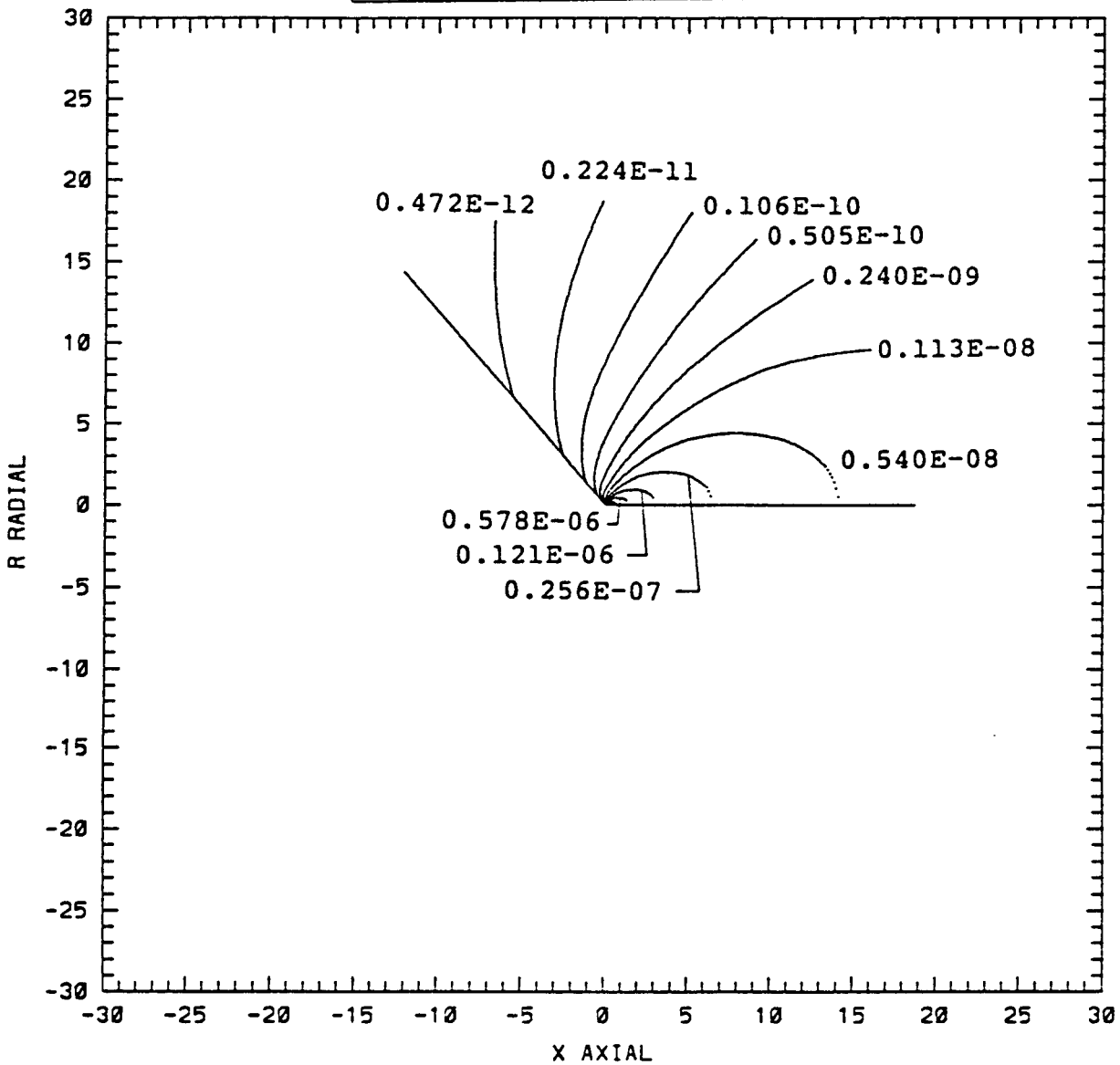


Figure 51: Density Contours: OMV Nitrogen Thruster

AEDC CO2 SONIC ORIFICE	
THROAT RADIUS	0.02475 ft
EXIT RADIUS	0.02475 ft
AREA RATIO	1
NOZZLE LENGTH	0.025 psia
CHAMBER PRESSURE	270 K
AMBIENT PRESSURE	1.875E-10 psia
PROPELLANT	Carbon Dioxide (CO ₂)
MASS FLOW RATE	0.000207 lb/sec
THRUST	0.008 lb

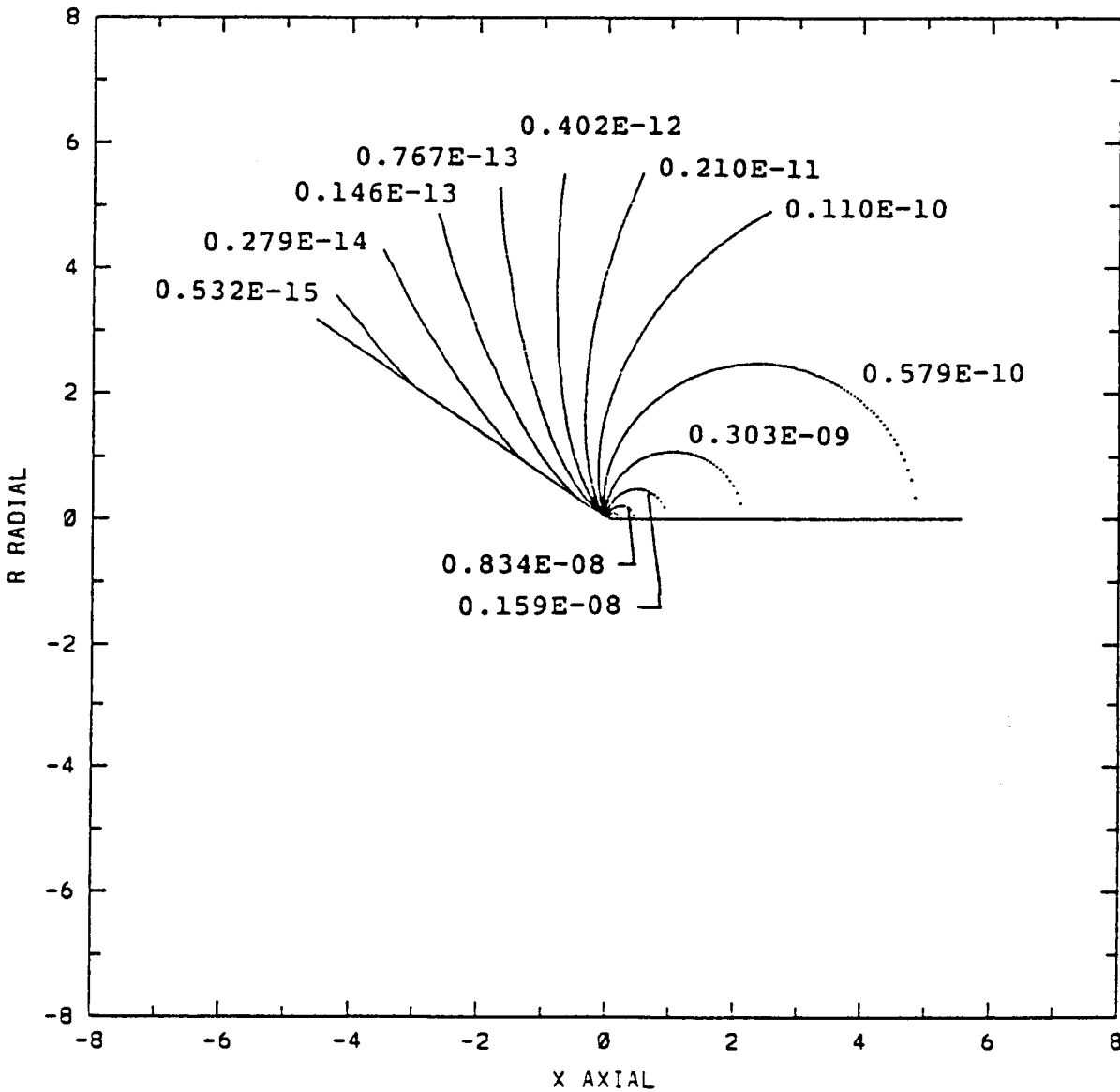


Figure 52: Density Contours: AEDC CO2 Sonic Orifice

EVASON4 - EVA Free Sonic Vent (4" Dia.)	
THROAT RADIUS	0.166667 ft
EXIT RADIUS	0.166667 ft
AREA RATIO	1
NOZZLE LENGTH	1.469 psia
CHAMBER PRESSURE	155 K
AMBIENT PRESSURE	6.94E-08 psia
PROPELLANT	Air
MASS FLOW RATE	0.5859 lb/sec
THRUST	23.4 lb

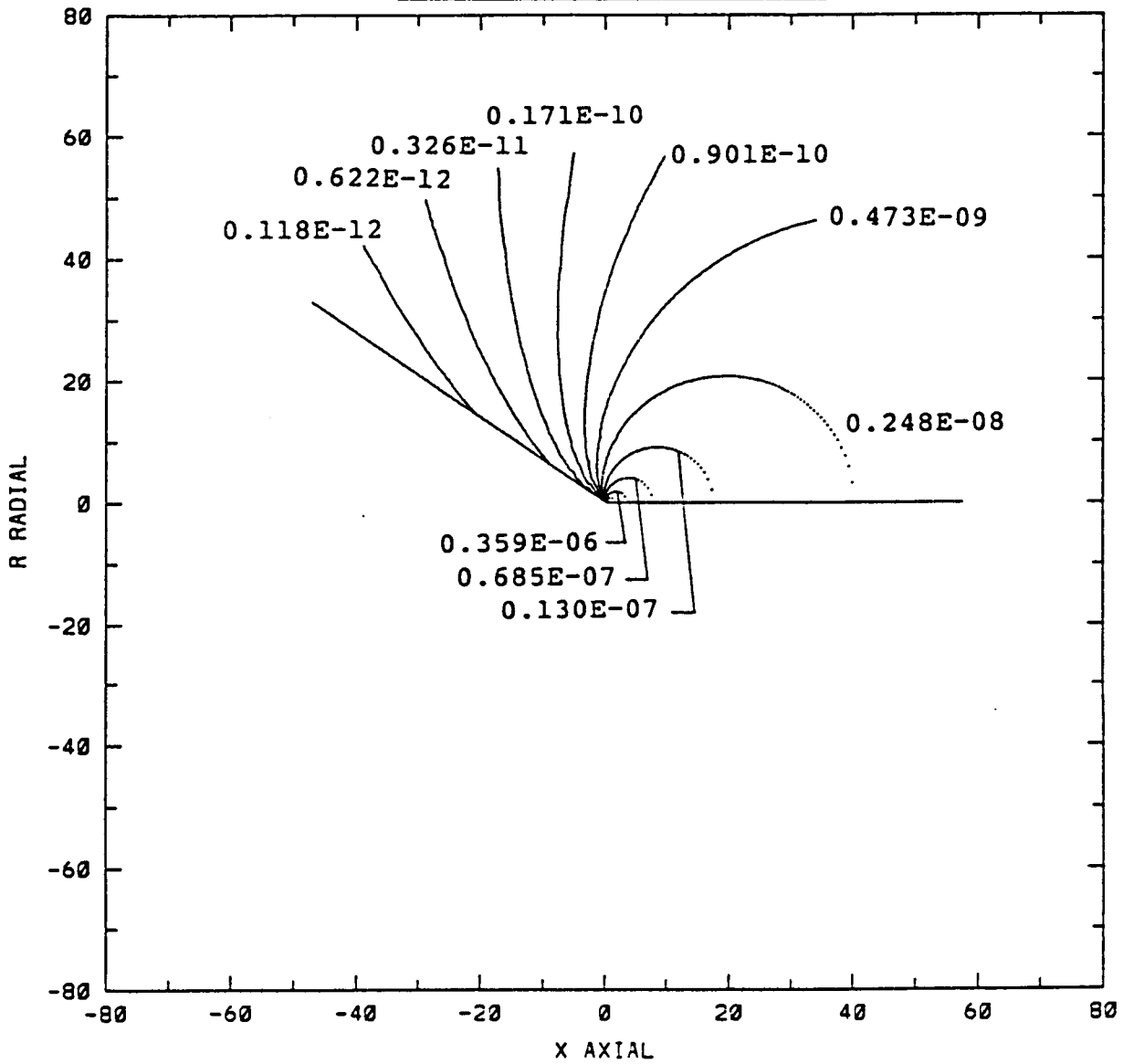


Figure 53: Density Contours: Space Station EVA Free Air Sonic Vent (4 In. Diameter)

EVAST1 - Space Station EVA - 1" Stringer Vent	
THROAT RADIUS	0.041667 ft
EXIT RADIUS	0.041667 ft
AREA RATIO	1
NOZZLE LENGTH	0.03788 psia
CHAMBER PRESSURE	244 K
AMBIENT PRESSURE	2.0E-10 psia
PROPELLANT	Air
MASS FLOW RATE	0.0007526 lb/sec

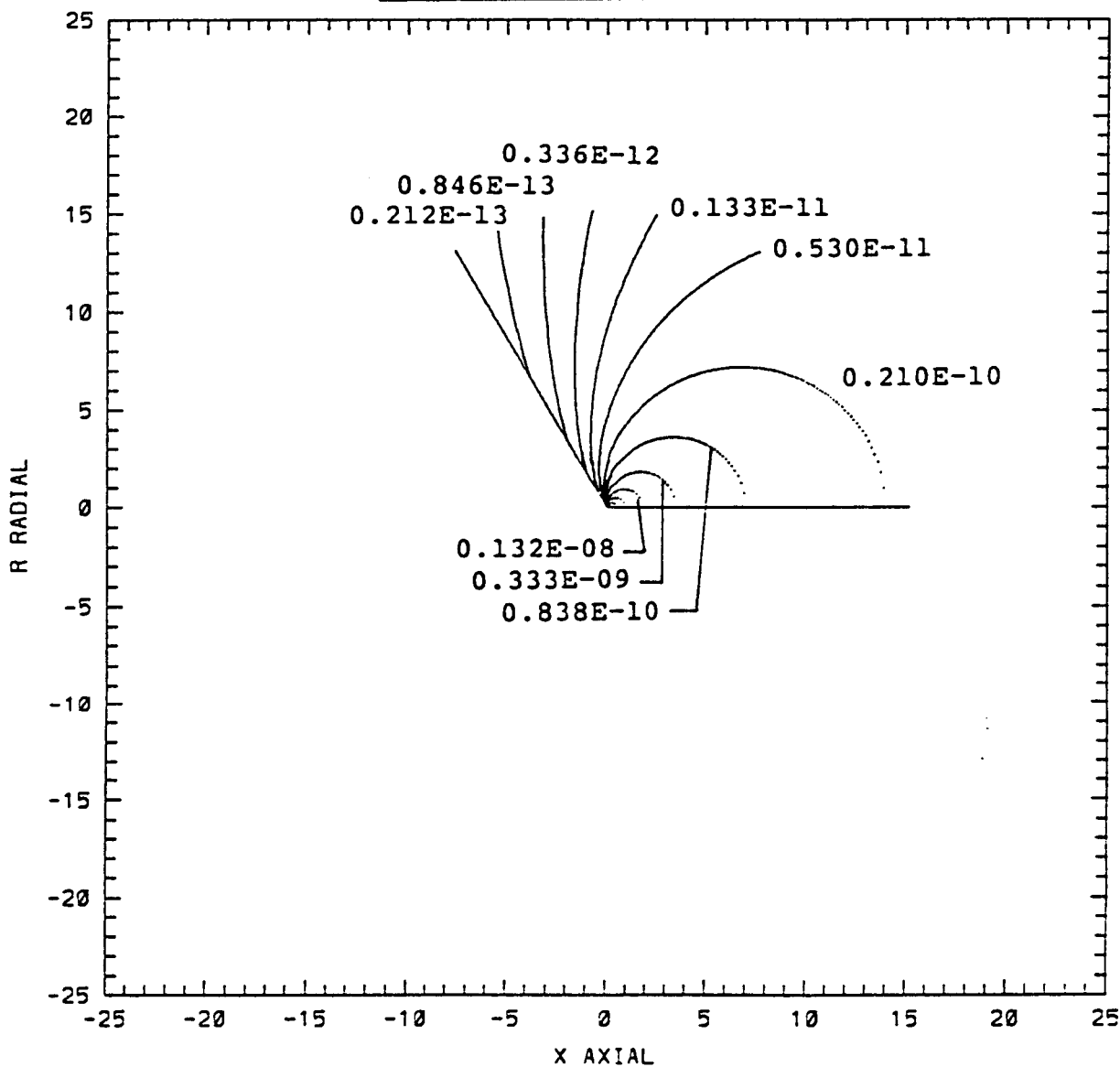


Figure 54: Density Contours: Space Station EVA Stringer Air Vent (1 In. Diameter)

EVA5T1 - Space Station EVA - 4" Stringer Vent	
THROAT RADIUS	0.16667 ft
EXIT RADIUS	0.16667 ft
AREA RATIO	1
NOZZLE LENGTH	0.6416 psia
CHAMBER PRESSURE	244 K
AMBIENT PRESSURE	3.47E-08 psia
PROPELLANT	Air
MASS FLOW RATE	0.2039 lb/sec
THRUST	10.2 lb

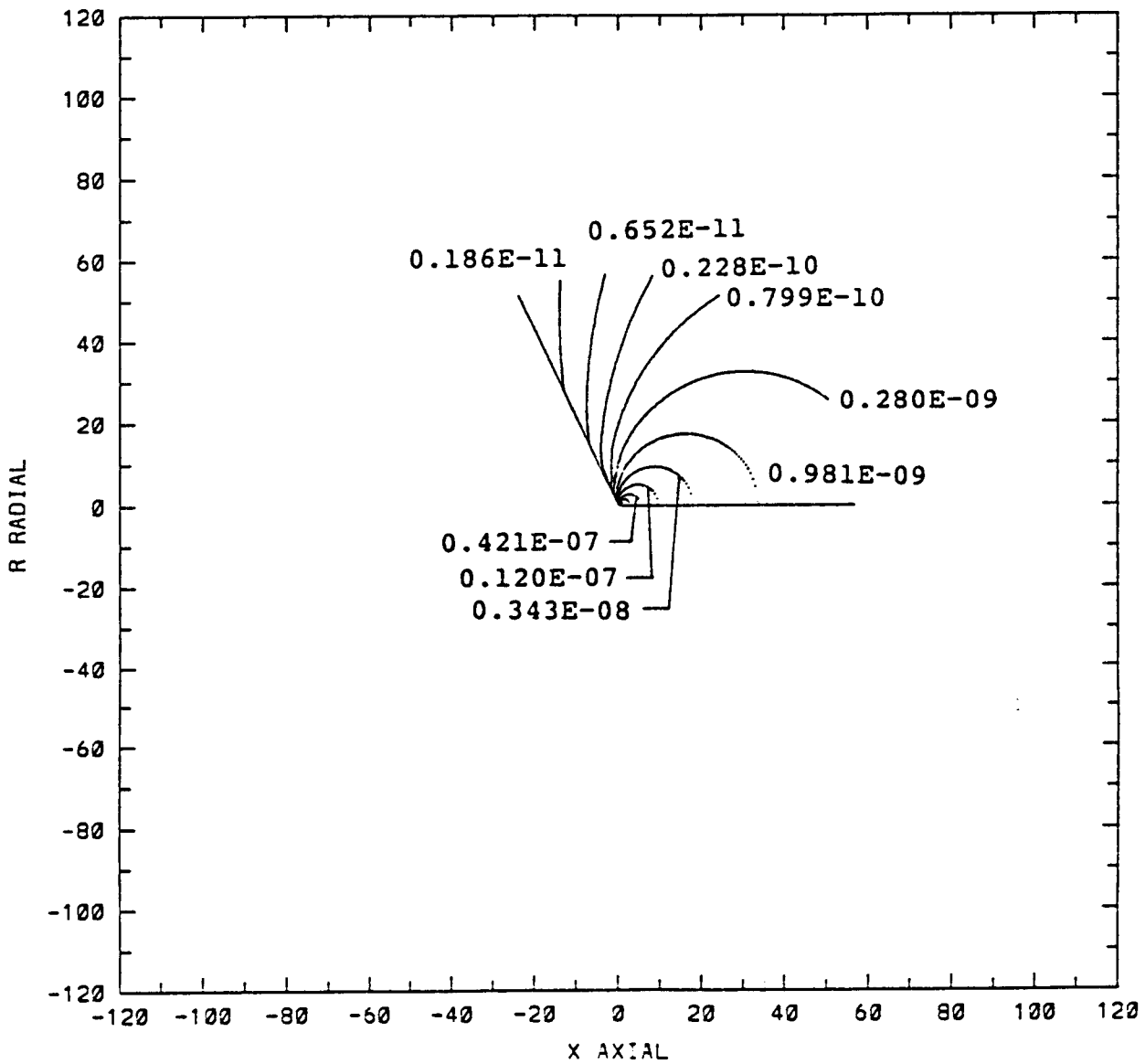


Figure 55: Density Contours: Space Station EVA Stringer Air Vent (4 In. Diameter)

HYPBAR - Space Station Hyperbaric Vent	
THROAT RADIUS	0.0145833 ft
EXIT RADIUS	0.0145833 ft
AREA RATIO	1
NOZZLE LENGTH	85.48 psia
CHAMBER PRESSURE	317 K
AMBIENT PRESSURE	3.47E-06 psia
PROPELLANT	Air
MASS FLOW RATE	0.1826 lb/sec
THRUST	10.4 lb

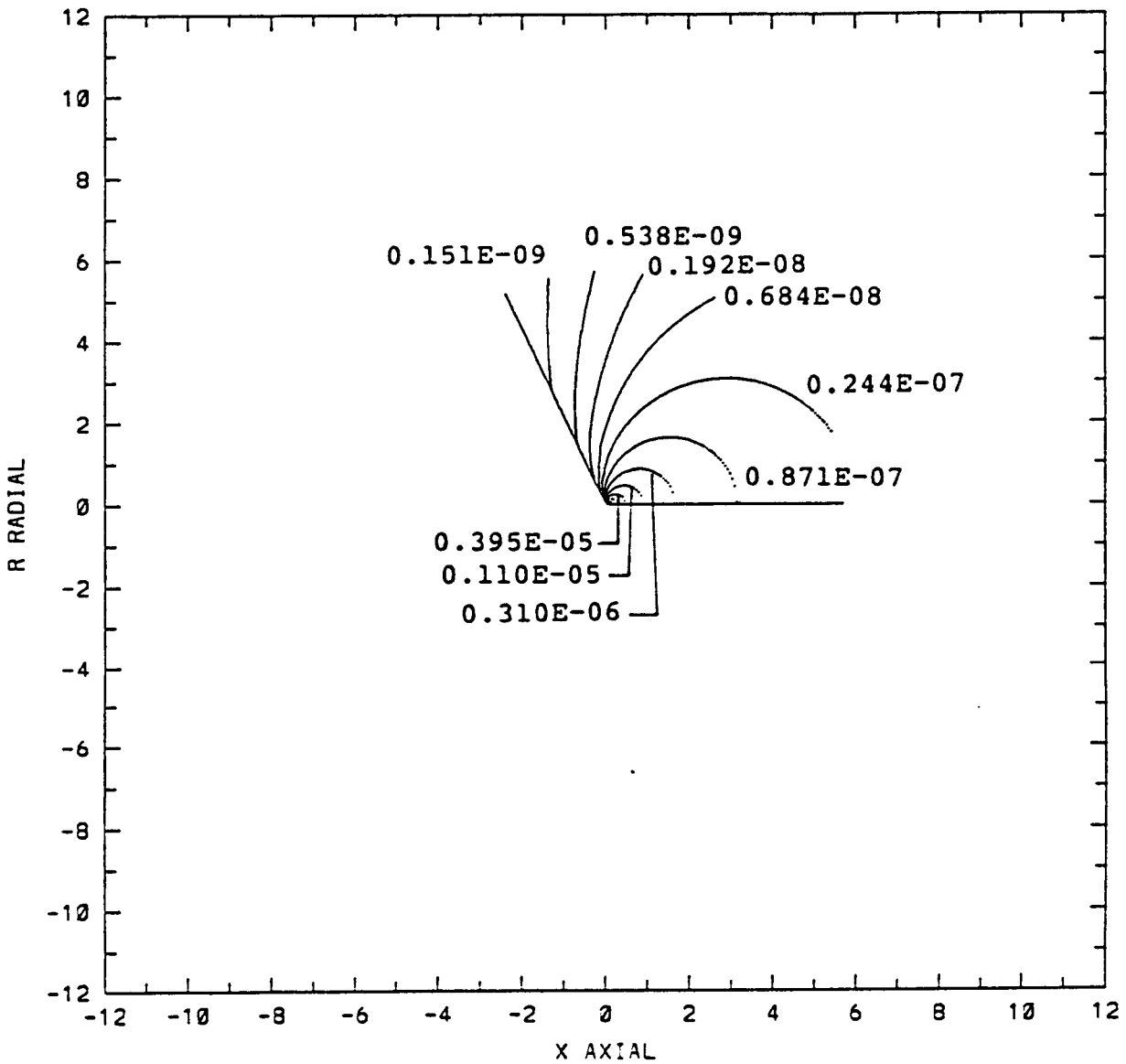


Figure 56: Density Contours: Space Station Hyperbaric Air Vent

JPL GN2 NOZZLE	
THROAT RADIUS	0.008333 ft
EXIT RADIUS	0.032275 ft
AREA RATIO	15
NOZZLE LENGTH	0.05536 ft
CHAMBER PRESSURE	3.2 psia
CHAMBER TEMPERATURE	294 K
AMBIENT PRESSURE	1.04E-08 psia
PROPELLANT	Nitrogen (N ₂)
MASS FLOW RATE	0.002285 lb/sec
THRUST	0.16 lb

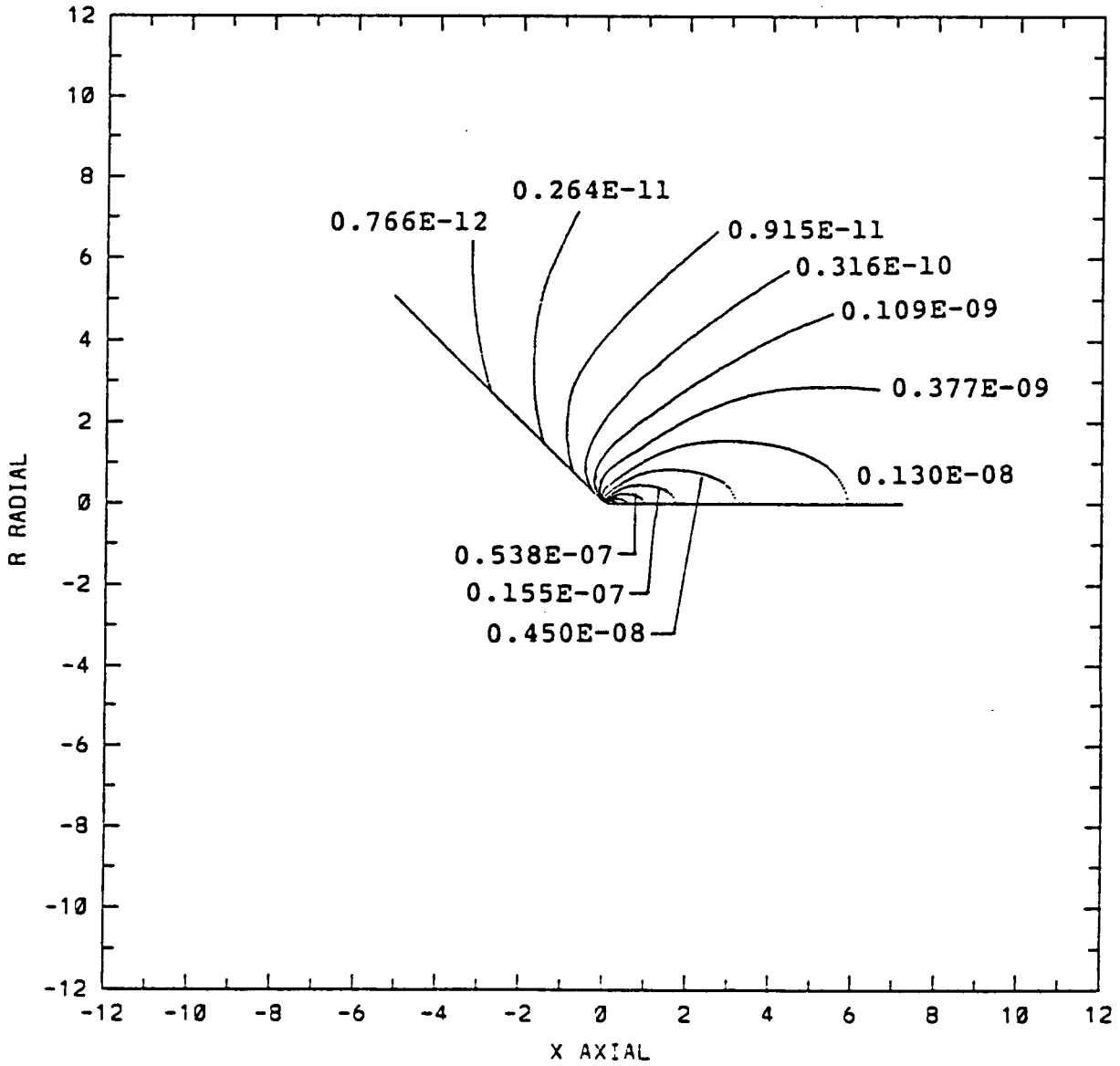


Figure 57: Density Contours: JPL GN2 Nozzle

STAR63 - AFE Injection Motor	
THROAT RADIUS	0.18875 ft
EXIT RADIUS	0.48176 ft
AREA RATIO	6.5
NOZZLE LENGTH	2.1342 ft
CHAMBER PRESSURE	831 psia
AMBIENT PRESSURE	5.55E-08 psia
MASS FLOW RATE	0.0060335 lb/sec
THRUST	24554 lb

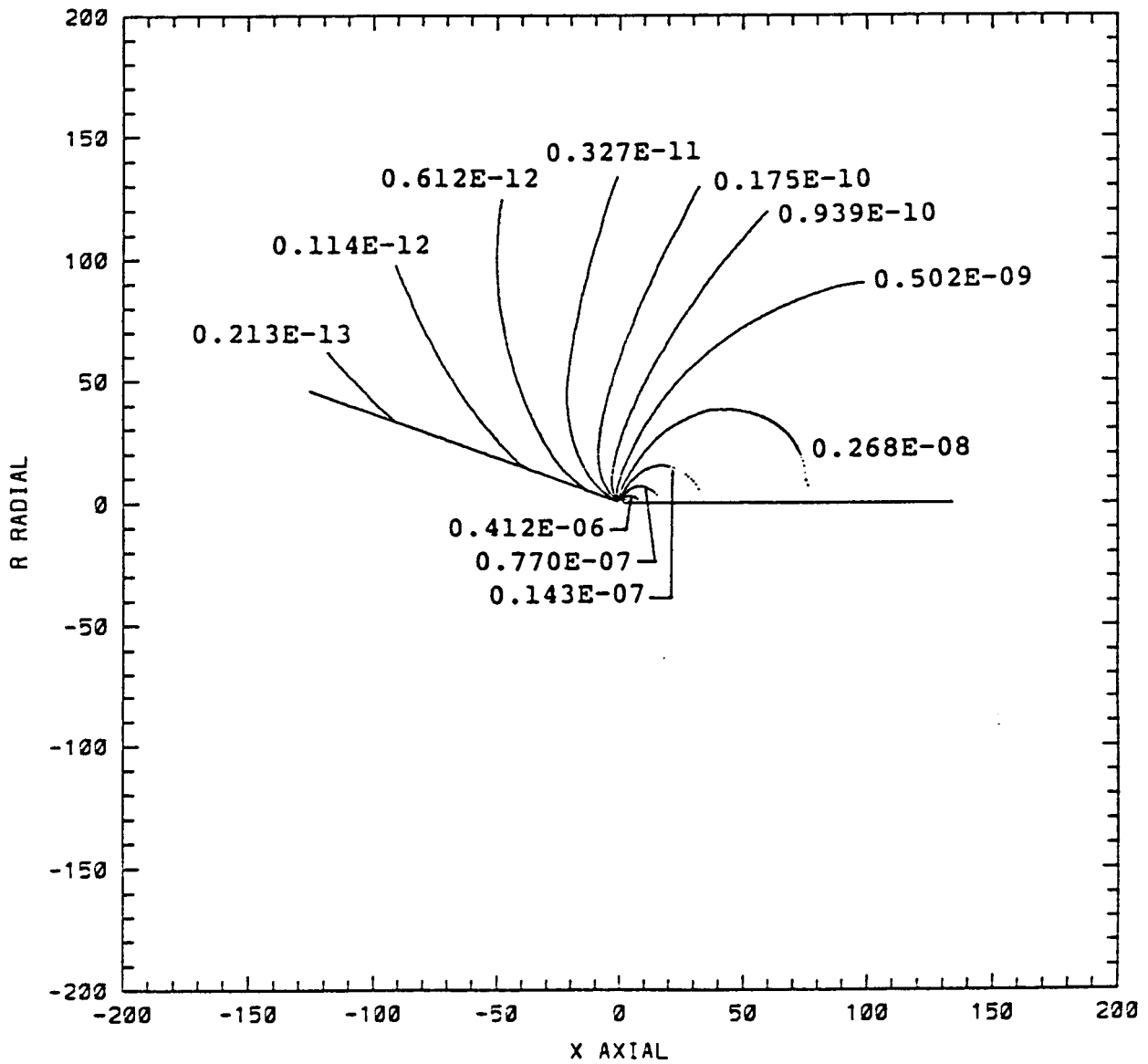


Figure 58: Density Contours: STAR63 (AFE Ignition Motor)

3.5 Sample Problems

Two sample problems were chosen to demonstrate how PLIMP may be used to solve different impingement scenarios. The sample cases are:

1. Impingement on a cylindrical subshape from the Space Shuttle Vernier RCS engine.
2. Impingement on two subshapes (flat plate and cylinder) from the Space Shuttle Primary RCS engine.

These cases are hypothetical but adequately demonstrate the procedures used to solve impingement forces and moments using an SFPGEN generated sourceflow plume flowfield. Case 1 involves impingement of a relatively small plume on a large surface (horizontal cylinder), while sample case 2 represents a large plume striking a small surface (vertical cylinder). It is assumed at this stage that the reader is familiar with the method(s) used to calculate the two flowfields. The PLIMP input files for both cases are shown in Tables 5 and 6.

3.5.1 Sample Case 1

There are many options in setting up the coordinate system in any impingement problem. For simplicity it was assumed that the engine and reference coordinate systems are identically positioned. The Vernier RCS engine was canted 30.0 degrees to fire directly on the impinged body. Therefore a -30.0 degree angle of rotation was used about the z-axis to transform the reference system to the engine coordinate system. The composite body is a cylinder fifty (50) feet in length with a diameter of ten (10) feet. The origin of the subshape coordinate system was located by a vector (RCI) from the reference system to the subshape origin. The x-component of the position vector was input as -12.0 , the y-component as -12.0 , and the z-component as 0.0 . Modified Newtonian theory was used to calculate the impingement pressure on the cylindrical body, while the convective heating rates were calculated employing the Yawed Infinite Cylinder theory. Figures 59 and 60 show the surface pressure values on the cylinder.

The engine coordinate system appears as the x-y-z axes located above the subshape. The color bar menu shows the relationship between contour colors and magnitude of the impingement pressure. The pressure is in psia. The plots clearly show the effects of the SFPGEN plume flowfield on the subshape. The underexpanded nature of the plume may be identified by the impinged areas behind the engine.

3.5.2 Sample Case 2

As in Sample Case 1, the engine and reference coordinate systems of Sample Case 2 are identically positioned. The Primary RCS engine was canted 15.0 degrees to fire directly on the composite body. Therefore a -15.0 degree angle of rotation was used about the z-axis. A series of two simple subshapes were coupled together to model the composite structure. The dimensions of the flat plate and conical subshapes (each located with its own local coordinate system) are outlined in the PLIMP input file (Table 6).

Table 5: PLIMP Input File for Sample Case 1

0	0	0	0	2	000	1	1	0	1
SPACE SHUTTLE	VERNIER	RCS	ENGINE	A/A*	= 21				
1	0	3	1	00	10	2	0	1	1 0 0
0.0	0.0		0.0				1	1	123
0.0	0.0		-30.0						
0.	0.		.12		1.		1.	1.	0.
0.1	-04100.	0.0	1.4	1716.	2.				3DHM
540.			2200.	.1333	1.				
50.0	10.0								
10500500051.0	25.0	0.0	0.0	0.0	0.0	0.0	0.0	0.0	50.0
-12.0	-12.0	0.0	123						
0.0	0.0	0.0							
0.0	360.								
100.	-50.	0.0	0.0	1000.	90.				
END									

Modified Newtonian theory was used to calculate the impingement pressure on both subshapes, while the convective heating rates were calculated employing the Eckert Reference Enthalpy method for the flat plate and Yawed Infinite Cylinder theory for the cylinder. Figures 61 and 62 show the surface pressure values on the two subshapes.

The engine coordinate system appears as the x-y-z axes located above the subshape. The plots clearly identify the plume boundary. The shading effects of the cylinder on the flat plate are evident from each plot.

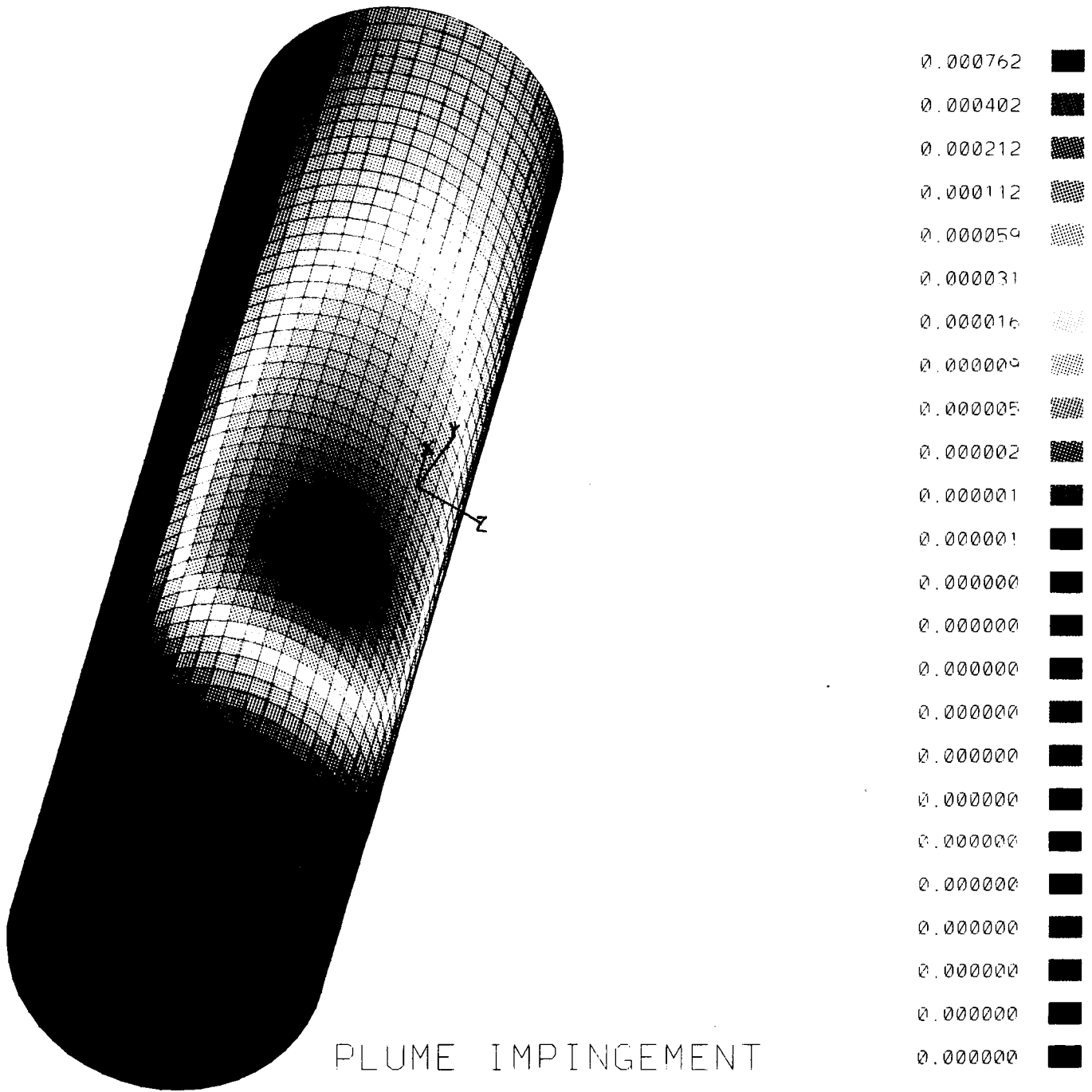


Figure 60: Sample Case 1 — Impingement Pressure (View 2)

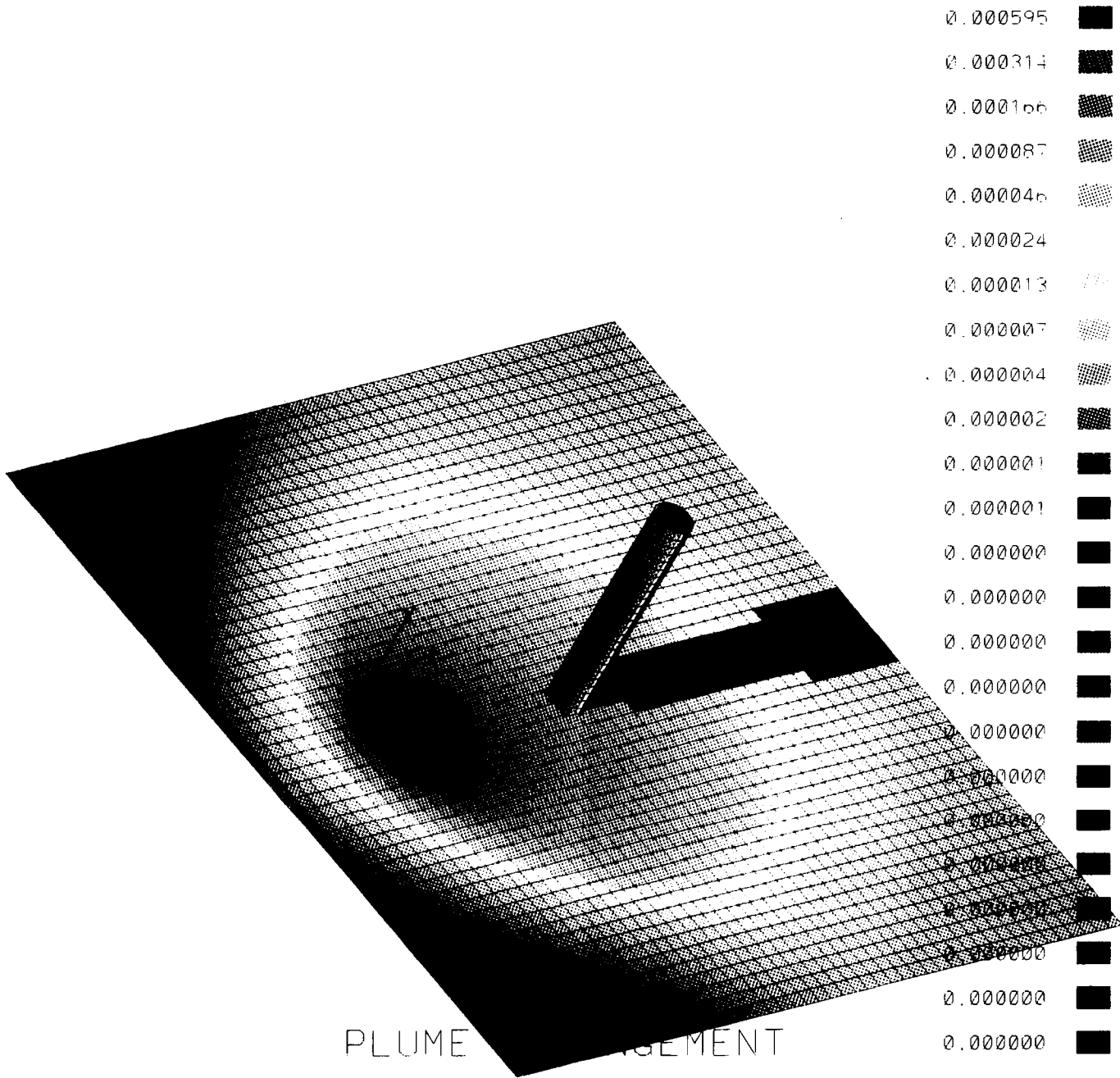


Figure 61: Sample Case 2 — Impingement Pressure (View 1)

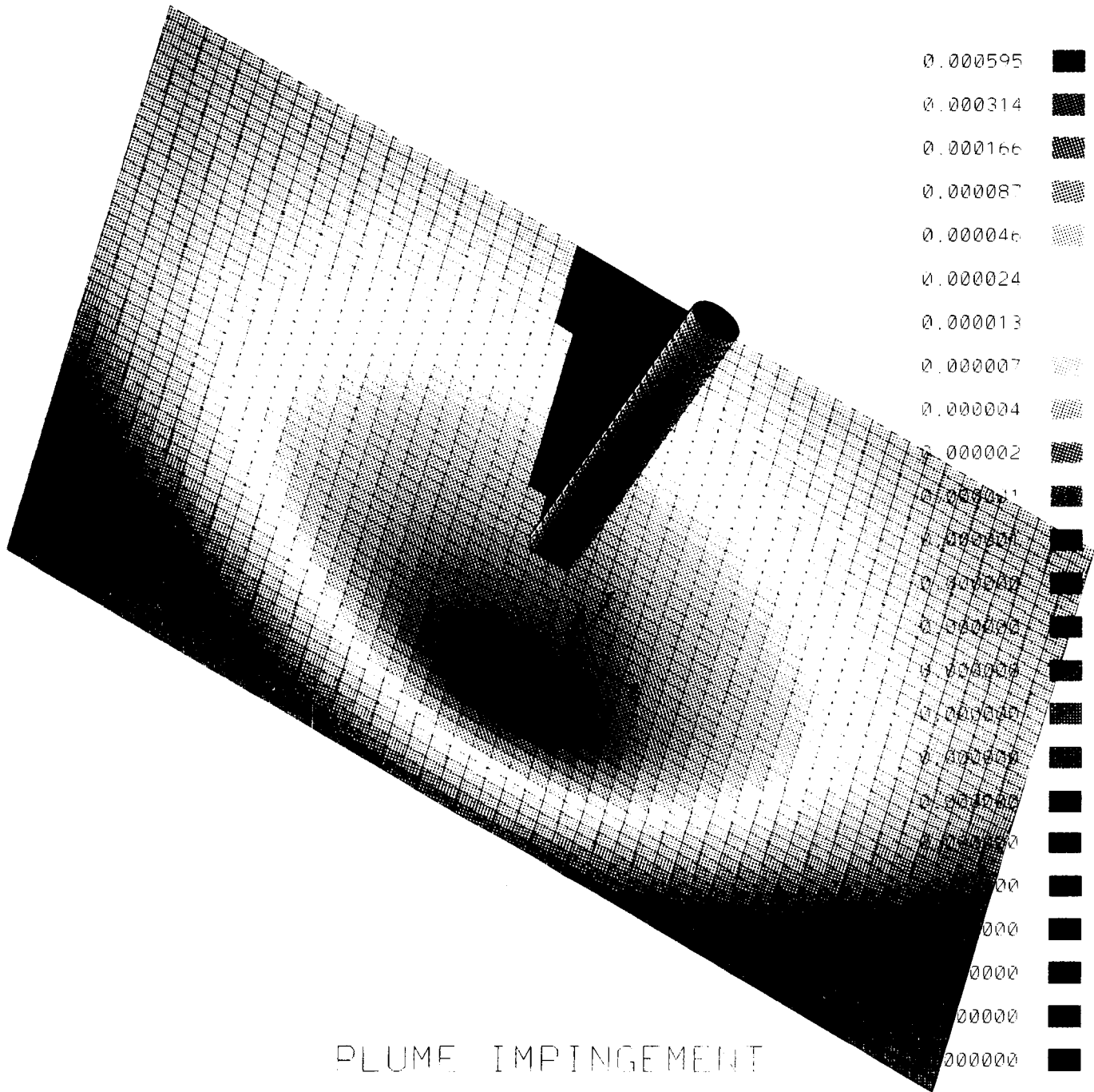


Figure 62: Sample Case 2 — Impingement Pressure (View 2)

References

- [1] Smith, S. D. and Ratliff, A. W., "Rocket Exhaust Plume Computer Program Improvement," Lockheed Missiles and Space Co. Report, LMSC-HREC D16220, June 1971.
- [2] Svehla, R. P. and McBride, B. J., "FORTRAN IV Computer Program for Calculation of Thermodynamics and Transport Properties of Complex Chemical Systems," NASA TN D-7056, Jan. 1976.
- [3] Smith, S. D., "High Altitude Chemically Reacting Gas Particle Mixtures," Lockheed Missiles and Space Co. Report, LMSC-HREC TR D867400, Oct. 1984.
- [4] Alred, J. W., "Flowfield Description of the Reaction Control System Jets of the Space Shuttle Orbiter," AIAA 18th Thermophysics Conference, Montreal, Canada, June 1983.
- [5] Smith, S. D., "Space Shuttle Solid Rocket Motor (SRM) Exhaust Plume Definitions — Sea Level to SRB Separation," Lockheed Missiles and Space Co. Report, LMSC-HREC TM D496879, Aug. 1976.
- [6] Smith, S. D., "Space Shuttle Solid Rocket Motor Sea Level Exhaust Plume Definition," Lockheed Missiles and Space Co. Report, LMSC-HREC TM D784045, Jan. 1981.
- [7] Boynton, F. P. and Rajadekhar, P. S., "Plume Interference with Space Shuttle Range Safety Signals," JANNAF 11th Plume Technology Mgt., CPIA Publication 306, May 1979.
- [8] Smith, S. D., "Definition of the Space Shuttle $A/A^*=5.83$, 2% Aluminum Separation Motor Plume Flowfield," Lockheed Missiles and Space Co. Report, LMSC-HREC TN D496599, Nov. 1975.
- [9] Tevepaugh, J. S., Smith, S. D., and Penny, M. M., "Assessment of Analytical Techniques for Predicting Solid Propellant Exhaust Plumes," AIAA Paper 77-711, 10th Fluid and Plasmadynamics Conference, June 1977.
- [10] Smith, S. D., "Definition of Solid Particle Plume Flowfields of the Space Shuttle Interim Upper Stage (IUS, SSUS-A, SSUS-D) Solid Booster Motors," Lockheed Missiles and Space Co. Report, LMSC-HREC TN D568087, Nov. 1977.
- [11] Ring, L. R., "Evaluation of Combustion/Nozzle Gasdynamic Models for Liquid Rocket Engine Applications," Air Force Rocket Propulsion Laboratory Report AFRPL-LR-77-46, July 1977.
- [12] Curtis, J. L., Moselle, J. R., and Marrone, P. V., "Plume Interference Prediction (PID) Code: User's Manual and Test and Evaluation Manual," Calspan Corporation Report KC5900 A-6, Vol. 1, April 1977.
- [13] Dash, S. M., Pergament, H. S., Wolf, D. E., Sinha, N., and Taylor, M. W., "The JANNAF Standardized Plume Flowfield Code Version II (SPF-II)," U. S. Army Missile Command Report CR-RD-SS-90-4, July 1990.
- [14] Dash, S. M., Weilerstein, G., and Vaglio-Laurin, R., "Compressibility Effects in Free Turbulent Shear Flows," Air Force Office of Scientific Research Report, TR-75-1436, Aug. 1975.

- [15] Launder, B. E., Morse, A., Rodi, W., and Spalding, D. B., "Prediction of Free Shear Layer Flows: A Comparison of Six Turbulence Models," in NASA SP-321 *Free Turbulent Shear Flows*, Vol. I, July 1972.
- [16] Spalding, D. B., "Concentration Fluctuation in a Round Turbulent Free Jet," *Chemical Engineering Science*, Vol. 26, 1971.
- [17] Jensen, D. E. and Wilson, A. S., "Prediction of Rocket Exhaust Flame Properties," *Combustion and Flame*, Vol. 25, 1975.
- [18] Pergament, H. S., Dash, S. M., and Varma, A. K., "Evaluation of Turbulence Models for Rocket and Aircraft Plume Flowfield Predictions," AIAA Paper 79-0359, Jan. 1979.
- [19] Smith, Sheldon D., Freeman, Jon A., and Farmer, Richard C., "Model Development for Exhaust Plume Effects on Launch Stand Design," SECA, Inc. Report SECA-89-20, September 1989.
- [20] Smith, Sheldon D., "Low Altitude Plume Impingement Handbook," SECA Report SECA-TR-91-8, August 9, 1991.
- [21] Wojciechowski, C. J. and Penny, M. M., "Development of High Altitude Plume Impingement Analysis for Calculating Heating Rates, Forces and Moments," Lockheed Missiles and Space Co. Report, LMSC-HREC D162867, March 1971.
- [22] Audeh, B. J. and Murph, J. E., "Input Guide for the Plume Impingement Computer Program (PLIMP)," Lockheed Missiles and Space Co. Report, LMSC-HEC TRF225888, June 30, 1988.
- [23] Smith, S. D., Burke, R. W., Xiques, K. E., and Freeman, J. A., "Space Station Plume Impingement and Contamination Control Study," Lockheed Missiles and Space Co. Report, LMSC-HEC TRF225887, Dec. 30, 1988.
- [24] Hoenig, R. J., "LMSC/HREC Boundary Layer Computer Program User's Manual," Lockheed Missiles and Space Co. Report A782404, TM 54/20-75, Aug. 1966.
- [25] Buck, M. L. and McLaughlin, E. J., "A Technique for Predicting Pressure Distributions and Aerodynamic Force Coefficients for Hypersonic Wing Reentry Vehicles (U)," Wright-Patterson AFB, Ohio, Report ASP-TDR-63-552, Aug. 1963 (Confidential).
- [26] James, M. L., Smith, G. M., and Wolford, J. C., *Applied Numerical Methods for Digital Computers*, Harper and Row, New York, 1985.
- [27] Smith, S. D., "Plume Modeling in Support of Space Station Contamination Model Development," Plumetech Report PT-R004, May 1989.
- [28] Smith, S. D., "Development of a Nozzle/Plume and Plume Impingement Code," Continuum, Inc. Report CI-FR-0089, Nov. 1986.
- [29] Tape of RAMP2 Flowfields and TRAN72, BLIMPJ, and RAMP2F Source Codes, Executables, and VAX Command Files
- [30] Tape of Sourceflow Data Files

Appendix A Experimental Verification

Two test cases are examined in this Appendix to demonstrate the validity of PLIMP predictions. In both cases experimental data are compared to RAMP2 and PLIMP pressure and/or heating rate calculations.

A.1 AEDC Tests

A.1.1 Introduction

Tests were conducted at the Arnold Engineering Development Center Rocket Test Facility J2A Test Cell [1] to determine the thermal and pressure effects of rocket-exhaust impingement on surfaces at 300,000 ft. simulated altitude using 100-lb. thrust, storable-propellant, attitude control rockets with area ratios (A/A^*) varying from 10 to 40. Heat transfer and surface pressure data were obtained on a flat plate (placed at various angles and distances from the rockets) which experienced impingement of the exhaust plumes from the operating engines.

The instrumented impingement panel consisted of a stainless steel sheet, 0.008 in. thick, bonded to a flat section of aluminum honeycomb sandwich 72 in. \times 72 in. \times 1.0 in. The support structure provided two degrees of freedom (vertical and rotational) for the adjustment of plate standoff distance and cant angle relative to the rocket engine. The test installation is shown in Fig. A1.

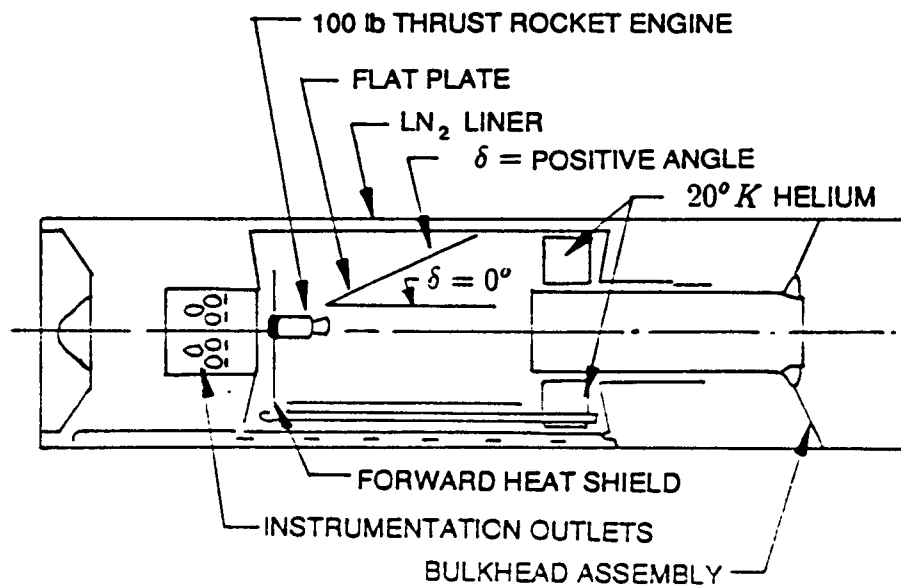


Figure A1: Test Installation

Several nozzle configurations were tested. Heating rates and surface pressures on the flat plate caused by exhaust impingement for the following three test cases are compared:

Case #1 Area ratio ($A/A^* = 10$) nozzle placed at a nozzle-axis-to-plate distance (h) of $3R_e$ ($R_e =$ exit radius) with a cant angle (δ) of 0°

Case #2 $A/A^* = 40$ nozzle placed at $h = 3R_e$ with $\delta = 0^\circ$

Case #3 $A/A^* = 40$ nozzle placed at $h = 3R_e$ with $\delta = 10^\circ$

The nozzle geometries and engine operating characteristics are presented in Table A1.

A.1.2 Analytical Simulation

Analytical calculations used to determine the impingement pressure and convective heating rate environments were divided into two areas. The first (plume analysis) involved calculating an undisturbed plume flowfield exhausting into a vacuum. Separate calculations were required for each nozzle. The second (impingement analysis) used surface geometry and appropriate shock theory to calculate the impingement pressures and heating rates. This methodology is based on the tandem utilization of the TRAN72, RAMP2, and PLIMP computer codes.

A.1.2.1 Plume Analysis

A modified version of TRAN72 was executed to generate a data tape describing the thermodynamic characteristics of the motor exhaust gases. The TRAN72 input file used in the $A/A^* = 10$ and the $A/A^* = 40$ rocket analysis is displayed in Table A2. The constant O/F option is used with 10 different total enthalpy tables input to simulate the heat transfer losses through the nozzle boundary layer. Experience in thermodynamic modeling of rocket exhaust flow has indicated that many chemical systems experience a transition from equilibrium to frozen chemistry during the expansion process. Previous calculations [2] give some rules of thumb in determining freeze pressures for certain types of motors and propellants. A freeze pressure corresponding to a pressure ratio (P_c/P_∞) of 5 is selected for each table.

An axisymmetric free plume exhausting into a vacuum was defined using RAMP2. RAMP2 was run using the option that first calculates the inviscid nozzle solution, then runs a boundary layer solution using BLIMPJ. This was followed by another RAMP2F nozzle solution (which modifies the nozzle contour with the boundary layer displacement thickness). Using the new edge conditions from the second nozzle calculation, BLIMPJ was executed again to determine the new boundary layer solution. For engines operating at vacuum conditions, the nozzle wall boundary layer can have a significant effect on the local exhaust plume properties. When the nozzle solution was completed, the analysis was continued into the plume flowfield. The flowfield chemistry used for the plume analysis was the same as that used for the nozzle. This was possible since

1. the flowfield chemistry was frozen inside the nozzle, and
2. the flow continually expands into the plume;

Table A1: Engine Operating Characteristics and Nozzle Geometry

Propellant	Engine Parameters
<p>Oxidizer N_2O_4</p> <p>Fuel 50% UDMH (Unsymmetrical dimethylhydrazine)</p> <p>50% N_2H_4</p>	<p>Area Ratio (A/A^*) = 10 (40)</p> <p>Exit radius = 1.37 (2.73) in.</p> <p>Chamber Pressure = 90 psia</p> <p>Throat radius = 0.434 in.</p> <p>Nozzle exit angle = 22 (8.3) degs.</p> <p>Ambient Pressure = 1.8×10^{-5} psi (at 300,000 ft.)</p> <p>Flow rate (nominal) = 0.11 lb/sec of fuel = 0.22 lb/sec of oxidizer</p>

NOZZLE COORDINATES			
X (in.)	R (in.)	A/A*	Exit Angle (degs)
0.000	0.434	10	22
0.278	0.513		
0.474	0.635		
0.812	0.832		
1.399	1.106		
1.866	1.349		
1.922	1.372		
2.393	1.565		
2.707	1.681		
2.920	1.762		
3.447	1.939	40	8.3
3.974	2.101		
4.501	2.245		
5.028	2.372		
5.555	2.483		
6.082	2.583		
6.609	2.671		
6.984	2.730		

Table A2: Bipropellant, Equilibrium/Frozen,
Constant O/F with Variable Total Enthalpy Tables

REACTANTS

C 2.0	H 8.0	N 2.0	50.0	11900.	L 298.15	F 0.783
N 2.0	H 4.0		50.0	12100.	L 298.15	F 1.0036
N 2.0	O 4.0		100.0	-4680.	L 298.15	O 1.431

NAMELISTS

SINPT2

RKT=T, PSIA=T,P=90.,9., MOCTF=T,OF=T,MIX=2.,
PARTHT=T,MOC2P=T,QDOTP=-1400.,-1200.,-1100.,-950.,-750.,-600.,
-450.,-300.,-150.,0.0,NQI=10

SEND

STAPGEN

IREAD=1, IO=8, IN=10

SEND

UDMH,N2H4,N2O4 pc=90. MKS

SRKTINP

PCP=2.,5.,10.,20.,40.,100.,500.,1000.,5000.,10000., NFZ=4

SEND

STOP

therefore, the chemistry should remain frozen. The RAMP2 input files for $AVA^* = 10$, and $AVA^* = 40$ engines are presented in Tables A3 and A4, respectively.

A.1.2.2 Impingement Analysis

The flowfield data generated by RAMP2 was first reformatted by PLIMP to create an ordered flowfield and then used by PLIMP to quickly determine the plume properties for an impingement analysis. Then the plume and the exposed composite structure (flat plate) susceptible to plume impingement were located with respect to a reference coordinate system. As shown in Fig. A2, the origins of the engine and reference coordinate systems were located at the nozzle exit plane. The flat plate coordinate system was located at its geometrical center.

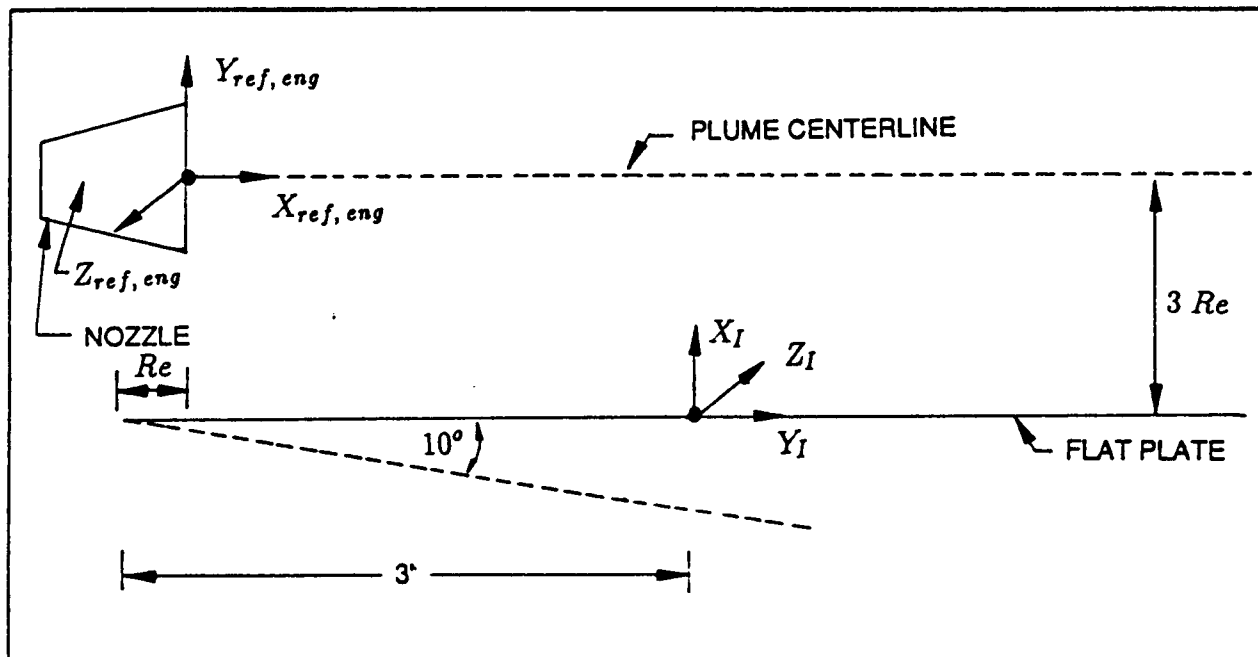


Figure A2: PLIMP Input Geometry for AEDC Test Comparison

Oblique shock theory was used to calculate the impingement pressure on the flat plate, while the convective heating rates were calculated employing the Eckert Reference Enthalpy method for flat plates. The PLIMP input files for cases #1, #2, and #3 are shown in Table A5.

Table A3: AEDC Test RAMP2 Input File (A/A* = 10)

```

0 3 2 1
exp test case #1 area ratio = 10

2 0 03020023 1 2202 011 2 3 0 0 1 00 0 012570
0.0361666 0.0
0 0.0000000 0.0361667 0.0000000 0 0.0008333 0.0361885 2.9967461
0 0.0016667 0.0362540 5.9934921 0 0.0025000 0.0363636 8.9902382
0 0.0033333 0.0365178 11.9869843 0 0.0041667 0.0367177 14.9837303
0 0.0050000 0.0369642 17.9804764 0 0.0058333 0.0372590 20.9772224
0 0.0066667 0.0376038 23.9739685 0 0.0075000 0.0380007 26.9707146
0 0.0083333 0.0384526 29.9674587 0 0.0125000 0.0409139 31.1743900
0 0.0166667 0.0434732 31.9446200 0 0.0208333 0.0460914 32.3422100
0 0.0250000 0.0487343 32.4311700 0 0.0411083 0.0587030 31.0720100
0 0.0572167 0.0681509 29.7128600 0 0.0800333 0.0806965 27.8951397
0 0.1028500 0.0923739 26.3107014 0 0.1256667 0.1033131 24.9194260
0 0.1484833 0.1136160 23.6834736 1 0.1501417 0.1143 23.5936440
3 0 0.1 1000.
2 0 1000.
UDMH,N2H4,N2O4 pc=90. MKS
0.0 0.0 1.01
100.0 0.0 0.0 0.0 10.0 90.0
0.01 0.01 1000.0 0.007 4.0 0.9
0 2 2 1 .015
0.0 2400. 1000. 2400.
    
```

Table A4: AEDC Test RAMP2 Input File (AVA* = 40)

```

0 3 2 1
exp test case #1 area ratio = 40

2 0 03020052 1 5102 011 2 3 0 0 1 00 0 012570
0.0361666 0.0
0 0.0000000 0.0361667 0.0000000 0 0.0003788 0.0361712 1.3621572
0 0.0007576 0.0361847 2.7243145 0 0.0011364 0.0362072 4.0864720
0 0.0015152 0.0362388 5.4486289 0 0.0018939 0.0362795 6.8107862
0 0.0022727 0.0363293 8.1729431 0 0.0026515 0.0363883 9.5351009
0 0.0030303 0.0364566 10.8972578 0 0.0034091 0.0365342 12.2594147
0 0.0037879 0.0366212 13.6215725 0 0.0041667 0.0367178 14.9837294
0 0.0045455 0.0368240 16.3458862 0 0.0049242 0.0369400 17.7080441
0 0.0053030 0.0370659 19.0702019 0 0.0056818 0.0372019 20.4323597
0 0.0060606 0.0373482 21.7945175 0 0.0064394 0.0375049 23.1566753
0 0.0068182 0.0376723 24.5188351 0 0.0071970 0.0378505 25.8809929
0 0.0075758 0.0380399 27.2431507 0 0.0079545 0.0382407 28.6053085
0 0.0083333 0.0384531 29.9674683 0 0.0125000 0.0409144 31.1743900
0 0.0166667 0.0434737 31.9446200 0 0.0208333 0.0460919 32.3422100
0 0.0250000 0.0487307 32.3511700 0 0.0411083 0.0586839 31.0720100
0 0.0572167 0.0681317 29.7128600 0 0.0800333 0.0806774 27.8951397
0 0.1028500 0.0923547 26.3107014 0 0.1256667 0.1032940 24.9194260
0 0.1484833 0.1135968 23.6834736 0 0.1713000 0.1233413 22.5690403
0 0.1941167 0.1325866 21.5463562 0 0.2169333 0.1413762 20.5896969
0 0.2397500 0.1497410 19.6773720 0 0.2625667 0.1577021 18.7917309
0 0.2853833 0.1652724 17.9191589 0 0.3082000 0.1724598 17.0500870
0 0.3310166 0.1792680 16.1789818 0 0.3538333 0.1856994 15.3043365
0 0.3766499 0.1917562 14.4287024 0 0.3994666 0.1974423 13.5586596
0 0.4222832 0.2027653 12.7048187 0 0.4450999 0.2077373 11.8818455
0 0.4679166 0.2123774 11.1084366 0 0.4907332 0.2167125 10.4073172
0 0.5135499 0.2207794 9.8052721 0 0.5363665 0.2246259 9.3330984
1 0.5542552 0.2275000 8.9218388
3 0 0.1 1000.
2. 0 1000.
UDMHL,N2H4,N2O4 pc=90. MKS
0.0 0.0 1.01
100.0 0.0 0.0 0.0 10.0 90.0
0.01 0.01 1000.0 0.007 4.0 0.9
0 2 2 1 .015
0.0 2400. 1000. 2400.
    
```

Table A5: AEDC Test PLIMP Input Files for Cases #1, #2, #3

<u>CASE #1</u>														
0	0	0	0	0	1	1	000	0	0	0	0	0		
EXPER TEST CASE #1 Area ratio 10 Cant 0														
1	0	3	1	10	1	00	0	2	0	0	1	1	1	0
0.0	0.0	0.0									1	1	2	3
0.0	0.0	0.0												
0.	0.	.1		-041.				1.		1.		1.		0.
2.592	-03	332.9		0.0		1.4		1716.		2.				
				2500.		1.		1.						2DFP
510.														
6.	6.													
20010603026.0		6.0												
2.8857	-0.3429	0.0				321								
0.0	-180.0	-90.0												
20.	-10.	0.0		0.0		20.		90.						
END														
<u>CASE #2</u>														
0	0	0	0	0	1	1	000	0	0	0	0	0		
EXPER TEST CASE #1 Area ratio 40 Cant 0														
1	0	3	1	10	1	00	0	2	0	0	1	1	1	0
0.0	0.0	0.0									1	1	2	3
0.0	0.0	0.0												
0.	0.	.1		-041.				1.		1.		1.		0.
2.592	-03	332.9		0.0		1.4		1716.		2.				
				2500.		1.		1.						2DFP
510.														
6.	6.													
20010603026.0		6.0												
2.7725	-0.6825	0.0				321								
0.0	-180.0	-90.0												
20.	-10.	0.0		0.0		20.		90.						
END														
<u>CASE #3</u>														
0	0	0	0	0	1	1	000	0	0	0	0	0		
EXPER TEST CASE #1 Area ratio 40 Cant 10														
1	0	3	1	10	0	00	0	2	0	0	1	1	1	0
0.0	0.0	0.0									1	1	2	3
0.0	0.0	0.0												
0.	0.	.1		-041.				1.		1.		1.		0.
2.592	-03	332.9		0.0		1.4		1716.		2.				
				2500.		1.		1.						2DFP
510.														
6.	6.													
20010603026.0		6.0												
2.7225	-1.1854	0.0				321								
0.0	-180.0	-100.0												
20.	-10.	0.0		0.0		20.		90.						
END														

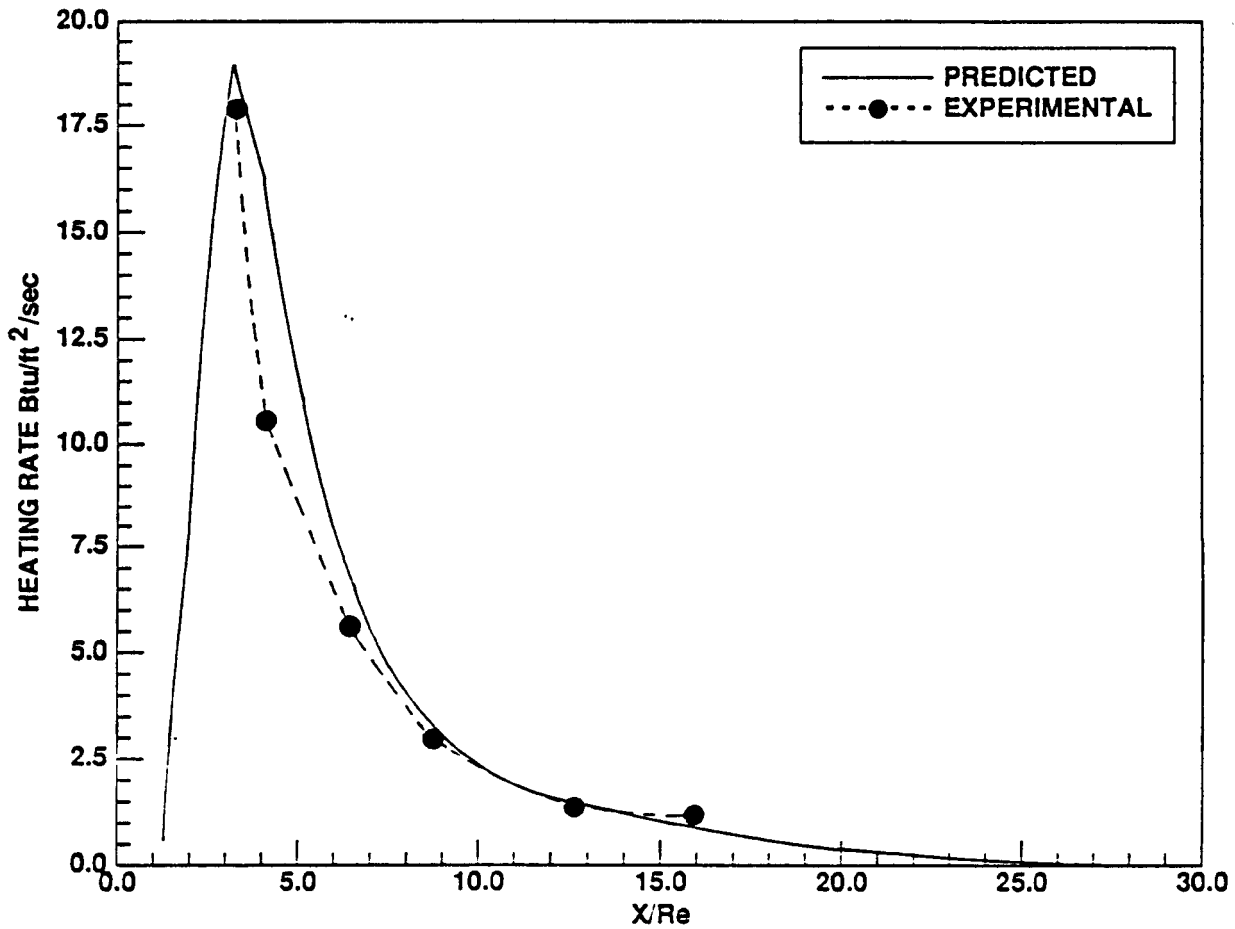
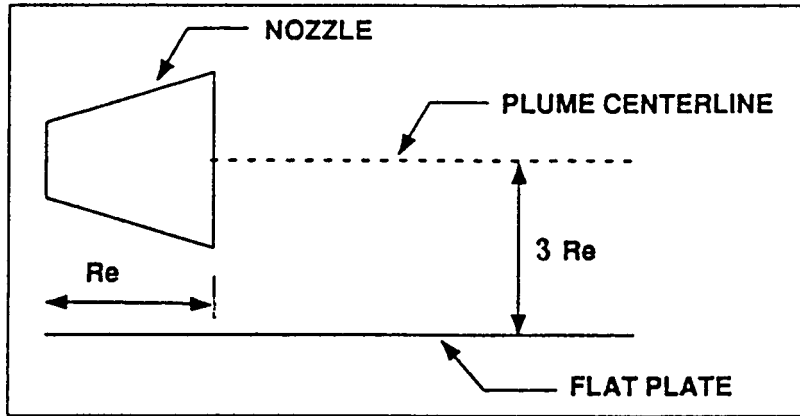


Figure A3: Analytical/Experimental Heating Rate Comparison for AEDC Case #1 along the Engine Centerline ($A/A^* = 10$, $h = 3R_e$, $\delta = 0$ Deg)

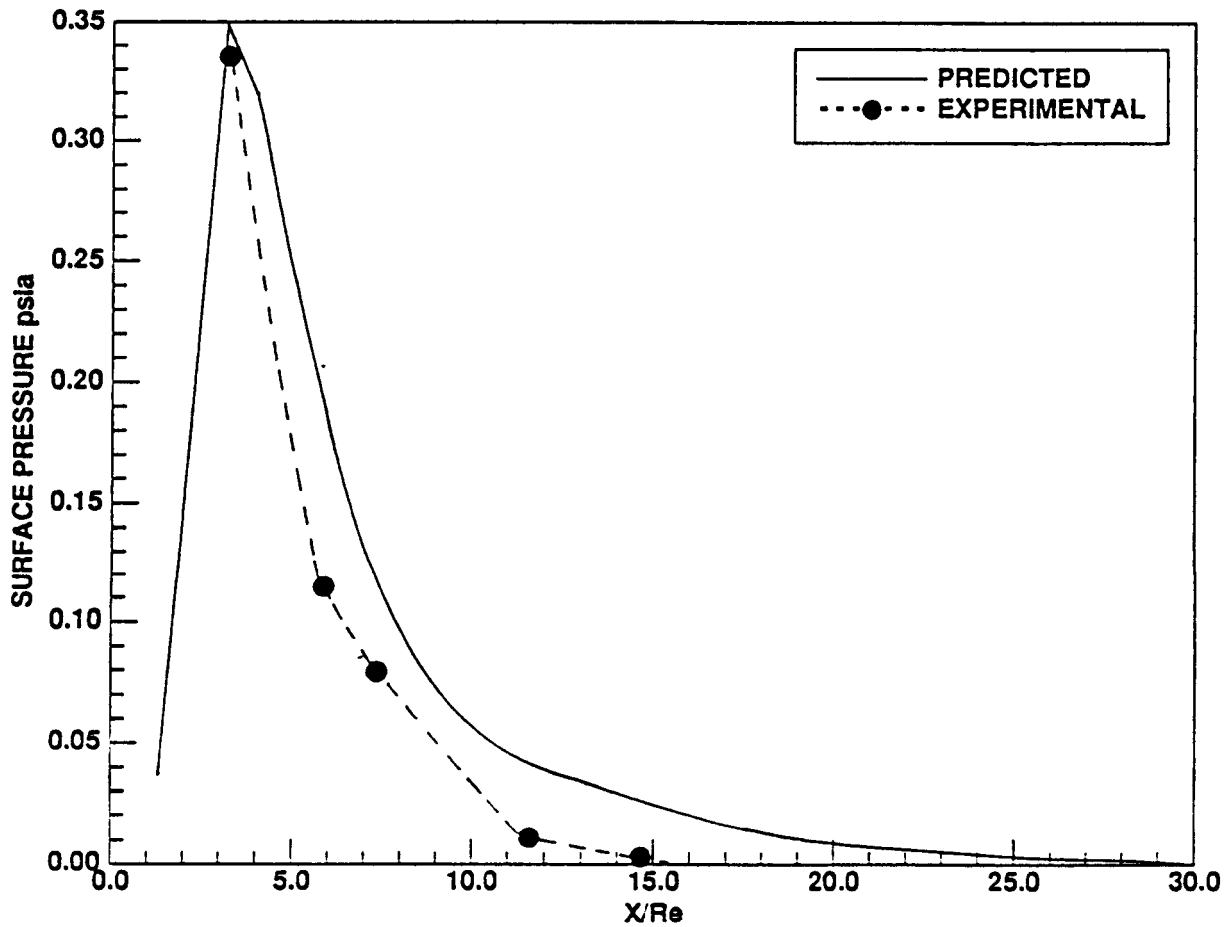
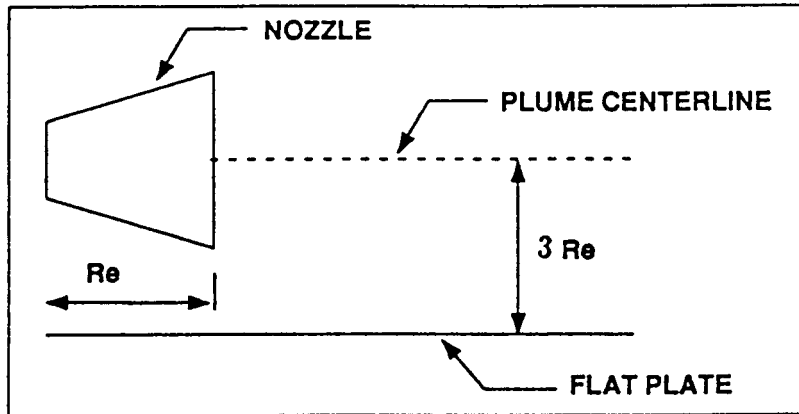


Figure A4: Analytical/Experimental Surface Pressure Comparison for AEDC Case #1 along the Engine Centerline ($A/A^* = 10$, $h = 3R_e$, $\delta = 0$ Deg)

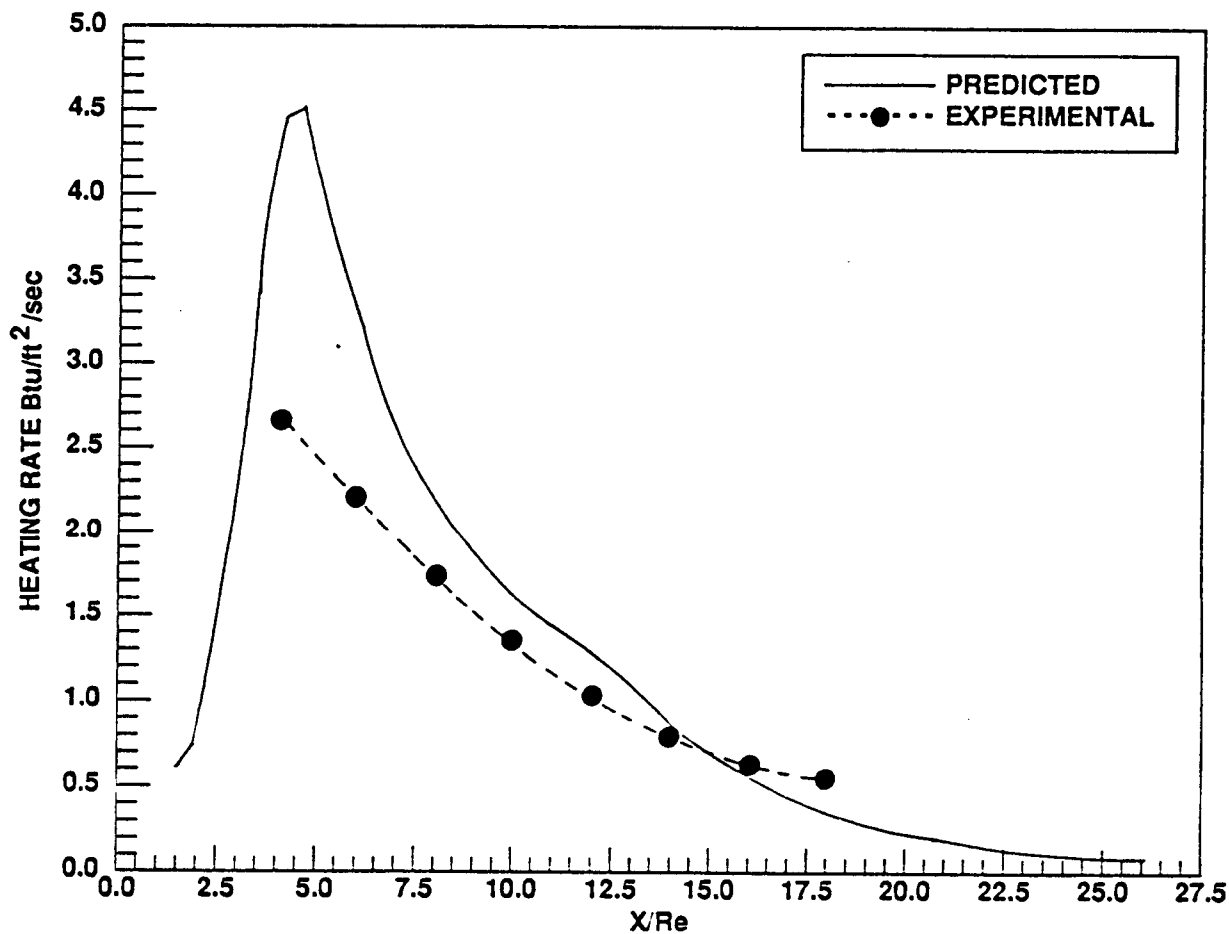
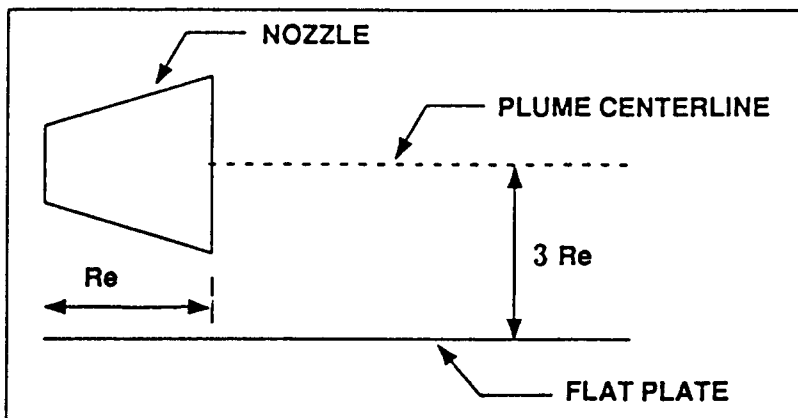


Figure A5: Analytical/Experimental Heating Rate Comparison for AEDC Case #2 along the Engine Centerline ($A/A^* = 40$, $h = 3R_e$, $\delta = 0$ Deg)

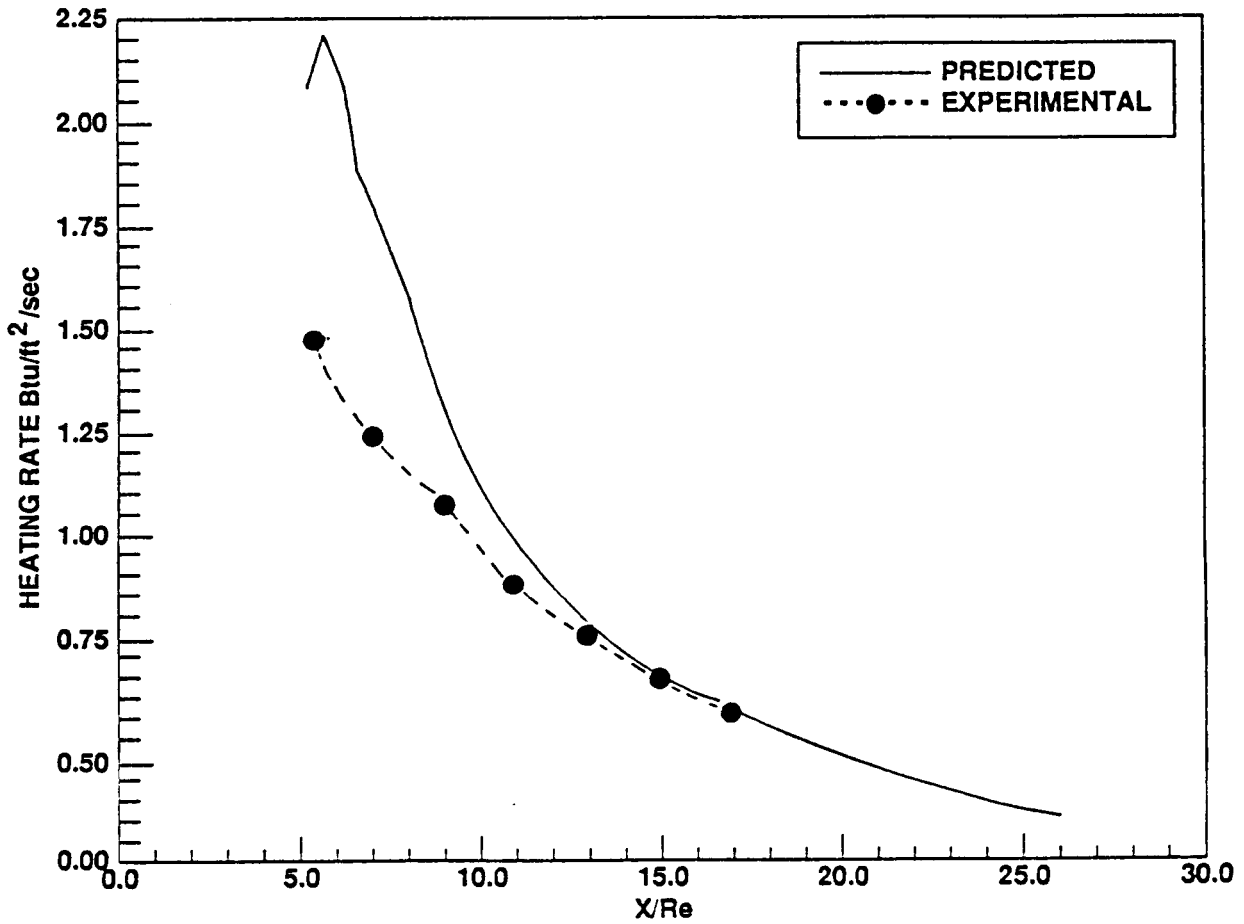
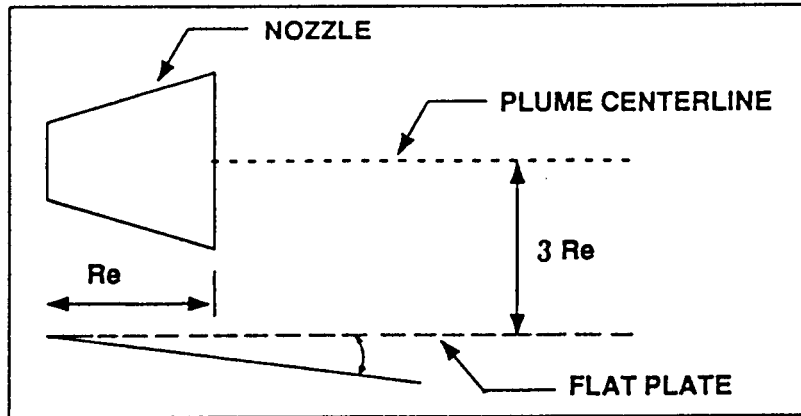


Figure A6: Analytical/Experimental Heating Rate Comparison for AEDC Case #3 along the Engine Centerline ($A/A^* = 40$, $h = 3R_e$, $\delta = 10$ Deg)

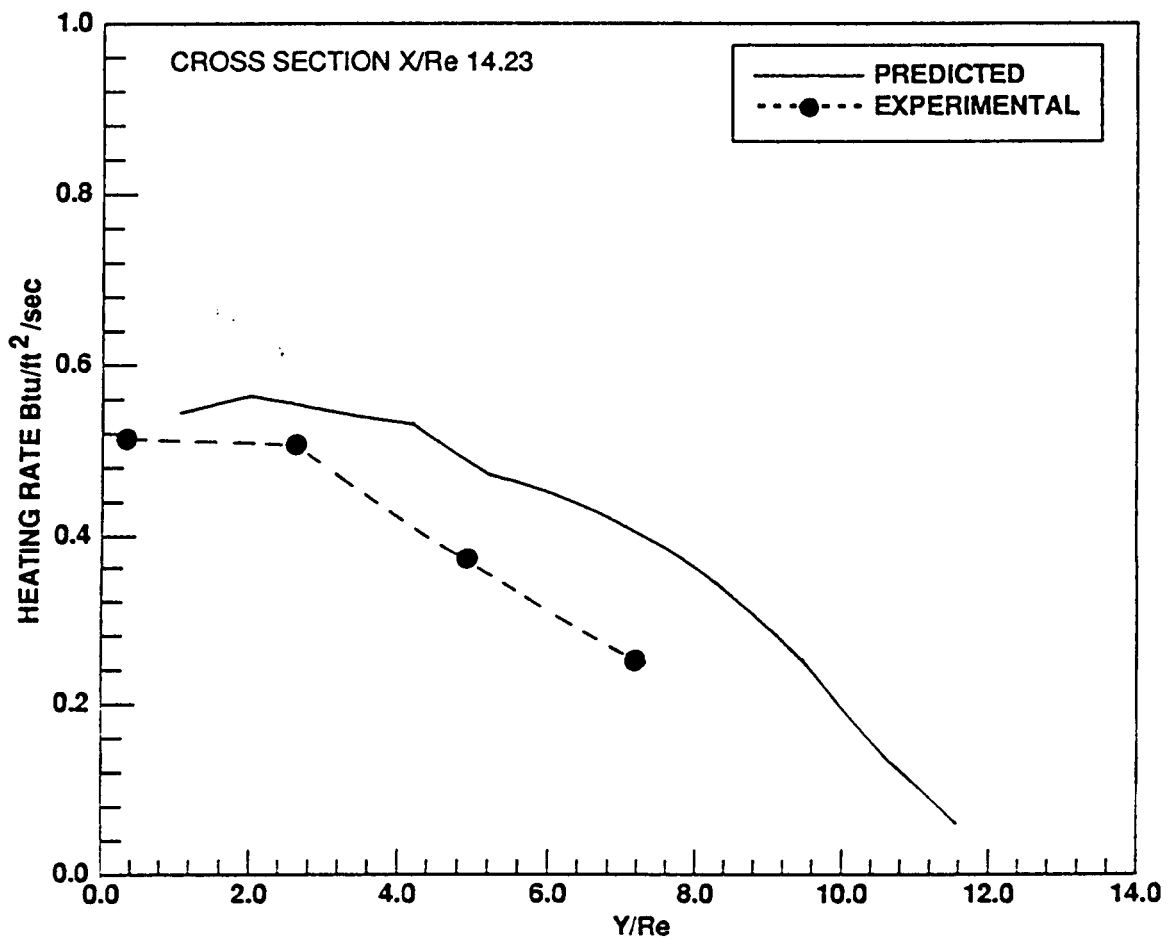
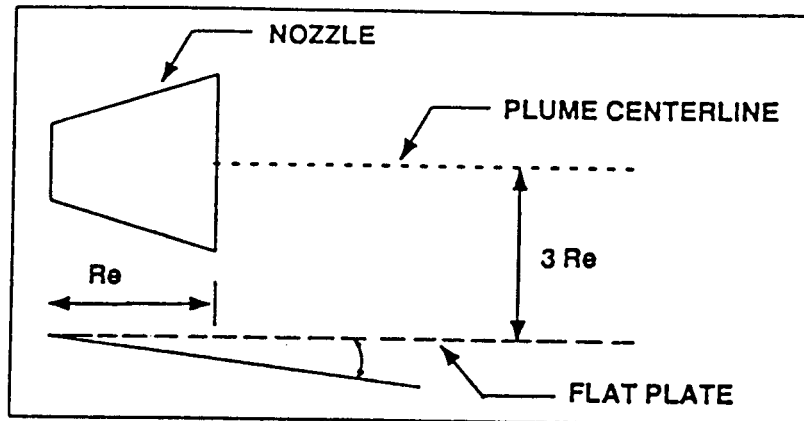


Figure A7: Analytical/Experimental Heating Rate Comparison with Distance from the Engine Centerline for AEDC Case #3 ($A/A^* = 40$, $h = 3R_e$, $\delta = 10$ Deg)

A.1.3 Results

PLIMP results are displayed in Figs. A3 through A7 for each of the three experimental test configurations. The centerline results for each case compare closely with their experimental values. The best agreement may be seen in Figs. A3 and A4 (surface pressure and heating rate comparisons, respectively, for case #1), while the heating rate comparisons for case #2 (Fig. A5) and case #3 (Fig. A6) differ by an average of approximately 50 percent. Figure A7 shows heating rate data for case #3 at $X/R_0 = 14.23$ with distance from the engine centerline. In all cases, PLIMP overpredicts the impact pressures and heating rates, while the location of the peak values show good agreement. The highest surface pressures were obtained for the $A/A^* = 10$ nozzle placed at $3R_0$ from the plate at $\delta = 0$ deg. Also, it can be noticed that the 10 deg cant reduces the peak heating rate for the $A/A^* = 40$ nozzle by approximately 50 percent. These observations are in agreement with the experimental results.

The overprediction of these results may be attributed to nonequilibrium chemistry effects, non-continuum effects, or may be due to small inaccuracies in individual computations [3].

A.2 Ariane Tests

A.2.1 Introduction

Experiments were conducted in the SR3 vacuum chamber of the Laboratoire d'Aérothermique at Meudon, France [4], to study plume impingement associated with the Ariane launcher's stage separation. During separation, retro-rockets are fired for approximately one second. The resultant exhaust gases impinge on the cylindrical wall of the second and third stages (Fig. A8). Heat-transfer measurements were obtained during the simulation on cylindrical antennas located perpendicular to the launcher wall.

The retro-rocket plume was generated using an underexpanded nozzle with an exit Mach number of 2.45. The propellant was nitrogen. Nozzle geometry, flow conditions, and stagnation conditions are presented in Table A6.

A 1/136 scale model of the launcher's upper stages was placed in the vicinity of the retro-rocket plume flowfield. Heat-transfer measurements were made at discrete points along four cylindrical antennas (4 mm diameter and 100 mm long) located perpendicular to the launcher wall. Antennas #1 and #2 were mounted 120 mm and 175 mm downstream of the nozzle exit as shown in Fig. A9. Figure A10 shows the positions of antennas #3 and #4 (one antenna is mounted in the plane of symmetry that contains the launcher and thruster axes, while the other antenna is inclined at an angle of 45 deg). The angle (α) between the launcher wall and thruster axis ranged from 11 deg to 30 deg.

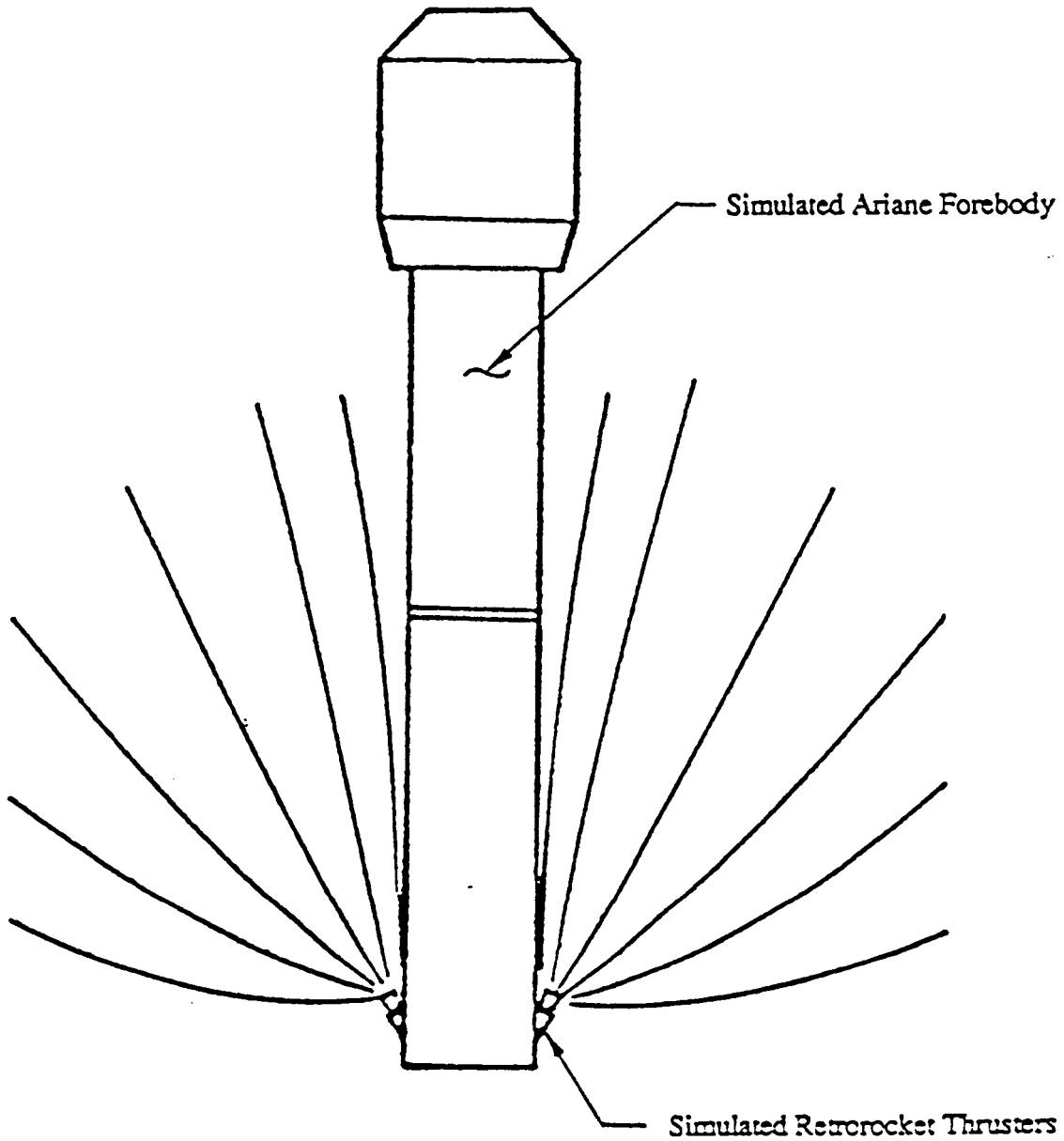


Figure A8: Ariane Configuration with Plume Due to Retro-rocket Firing

Table A6: Ariane Engine Operating Characteristics (Data Obtained from Ref. [A4])

SIMULATION CONDITIONS		
Stagnation conditions	Pressure, Pa Temperature, K	4×10^5 1100
Nozzle conditions	Propellant Throat radius, m Exit radius, m Half angle of divergence, deg	Nitrogen 0.8×10^3 1.3×10^3 10
Nozzle flow	Throat Reynolds number, based on diameter Mass flow rate, kg/s Thrust, N	2.04×10^4 0.96×10^3 1.18
Exit conditions	Relative boundary layer displacement thickness Mach number	2.39×10^{-2} 2.45

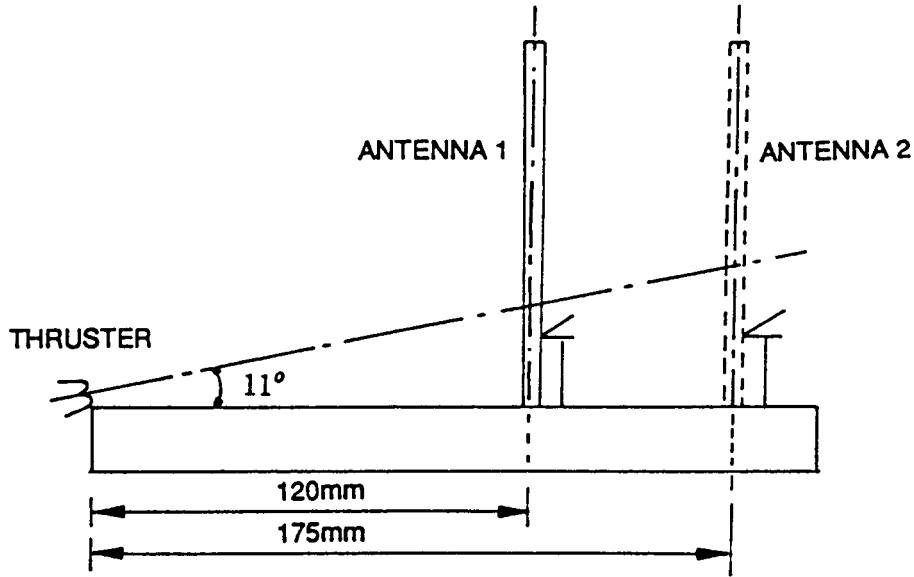


Figure A9: Position of Antennas #1 and #2 on the Cylindrical Model

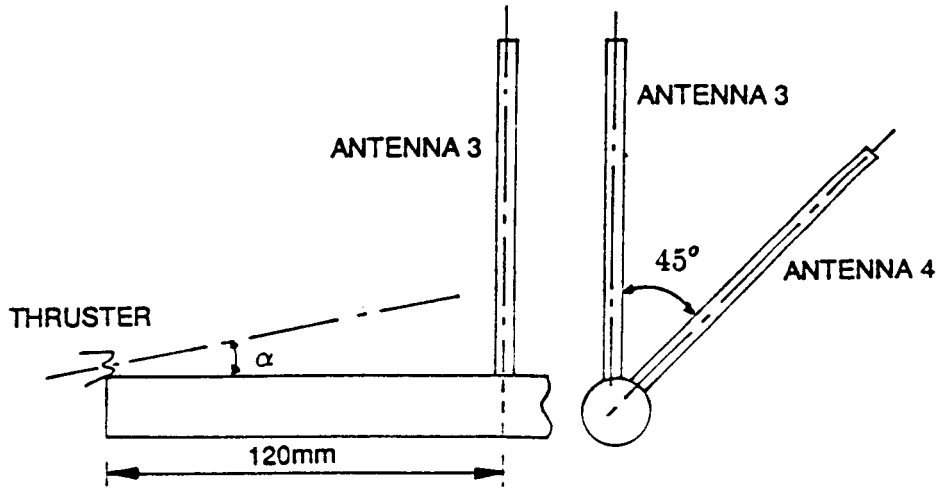


Figure A10: Position of Antennas #3 and #4 on the Cylindrical Model

A.2.2 Analytical Simulation

The calculations to determine the heating rates followed the same methodology mentioned in Section A.1.2.

A.2.2.1 Plume Analysis

An axisymmetric free plume was defined using the RAMP2 program combined with BLIMPJ to generate a nozzle boundary layer solution. RAMP2 was then restarted at the exit plane to generate the viscous plume. Since the propellant for the motor is an ideal gas (nitrogen), the gas thermodynamic data was input on a single card directly into the RAMP2 code. Therefore, it was not necessary to execute the TRAN72 Chemical Equilibrium Code. The RAMP2 input file is presented in Table A7.

A.2.2.2 Impingement Analysis

The impingement analysis was performed using PLIMP and the flowfield generated by RAMP2. Yawed Infinite Cylinder Theory was used to calculate the maximum heat flux values on the cylindrical antennas. Table A8 shows the input file required by PLIMP to perform the impingement analysis on antennas #3 and #4 ($\alpha = 11$ deg). Similar input files were required to determine heating rates on antennas #1 and #2.

A.2.3 Results

Maximum values of the heat fluxes resulting from plume impingement on the four antennas at different engine cants (α) are presented in Table A9. Figure A11 shows the analytical/experimental data comparison for antenna #1 ($\alpha = 11$ deg) with axial distance along the antenna. The large discrepancies at smaller axial values may be explained as follows; PLIMP does not take into account plume reflection from the launcher wall. This reflection causes high experimental heating rates at the lower regions of the antenna. The impingement results show better agreement at distances greater than 30 mm along antenna #1 (Fig. A11) where impingement is due to free plume interaction. A similar trend may be noticed in Figs. A12 and A13; analytical/experimental data comparisons for impingement on antenna #2 and antenna #4, respectively ($\alpha = 11$ deg). This may account for the approximately 49 percent overprediction in the maximum heat flux results shown in Table A9 for antenna #1. (Notice that this percentage difference decreases drastically as the engine cant (α) increases from 11 deg to 30 deg.) The percentage difference is shown in italics in Table A9 (the negative percentage for antenna #4 at $\alpha = 11$ deg represents an underprediction).

A.3 Conclusions

Several analytical/experimental data comparisons are presented which demonstrate the capabilities of the modified PLIMP computer program to assess the plume impingement environment on bodies subject to rocket plume impingement. Generally good agreement between the analytical results and experimental data was obtained. Where

Table A7: RAMP2 Input File for Ariane Tests

```

0 3 2 0
exp test case #2 heated nitrogen plume area ratio=2.6

31 0 03000003 100207 011 2 3 0 0 1 00 0 012570
2.6246 -030.0
1 0 -1.0 1.7221 -060.0 -1.0 -3.9369-032.2787 -04
2 1 0.0 0.0 0.0 0.17632 2.6043 -039.4182 -03
3 0 0.1 1000.
2 0 1000.
NITROGEN MKS 1 1
0.0
0.0 1
0.0 28.01 1.4 1100.0 3.94769 0.73 4.1772 -040.5
0.0 0.0 1.01
100.0 0.0 0.0 0.0 2.0 90.0
0.001 0.001 1000.0 0.005 6.0 0.8
1
N2
1.0
0 0 0 1 1
N2 1.0
4.1772 -040.73
    
```


Table A8: PLIMP Input File for Ariane Tests (Antennas #3 and #4 with $\alpha = 11$ Deg)

```

0 0 0 0 0 1 2 000 0 0 0 0 0
EXPER TEST CASE #2 Propellant N2 engine cant 11 degs
1 0 3 3 00 1 01 0 2 0 0 3 1 1 0 01
0.0 0.0 0.0 1 123
0.0 0.0 11.0
N2 1.
0. 0. .1 -081. 1. 1. 1. 0.
0.05574 350. 0.0 1.4 1716. 2.
2200. 0.0065615 1. 2DHM
450. 450. 450.
0.400262 0.062729 0.328084 0.013123 0.328084 0.013123
60030030050.031365 0.0 0.0 0.0 0.0 0.400262
010203
60011000056.5616 -030.0 0.0 0.0 0.0 0.328084
010203
60011000056.5616 -030.0 0.0 0.0 0.0 0.328084
010203
0.0 0.0 0.0 123
0.3937 0.031365 0.0 123
0.3937 0.02218 -0.02218 321
0.0 0.0 0.0
0.0 0.0 90.0
0.0 45.0 90.0
-90.0 90.0
-90.0 90.0
-90.0 90.0
100. 0.0 0.0 0.0 2.0 90.
END

```

large discrepancies between the experimental and predicted results exist, it is important to remember that PLIMP does not consider the effects of plume/surface reflection, only free plume interaction. This deficiency may account for the initial differences between the Ariane test results since the agreement appears to improve in areas where reflection is not a major consideration. Also, it should be noted that the PLIMP comparisons are highly dependent on the level of accuracy obtained in determining the undisturbed plume flowfield.

Table A9: Maximum Heating Rates for Ariane Tests on Antennas #1, #2, #3, and #4 at Various Engine Cants (α)

	\dot{q}_{max} (BTU/ft ² -sec)					
	$\alpha = 11$ deg		$\alpha = 20$ deg		$\alpha = 30$ deg	
	Exper.	Predicted	Exper.	Predicted	Exper.	Predicted
Antenna #1	5.2	49% 2.61	—	—	—	—
Antenna #2	3.0	41% 1.76	—	—	—	—
Antenna #3	5.2	49% 2.61	4.05	37% 2.54	3.08	22% 2.4
Antenna #4	3.8	32% 2.58	3.08	19% 2.49	2.03	-12% 2.28

Note: Percentage differences between the maximum experimental and predicted results are shown in *italics*.

A.4 References

- [A1] Piesik, E. T., Koppang, R. R., and Simkin, D. J., "Rocket-Exhaust Impingement on a Flat Plate at High Vacuum," *J. Spacecraft*, Vol. 3, No. 11, Nov. 1966.
- [A2] Smith, S. D., "High Altitude Supersonic Flow of Chemically Reacting Gas-Particle Mixtures — Vol. III: RAMP2 — Computer Code User's and Applications Manual," Lockheed Missiles and Space Co., Huntsville, AL, LMSC-HREC TR D867400-III, Oct. 1984.
- [A3] Penny, M. M., Smith, S. D., Ring, L. R., Roberts, B. B., and Greenwood, T. F., "Plume Impingement Technology," Lockheed Aircraft Corp., Lockheed Missiles and Space Co., Huntsville, AL, Technical Report CPIA Pub. 260, Vol. 1, Pt. 1, Oct. 1974.

- [A4] Allegre, J., Raffin, M., and Lengrand, J. C., "Experimental Study of the Plume Impingement Problem Associated with Rocket Stage Separation," AIAA Paper 85-0930, 1985.

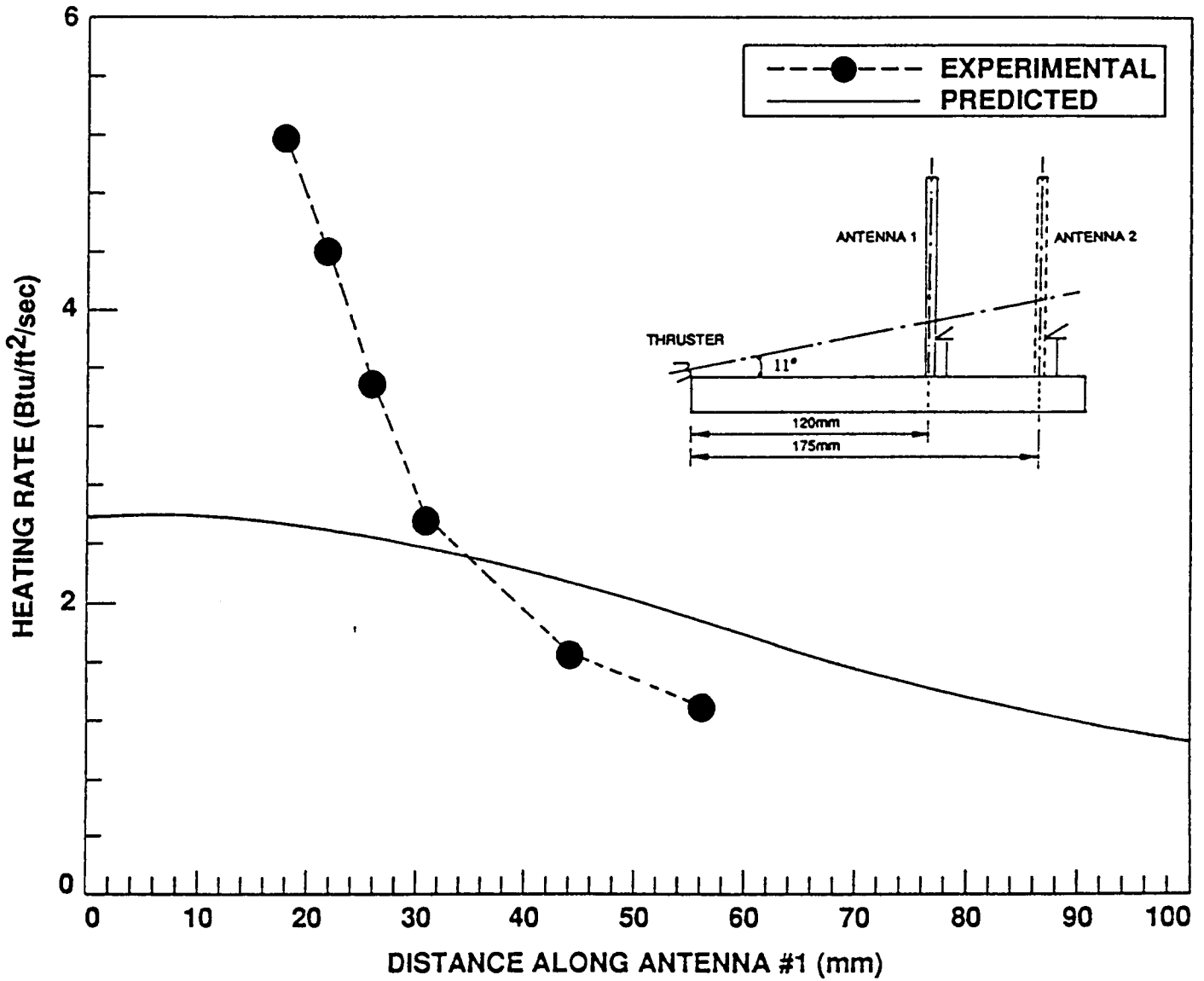


Figure A11: Analytical/Experimental Heating Rate Comparison on Antenna #1 with Axial Distance ($\alpha = 11$ Deg)

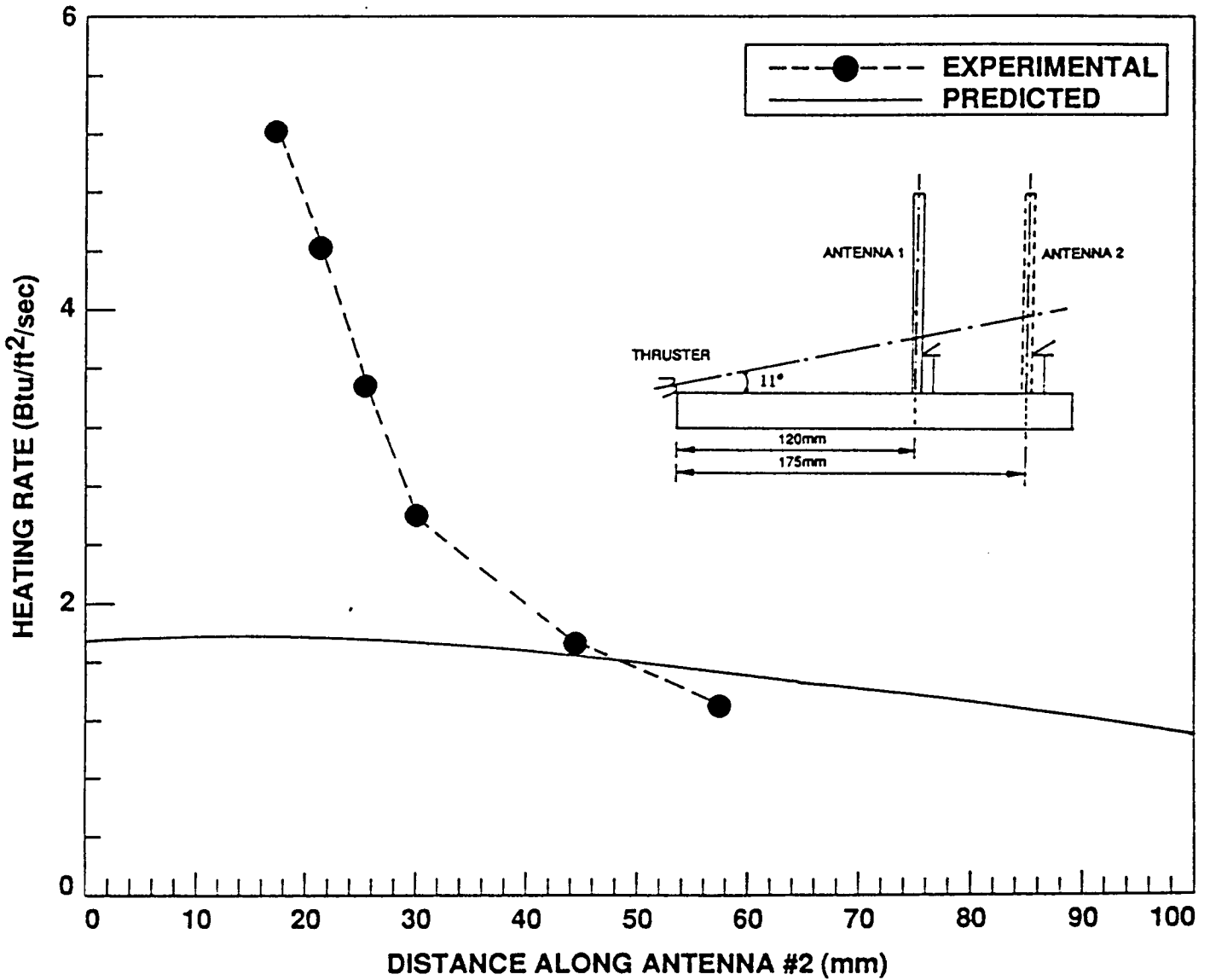


Figure A12: Analytical/Experimental Heating Rate Comparison on Antenna #2 with Axial Distance ($\alpha = 11$ Deg)

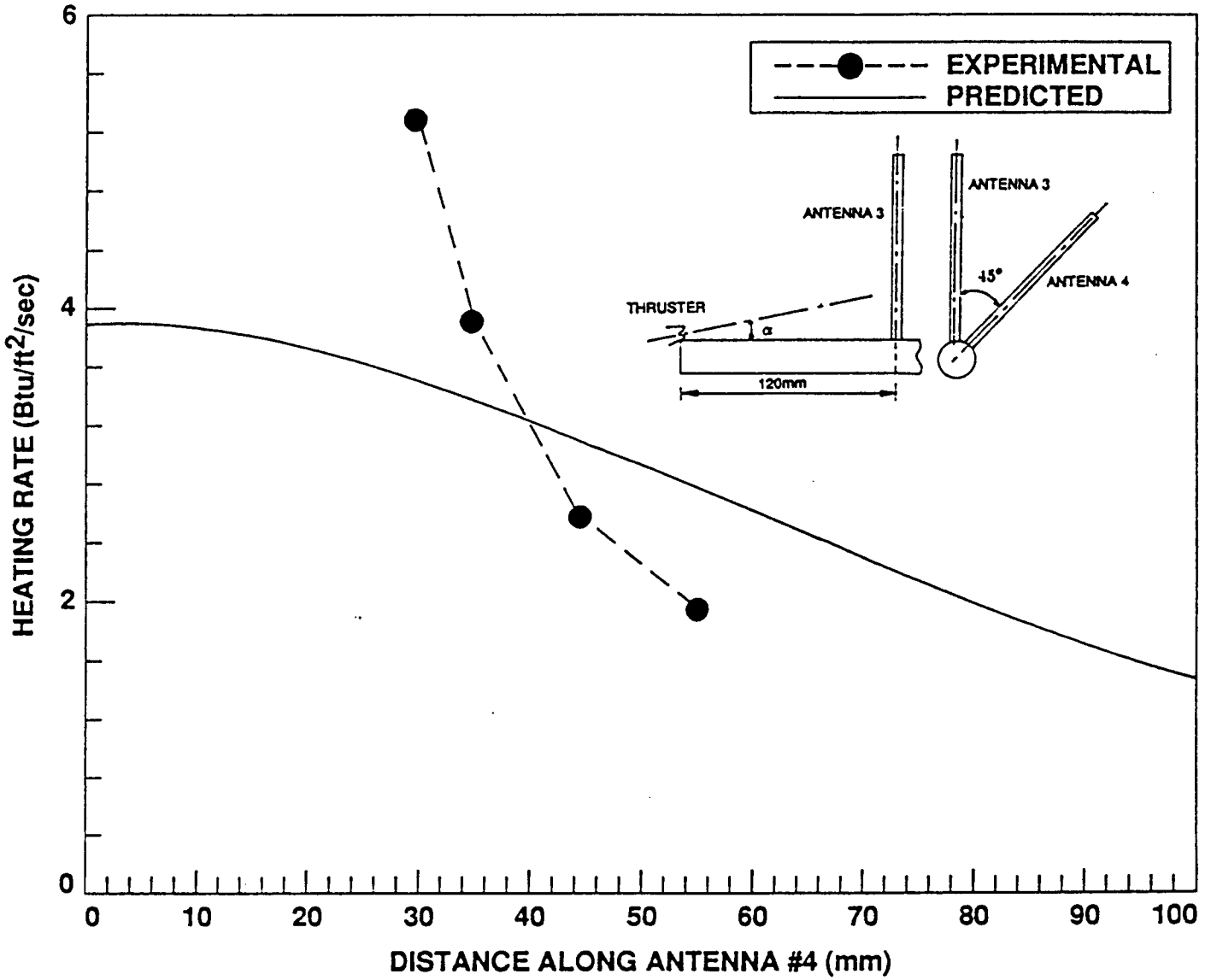


Figure A13: Analytical/Experimental Heating Rate Comparison on Antenna #4 with Axial Distance ($\alpha = 11$ Deg)

Appendix B

Description of Taped Program Code Input and Output Flowfield Files

A VAX/VMS version V5.3 backup tape was made of the following directories:

1. RAMP2 (Save set: RAMP.BCK)
2. BLIMPJ (Save set: BLIMPJ.BCK)
3. TRAN72 (Save set: CEC.BCK)
4. SFPGEN (Save set: SFPGEN.BCK)
5. BI-PROPELLANT ENGINES (Save set: BI_PROP.BCK)
6. H2/O2 ENGINES (Save set: H2_O2.BCK)
7. MONOPROPELLANT ENGINES (Save set: MONOPROP.BCK)
8. COLD GAS THRUSTERS (Save set: COLD_GAS.BCK)
9. SOLID PROPELLANT ENGINES (Save set: SOLID.BCK)

The contents of each save_set are:

1. RAMP.BCK

This directory contains the RAMP2 FORTRAN source code files, the VAX command files used to compile these source files and link their respective object files, (thus creating the executable file(s) required to generate the various plume flowfields) and the RAMP2 executable files.

Directory DUB1 : [PRENDERGAST.033013.RAMP.SOURCE]

ALGINT.FOR;1	ANUSNU.FOR;1	AOASTR.FOR;2	ARASSL.FOR;2
AVERAG.FOR;1	AXIS.FOR;1	BACWRD.FOR;1	BDRMP.FOR;2
BLEXIT.FOR;27	BLEXITMOD.FOR;12	BLEXITMOD1.FOR;2	BLIMPJ.DIR;1
BLIMPJLINK.COM;1	BLMPIN.FOR;15	BOUND.FOR;1	BOUND.A.FOR;2
CARCTR.FOR;1	CBREAK.FOR;6	CBREAK1.FOR;7	CEC.DIR;1
CHECK.FOR;5	CHEM.FOR;3	CODEE.FOR;1	CODEF.FOR;1
CODEH.FOR;1	COEFEQ.FOR;2	COEFF3.FOR;1	COEFS.FOR;1
D.D;1	D.DAT;2	DAMP.FOR;1	DECODE.FOR;1
DELTA.FOR;2	DLTA.FOR;4	DMDXSI.FOR;2	DOTPRD.FOR;1
DRAGCP.FOR;1	DRAGMR.FOR;1	DRIVER.FOR;14	DUMSYS.FOR;1
EMOFP.FOR;1	EMOFV.FOR;2	ENTROP.FOR;1	ENTSET.FOR;2
ERRORS.FOR;5	ESHOCK.FOR;1	EXPCOR.FOR;4	FABLE.FOR;9
FIXIL.FOR;1	FMCHK1.FOR;4	FMKNUD.FOR;11	FMTAPE.FOR;14
FNEWTN.FOR;1	FNUDSN1.FOR;5	FORWRD.FOR;1	FREEMC.FOR;5
FREPRO.FOR;3	GAPPBI.FOR;1	GAS.FOR;1	GASRD.FOR;19
GASTAP.FOR;11	HALL.FOR;1	HITER.FOR;6	HYPER.FOR;2
IBOUND.FOR;1	IDMPDT.FOR;1	IDMPFP.FOR;1	IDMPHI.FOR;1
IDMPOP.FOR;1	IDMPRO.FOR;1	IDMTAB.FOR;1	IDMTOB.FOR;1
IDMXSI.FOR;1	IDSPEC.FOR;1	IDTAPE.FOR;2	IMPUT.FOR;7

INITP.FOR;1	INRSCP.FOR;1	INRSCT.FOR;2	INTEGR.FOR;1
INTERP.FOR;1	INTT.FOR;1	IRAD.FOR;1	ITERM.FOR;1
ITERP.FOR;18	ITSUB.FOR;1	KIKOFF.FOR;2	LAGRNG.FOR;1
LIMITS.FOR;1	LIPIN.FOR;1	LOGIC.FOR;5	MASCON.FOR;1
MASS.FOR;2	MASSCK.FOR;10	MAXT.FOR;1	MCCRMK.FOR;1
MERGBL.FOR;4	MESH.FOR;17	MOCOSOL.FOR;2	NEWENT.FOR;1
NORMCK.FOR;1	NORSCK.FOR;5	OFSET.FOR;1	ONED.FOR;1
ORTHLS.FOR;1	OUT.FOR;9	OUTBIN.FOR;6	OUTPUT.FOR;1
OVEREX.FOR;2	PAGE.FOR;2	PAGVOF.FOR;1	PARINT.FOR;4
PARINT1.FOR;3	PARLOK.FOR;3	PARSTR.FOR;4	PARSTR1.FOR;1
PARTIL.FOR;6	PARTIN.FOR;10	PARTPH.FOR;2	PBLTRC.FOR;13
PDT.FOR;1	PFP.FOR;1	PHASE1.FOR;115	PHASE1_NODEL.FOR;1
PHI.FOR;1	PHYSOL.FOR;6	PHYZOL.FOR;1	PLMOUT.FOR;2
PLOAD.FOR;1	PLUMIN.FOR;56	POFEM.FOR;7	POFH.FOR;2
POINT.FOR;1	POP.FOR;1	PPATPT.FOR;2	PRANDT.FOR;2
PREAD.FOR;1	PRFRBD.FOR;1	PRO.FOR;1	PROP.FOR;1
PUNEX.FOR;24	RAMP.EXE;113	RAMP.FOR;2	RAMP2P.FOR;1
RAMP2PLINK.COM;100	RAMPBLNODEL.COM;2	RAMPBLNODEL.EXE;1	
RAMPBLWAL.COM;2	RAMPBLWAL.EXE;1	RAMPFOR.COM;2	
RAMPLINK.COM;27	RAMPWALNODEL.COM;2	RAMPWALNODEL.EXE;1	
RAMP_BLMOD.COM;2	RAMP_BLMOD.EXE;1	RAMP_NEW.EXE;2	
RAMP_NODEL.COM;1	RAMP_NODEL.EXE;1	RAMP_WALPR1.COM;2	
RAMP_WALPR1.EXE;1	RDIST1.FOR;9	READF.FOR;2	
REDIST.FOR;1	REPEAT.FOR;1	REST.FOR;7	RGMOFP.FOR;1
RGVOFM.FOR;4	RHOVEM.FOR;1	RITE.FOR;4	ROTERM.FOR;1
SEHTG.FOR;5	SITER.FOR;1	SLDP.FOR;1	SLINT.FOR;1
SLINTT.FOR;7	SLPLIN.FOR;1	SLSKIP.FOR;5	SOKFIX.FOR;1
SOKFLX.FOR;1	SOKINP.FOR;1	SOKSOL.FOR;1	SPACET1.FOR;12
SPACET2.FOR;1	SPCTX.FOR;1	SPECC.FOR;1	SPECIB.FOR;1
SPECIE.FOR;1	START.FOR;1	STARTV.FOR;1	STGMOD.FOR;2
STLINE.FOR;1	STLRFT.FOR;1	STRNOR.FOR;14	TAB.FOR;1
TAPMOV.FOR;1	TCHK.FOR;6	TEMTAB.FOR;3	TEST0.FOR;1
THERM1.FOR;2	THERMO1.FOR;45	THERMT.FOR;1	THETPM.FOR;1
THRUST.FOR;2	TKEY.FOR;1	TOB.FOR;1	TOFEM.FOR;1
TOFENH.FOR;3	TOFH.FOR;4	TOFV.FOR;9	TRACE.FOR;1
TRACEP.FOR;5	TRAN72.COM;98	TRANS.FOR;2	TURN.FOR;1
UOFEM.FOR;1	UOFV.FOR;1	VEMAG.FOR;1	VMOD1.FOR;2
VMOD1.OLB;1	VMOD2.FOR;1	VMODEL.FOR;1	VOFEM.FOR;1
WALMOD.FOR;14	WALMOD1.FOR;1	WALPRP.FOR;1	WALPRP1.FOR;2
WALPRP2.FOR;4	WALPRP4.FOR;2	WDGI.FOR;1	WEAK.FOR;1
WG.FOR;1	WOFA.FOR;1	WR.DAT;1	WRITP.FOR;3

WTFLOF.FOR;1 WTFLOP.FOR;4 WTFLOP1.FOR;3 WTT.FOR;1
 WXANDR.FOR;1 XSI.FOR;1 ZH.FOR;6
 Total of 241 files.

2. BLIMPJ.BCK

This directory contains the BLIMPJ FORTRAN source code files, the VAX command files, and the BLIMPJ executable file.

Directory DUB1: [PRENDERGAST.033013.RAMP.SOURCE.BLIMPJ]

ABMAX.FOR;2	BLIMPJ.EXE;10	BLIMPJ.FOR;4	BLIMPJLINK.COM;2
CHOMO.FOR;2	CRECT.FOR;2	DATE.FOR;2	DRIVER.FOR;3
EDGHSP.FOR;2	EDGPRP.FOR;2	EFC.FOR;3	EQUIL.FOR;2
ERP.FOR;2	ETIMEF.FOR;2	FILQ3.FOR;2	FILQ5.FOR;2
FINEQ.FOR;2	FIRSTG.FOR;2	FISLEQ.FOR;2	FUNXS.FOR;2
GEOM.FOR;2	HHOMO.FOR;2	HISTXI.FOR;2	ICOEFF.FOR;2
IDMTAD.FOR;2	IMONE.FOR;2	INPUT.FOR;5	IONLY.FOR;2
ITERAT.FOR;2	KINET.FOR;2	LIAD.FOR;2	LINCER.FOR;2
LINMAT.FOR;2	MATER.FOR;2	MATS1.FOR;2	MATS2.FOR;2
MISCIN.FOR;2	NNNCER.FOR;2	OGLE.FOR;2	OUTBL.FOR;2
POINTS.FOR;3	PROPS.FOR;2	READP.FOR;2	RECASE.FOR;5
REFCON.FOR;3	REFIT.FOR;2	RERAY.FOR;2	RNLKER.FOR;2
ROCOU.FOR;2	SECOND.FOR;2	SETUP.FOR;2	SHOMO.FOR;2
SLOPL.FOR;2	SLOPQ.FOR;1	STATE.FOR;2	STATEN.FOR;5
TAD.FOR;2	TAPMOV.FOR;2	TAYLOR.FOR;2	THERM.FOR;2
TLEFT.FOR;2	TOD.FOR;2	TRANCR.FOR;2	TRINT.FOR;2
TRMBL.FOR;2			

Total of 65 files.

3. CEC.BCK

This directory contains the TRAN72 FORTRAN source code files, the VAX command files, and the TRAN72 executable file.

Directory DUB1: [PRENDERGAST.033013.RAMP.SOURCE.CEC]

BDCEC.FOR;1	CECLINK.COM;2	CECR2F.EXE;1	CECR2F.FOR;1
CECTHERM.DAT;2	CPHS.FOR;1	DETON.FOR;1	DIFUSN.FOR;1
EFMT.FOR;1	EQLBRM.FOR;1	FROZEN.FOR;1	GAUSS.FOR;1
HCALC.FOR;1	INPUT.FOR;1	LGRNGE.FOR;1	MAIN1.FOR;1
MATRIX.FOR;1	MINV.FOR;1	MOCDAT.FOR;1	OUT.FOR;1
OUT1.FOR;1	REACT.FOR;2	RKTOUT.FOR;1	ROCKET.FOR;1
SAVE.FOR;1	SEARCH.FOR;1	SHCK.FOR;1	THERMP.FOR;1
TRANSP.FOR;1	VAREMT.FOR;1		

Total of 30 files.

4. SFPGEN.BCK

This directory contains the SFPGEN FORTRAN source code files, the VAX command files, and the SFPGEN executable file.

Directory DUB1: [PRENDERGAST.033013.RADLOOK.SOURCE]

AJ10SOURCE.COM;14	ALGINT.FOR;2	AMOLWT.FOR;3	ARASLS.FOR;3
ARASSL.FOR;3	ARRNGE.FOR;3	BDRAD.FOR;2	BDRYCK.FOR;3
BDRYEQ.FOR;4	CLDAT.INC;2	CURVFT.FOR;6	D296.DAT;1
D298.DAT;1	DARA.DAT;1	DEL.FOR;5	DELTA.FOR;2
DUM.DAT;1	EFIELD.FOR;2	EMOFV.FOR;2	ENTROP.FOR;3
ESHOCK.FOR;3	FABLE.FOR;6	FDBDRY.FOR;3	FETCH.FOR;3
GASNT.FOR;7	GASWT.FOR;5	GOTEM.FOR;3	HEAD.FOR;5
HEAD1.FOR;4	INIT.FOR;4	INITS.FOR;4	INITS1.FOR;5
INITS2.FOR;4	INITS3.FOR;4	INITS4.FOR;4	INITS5.FOR;7
INTD.FOR;5	INTERP.FOR;5	ITSUB.FOR;3	JPLGRD.FOR;3
JPLTAP.FOR;6	JPLTAP1.FOR;6	JUGGLE.EXE;11	JUGGLE.FOR;14
JUGGLE1.FOR;3	JWBTSS.FOR;8	LIMCK.FOR;2	MAIN.EXE;14
MAIN.FOR;8	MAXMIN.FOR;3	MOVEFL.FOR;5	
MRE15SOURCE.COM;8	MTRAN.FOR;3	OMVGN2SOURCE.COM;2	
PLUME.FOR;14	POFEM.FOR;2	POINTLINK.COM;10	
POINTS.FOR;2	PREV.FOR;2	RADLINK.COM;6	
RCS30SOURCE.COM;4	RCSVOFSOURCE.COM;2	READB.FOR;11	READF.FOR;3
REORDR.FOR;3	REWRITE.COM;74	RGVOFM.FOR;3	RHOVEM.FOR;5
SLD.DAT;2	SORTC.FOR;3	SORTCS.FOR;10	SORTCT.FOR;12
SOURCE.FOR;3	SOURCE1.FOR;3	SOURCE2.FOR;3	
SOURCE2LINK.COM;2	SOURCE3.FOR;4	SOURCE3LINK.COM;5	
SOURCE4.EXE;1	SOURCELINK.COM;2	SPECIE.FOR;5	SWAP.FOR;4
TABLE.FOR;6	TAPED.FOR;4	THERM1.FOR;2	TMP.DAT;1
TOFEM.FOR;2	TOFV.FOR;2	TRAMS.FOR;4	VECCHK.FOR;2
VOFEM.FOR;2	W.D;1	W.D1;1	W.D2;1
WEAK.FOR;3	WRITE1.DAT;1		

Total of 96 files.

5. BI_PROP.BCK

This directory contains the VAX command files (located in COMMAND.DIR), and all the input files (TRAN72, RAMP2) required to generate the RAMP2 bi-propellant plume flowfields. Each directory also contains the RAMP2 flowfield file and UNIT 6 output files for each engine.

Directory DUB1: [PRENDERGAST.BI_PROP]

AJ10.DIR;1	BP14.DIR;1	COMMAND.DIR;1	LMSC.DIR;1
R6C.DIR;1	RCSCONST.DIR;1	RCSVOF.DIR;1	READ_ME.DAT;4
VERN.DIR;1			

Total of 9 files.

Directory DUB1: [PRENDERGAST.BI_PROP.COMMAND]

AJ10SOURCE.COM;3	BP14SOURCE.COM;5	CECAJ10.COM;1	CECBP14.COM;2
CECLMSC.COM;2	CECR6C.COM;2	CECRCONST.COM;2	CECVERN.COM;2
COMMAND.DIR;1	LMSCSOURCE.COM;3	R6CSOURCE.COM;3	RAMPAJ10.COM;37
RAMPBP14.COM;31	RAMPLMSC.COM;5	RAMPR6C.COM;13	

RAMPRCSCONST.COM;2 RAMPRCSVOF.COM;6 RAMPVERN.COM;13
 RCSCONSTSOURCE.COM;2 RCSVOFSOURCE.COM;2 VERNSOURCE.COM;2
 Total of 21 files.

Directory DUB1: [PRENDERGAST.BI_PROP.AJ10]

AJ10.OUT;1 AJ10.OUT1;1 AJ10.OUT2;1 AJ10UN20.DAT;1
 AJ10UN3.DAT;2 AJ10UN5A.DAT;7 AJ10UN5B.DAT;3 AJ10UN5C.DAT;5
 CECAJ10.DAT;1 CECAJ10.UN10;1
 Total of 10 files.

Directory DUB1: [PRENDERGAST.BI_PROP.BP14]

BP14.OUT;2 BP14.OUT1;1 BP14.OUT2;1 BP14UN20.DAT;2
 BP14UN3.DAT;4 BP14UN5A.DAT;31 BP14UN5B.DAT;1 BP14UN5C.DAT;24
 CECBP14.DAT;2 CECBP14.UN10;1
 Total of 10 files.

Directory DUB1: [PRENDERGAST.BI_PROP.LMSC]

CECLMSC.DAT;2 CECLMSC.UN10;1 LMSC.OUT;2 LMSC.OUT1;1
 LMSC.OUT2;1 LMSCUN20.DAT;1 LMSCUN3.DAT;4 LMSCUN5A.DAT;15
 LMSCUN5B.DAT;1 LMSCUN5C.DAT;1
 Total of 10 files.

Directory DUB1: [PRENDERGAST.BI_PROP.R6C]

CECR6C.DAT;1 CECR6C.UN10;2 R6C.OUT;1 R6C.OUT1;1
 R6C.OUT2;1 R6CUN20.DAT;1 R6CUN3.DAT;2 R6CUN5A.DAT;4
 R6CUN5B.DAT;1 R6CUN5C.BAK;1 R6CUN5C.DAT;6
 Total of 11 files.

Directory DUB1: [PRENDERGAST.BI_PROP.RCSCONST]

CECRCSCONST.DAT;1 CECRCSCONST.UN10;1 RCSCONST.OUT;1
 RCSCONST.OUT1;1 RCSCONSTUN20.DAT;1 RCSCONSTUN3.DAT;1
 RCSCONSTUN5A.DAT;1 RCSCONSTUN5B.DAT;1 RCSCONSTUN5C.DAT;1
 Total of 9 files.

Directory DUB1: [PRENDERGAST.BI_PROP.RCSVOF]

CECRCSVOF.DAT;3 CECRCSVOF.UN10;1 RCSVOF.OUT;1
 RCSVOF.OUT1;6 RCSVOFUN20.DAT;1 RCSVOFUN3.DAT;7
 RCSVOFUN5.DAT;3 RCSVOFUN5A.DAT;5
 Total of 8 files.

Directory DUB1: [PRENDERGAST.BI_PROP.VERN]

CECVERN.DAT;4 CECVERN.UN10;2 VERN.OUT;1
 VERN.OUT1;1 VERN.OUT2;1 VERNUN20.DAT;1
 VERNUN3.DAT;3 VERNUN5A.DAT;5 VERNUN5A.DAT1;3
 VERNUN5B.DAT;1 VERNUN5C.DAT;2
 Total of 11 files.

6. H2_O2.BCK

This directory contains the VAX command files, and all the relevant files required to generate the RAMP2 liquid hydrogen/oxygen plume flowfields.

Directory DUB1: [PRENDERGAST.H2_O2]

ACS.DIR;1 COMMAND.DIR;1 NUC.DIR;1
 READ_ME.DAT;10 SSME.DIR;1
 Total of 5 files.

Directory DUB1: [PRENDERGAST.H2_O2.COMMAND]

CECACS.COM;2 CECNUC.COM;2 CECSSME.COM;2
 RAMPACS.COM;8 RAMPNUC.COM;8 RAMPSSME.COM;9
 Total of 6 files.

Directory DUB1: [PRENDERGAST.H2_O2.ACS]

ACSUN5A.DAT;3 ACSUN5B.DAT;1 ACSUN5C.DAT;5
 CECACS.DAT;1 CECAC.S.UN10;1
 Total of 5 files.

Directory DUB1: [PRENDERGAST.H2_O2.NUC]

CECNUC.DAT1;3 CECNUC.UN10;2 NUC.OUT;1
 NUC.OUT1;1 NUC.OUT2;2 NUCUN20.DAT;1
 NUCUN3.DAT;4 NUCUN5A.DAT;7 NUCUN5B.DAT;2
 NUCUN5C.DAT;4 NUCUN5C.DAT1;2
 Total of 11 files.

Directory DUB1: [PRENDERGAST.H2_O2.SSME]

CECSSME.DAT;3 CECSSME.UN10;2 SSME.OUT;1
 SSMEUN3.DAT;1 SSMEUN5A.DAT;14
 Total of 5 files.

7. MONOPROP.BCK

This directory contains the VAX command files, and all the relevant files required to generate the RAMP2 monopropellant plume flowfields.

Directory DUB1: [PRENDERGAST.MONOPROP]

COMMAND.DIR;1 FONG1.DIR;1 MOD2.DIR;1
 MONO3B.DIR;1 MONO5.DIR;1 MRE15.DIR;1
 RCS30.DIR;1 REA15.DIR;1 READ_ME.DAT;4
 Total of 9 files.

Directory DUB1: [PRENDERGAST.MONOPROP.COMMAND]

CECMOD2.COM;2 CECMONO3B.COM;2 CECMONO5.COM;2
 CECMRE15.COM;2 CECRCS30.COM;2 CECREA15.COM;2
 FONG1SOURCE.COM;3 MOD2SOURCE.COM;5 MONO3BSOURCE.COM;4
 MONO5SOURCE.COM;7 MRE15SOURCE.COM;13 RAMPFONG1.COM;3
 RAMPMOD2.COM;8 RAMPMONO3B.COM;4 RAMPMONO5.COM;12
 RAMPMRE15.COM;43 RAMPRCS30.COM;34 RAMPREA15.COM;7
 RCS30SOURCE.COM;4 REA15SOURCE.COM;4
 Total of 20 files.

Directory DUB1: [PRENDERGAST.MONOPROP.FONG1]

CECFONG1.DAT;3 CECFONG1.UN10;1 FONG1.OUT;1
 FONG1.OUT1;1 FONG1.OUT2;1 FONG1UN20.DAT;1

FONG1UN3.DAT;2 FONG1UN5A.DAT;5 FONG1UN5B.DAT;1
 FONG1UN5C.DAT;1
 Total of 10 files.

Directory DUB1: [PRENDERGAST.MONOPROP.MOD2]

CECMOD2.DAT;4 CECMOD2.UN10;5 MOD2.OUT;1
 MOD2.OUT1;1 MOD2.OUT2;1 MOD2UN20.DAT;14
 MOD2UN3.DAT;2 MOD2UN5A.DAT;19 MOD2UN5A.DAT1;1
 MOD2UN5B.DAT;2 MOD2UN5C.DAT;5
 Total of 11 files.

Directory DUB1: [PRENDERGAST.MONOPROP.MONO3B]

CECMONO3B.DAT;2 CECMONO3B.UN10;1 MONO3B.OUT;1
 MONO3B.OUT1;1 MONO3B.OUT2;1 MONO3BUN20.DAT;1
 MONO3BUN3.DAT;3 MONO3BUN5A.DAT;11 MONO3BUN5B.DAT;2
 MONO3BUN5C.DAT;2
 Total of 10 files.

Directory DUB1: [PRENDERGAST.MONOPROP.MONO5]

CECMONO5.DAT;2 CECMONO5.UN10;1 MONO5.OUT;4
 MONO5.OUT1;1 MONO5.OUT2;3 MONO5UN20.DAT;5
 MONO5UN3.DAT;5 MONO5UN5A.DAT;13 MONO5UN5A.DAT1;1
 MONO5UN5B.DAT;1 MONO5UN5C.DAT;2
 Total of 11 files.

Directory DUB1: [PRENDERGAST.MONOPROP.MRE15]

CECMRE15.DAT;3 CECMRE15.UN10;1 MRE15.OUT;1
 MRE15.OUT1;1 MRE15.OUT2;1 MRE15UN20.DAT;1
 MRE15UN3.DAT;2 MRE15UN5A.DAT;21 MRE15UN5B.DAT;1
 MRE15UN5C.DAT;4
 Total of 10 files.

Directory DUB1: [PRENDERGAST.MONOPROP.RCS30]

CECRCS30.DAT;4 CECRCS30.UN10;1 RCS30.OUT;1
 RCS30.OUT1;1 RCS30.OUT2;1 RCS30UN20.DAT;1
 RCS30UN3.DAT;3 RCS30UN5A.DAT;14 RCS30UN5A.DAT1;4
 RCS30UN5B.DAT;2 RCS30UN5C.DAT;7
 Total of 11 files.

Directory DUB1: [PRENDERGAST.MONOPROP.REA15]

CECREA15.DAT;2 CECREA15.UN10;2 REA15.OUT;1
 REA15.OUT1;1 REA15.OUT2;1 REA15UN20.DAT;16
 REA15UN3.DAT;2 REA15UN5A.DAT;12 REA15UN5A.DAT1;1
 REA15UN5B.DAT;3 REA15UN5C.DAT;3
 Total of 11 files.

8. COLD_GAS.BCK

This directory contains the VAX command files, and all the relevant files required to generate the RAMP2 cold gas thruster plume flowfields.

Directory DUB1: [PRENDERGAST.COLD_GAS]

AEDCSONIC.DIR;1	AFEGHE.DIR;1	COMMAND.DIR;1
EVASON4.DIR;1	EVAST1.DIR;1	EVAST4.DIR;1
HYPBAR.DIR;1	JPL1GN2.DIR;1	OMVGN2.DIR;1
READ_ME.DAT;4		

Total of 10 files.

Directory DUB1: [PRENDERGAST.COLD_GAS.COMMAND]

AEDCSONICSOURCE.COM;2	EVASON4SOURCE.COM;11	EVAST1SOURCE.COM;6
EVAST4SOURCE.COM;12	HYPBARSOURCE.COM;5	JPL1GN2SOURCE.COM;3
OMVGN2SOURCE.COM;9	RAMPAEDCSONIC.COM;1	RAMPAFEGHE.COM;1
RAMPEVASON4.COM;1	RAMPEVAST1.COM;1	RAMPEVAST4.COM;1
RAMPHYPBAR.COM;1	RAMPJPL1GN2.COM;1	RAMPOMVGN2.COM;1

Total of 15 files.

Directory DUB1: [PRENDERGAST.COLD_GAS.AEDCSONIC]

AEDCSONIC.OUT;1	AEDCSONICUN20.DAT;2	AEDCSONICUN3.DAT;1
AEDCSONICUN5A.DAT;4		

Total of 4 files.

Directory DUB1: [PRENDERGAST.COLD_GAS.AFEGHE]

AFEGHEUN5A.DAT;5	AFEGHEUN5B.DAT;1	AFEGHEUN5C.DAT;2
------------------	------------------	------------------

Total of 3 files.

Directory DUB1: [PRENDERGAST.COLD_GAS.EVASON4]

EVASON4.OUT;5	EVASON4UN20.DAT;6	EVASON4UN3.DAT;5
EVASON4UN5A.DAT;4		

Total of 4 files.

Directory DUB1: [PRENDERGAST.COLD_GAS.EVAST1]

EVAST1.OUT;2	EVAST1UN20.DAT;4	EVAST1UN3.DAT;2
EVAST1UN5A.DAT;6		

Total of 4 files.

Directory DUB1: [PRENDERGAST.COLD_GAS.EVAST4]

EVAST4.OUT;2	EVAST4UN20.DAT;4	EVAST4UN3.DAT;1
EVAST4UN5A.DAT;2		

Total of 4 files.

Directory DUB1: [PRENDERGAST.COLD_GAS.HYPBAR]

HYPBAR.OUT;1	HYPBARUN20.DAT;4	HYPBARUN3.DAT;1
HYPBARUN5A.DAT;2		

Total of 4 files.

Directory DUB1: [PRENDERGAST.COLD_GAS.JPL1GN2]

JPL1GN2.OUT;3	JPL1GN2.OUT1;2	JPL1GN2.OUT2;2
JPL1GN2UN20.DAT;1	JPL1GN2UN3.DAT;3	JPL1GN2UN5A.DAT;5
JPL1GN2UN5B.DAT;1	JPL1GN2UN5C.DAT;1	

Total of 8 files.

Directory DUB1: [PRENDERGAST.COLD_GAS.OMVGN2]

OMVGN2.OUT;5	OMVGN2.OUT1;2	OMVGN2UN20.DAT;4
OMVGN2UN3.DAT;1	OMVGN2UN5A.DAT;10	OMVGN2UN5B.DAT;3

Total of 6 files.

9. SOLID.BCK

This directory contains the VAX command files, and all the relevant files required to generate the RAMP2 solid propellant plume flowfields.

Directory DUB1: [PRENDERGAST.SOLID]

ASRM.DIR;1	COMMAND.DIR;1	HPM.DIR;1
READ_ME.DAT;8	STAR63.DIR;1	

Total of 5 files.

Directory DUB1: [PRENDERGAST.SOLID.COMMAND]

CECASRM.COM;2	CECHPM.COM;2	CECSTAR63.COM;2
RAMPASRM.COM;10	RAMPHPM.COM;25	RAMPSTAR63.COM;9
STAR63SOURCE.COM;5		

Total of 7 files.

Directory DUB1: [PRENDERGAST.SOLID.ASRM]

ASRMUN3.DAT;3	ASRMUN5.DAT;11	CECASRM.DAT;8
CECASRM.UN10;2	RAMPASRM.OUT;3	

Total of 5 files.

Directory DUB1: [PRENDERGAST.SOLID.HPM]

CECHPM.DAT;3	CECHPM.UN10;1	HPMUN3.DAT;2
HPMUN5.DAT;11	RAMPHPM.OUT;2	

Total of 5 files.

Directory DUB1: [PRENDERGAST.SOLID.STAR63]

CECSTAR63.DAT;2	CECSTAR63.UN10;2	STAR63.OUT;3
STAR63.OUT1;1	STAR63UN20.DAT;1	STAR63UN3.DAT;3
STAR63UN5A.DAT;5	STAR63UN5B.DAT;1	

Total of 8 files.

A VAX/VMS version V5.3 copy tape (ASCII tape) was made of the following directory: SOURCEFLOW (Save set: SOURCEFLOW.BCK).

This directory contains the SFPGEN sourceflow plume flowfields that can be used by PLIMP to perform relevant impingment analyses. The VAX command file, SOURCE.COM, contains an example command file used to generate an SFPGEN flowfields from an original RAMP2 flowfield.

The contents of this save_set are: SOURCEFLOW.BCK

Directory DUB1: [PRENDERGAST.SOURCEFLOW]

ACSUN16.DATSOR;2	AEDCSONICUN16.DATSOR;2	AFEGHEUN16.DATSOR;2
AJ10UN16.DATSOR;2	BP14UN16.DATSOR;2	EVASON4UN16.DATSOR;2
EVAST1UN16.DATSOR;3	EVAST4UN16.DATSOR;4	FONG1UN16.DATSOR;2
HYPBARUN16.DATSOR;2	JPL1GN2UN16.DATSOR;2	LMSCUN16.DATSOR;2
MOD2UN16.DATSOR;2	MONO3BUN16.DATSOR;2	MONO5UN16.DATSOR;2
MRE15UN16.DATSOR;2	NUCUN16.DATSOR;7	OMVGN2UN16.DATSOR;3
PLUMEDATA.BASE;11	R6CUN16.DATSOR;3	RCS30UN16.DATSOR;3
RCSCONSTUN16.DATSOR;1	RCSVOFUN16.DATSOR;3	REA15UN16.DATSOR;6
SOURCE.COM;2	STAR63UN16.DATSOR;2	VERNUN16.DATSOR;5

Total of 27 files.



Report Documentation Page

1. Report No.	2. Government Accession No.	3. Recipient's Catalog No.	
4. Title and Subtitle 1991 Version of the Plume Impingement Computer Program		5. Report Date October 1991	6. Performing Organization Code REMTECH inc.
		8. Performing Organization Report No. RTR 214-01	10. Work Unit No.
7. Author(s) Robert L. Bender, Richard E. Somers, Maurice J. Prendergast, Joseph P. Clayton (REMTECH) and Sheldon D. Smith (SECA)		11. Contract or Grant No. NAS8-38428	
9. Performing Organization Name and Address REMTECH inc. 3304 Westmill Drive Huntsville, AL 35805		13. Type of Report and Period Covered Final June 1989 - Oct. 1991	
12. Sponsoring Agency Name and Address National Aeronautics and Space Administration George C. Marshall Space Flight Center Marshall Space Flight Center, AL 35805		14. Sponsoring Agency Code	
15. Supplementary Notes Technical Monitor: EJ-71/Dr. T. F. Greenwood ED-33/Mr. Peter R. Sulyma			
16. Abstract The objective of this contract was to continue development of a vacuum plume impingement evaluator to provide an analyst with a capability for rapid assessment of thruster plume impingement scenarios. The research was divided into three areas: Plume Impingement Computer Program (PLIMP) modification/validation; graphics development; and documentation in the form of a Plume Handbook and PLIMP Input Guide. PLIMP code modifications and enhancements have been made to provide more detailed output information, improved shading, and the ability to order and analyze two-phase impingement solutions in a single execution. The code was also modified to accept plume flowfields generated using the Source Flow Plume Model Generator (SFPGEN). A pre/post processing graphics system utilizing the NCAR graphics package was developed. The pre-processing graphics system provides the capability to view the individual subshapes or the composite body (with or without shading) prior to PLIMP execution to ensure correct model geometry. The post processor enables the user to view 3D geometric object(s) with color contours representing surface conditions such as temperature, pressure, heating rate, etc. A Plume Handbook detailing the processes necessary to perform rapid assessment of plume impingement scenarios was the principal output of this research. The Handbook consists of two volumes. One volume describes the overall process of generating plume impingement environments with PLIMP from various plume flowfield sources. The second volume is an updated PLIMP specific input/output guide.			
17. Key Words (Suggested by Author(s)) Plume Impingement, Rocket Engine Graphics		18. Distribution Statement Unclassified — Unlimited	
19. Security Classif. (of this report) Unclassified	20. Security Classif. (of this page) Unclassified	21. No. of pages Vol. I — 137 Vol. II — 65	22. Price Unknown